Exciton dynamics studies from first-principles calculations: radiative recombination, exciton-phonon interactions, and ultrafast exciton relaxation

Thesis by
Hsiao-Yi Chen

In Partial Fulfillment of the Requirements for the
Degree of
Doctor of Philosophy

CALIFORNIA INSTITUTE OF TECHNOLOGY
Pasadena, California

2021
Defended May 24, 2021

Hsiao-Yi Chen
ORCID: 0000-0003-1962-5767

ACKNOWLEDGEMENTS

I don't think anyone could have their name on my to-thank list ranked before my advisor, Professor Marco Bernardi. Marco gave me everything I had been looking for during my first three years in Caltech, including an office with a huge window in the basement. As an advisor, he cares about my academic, research, and career progress and the balance between work and life for which sometimes I think I would be happier if he could put more pressure on me. He understands my ability, letting me do whatever I can do and supporting me to gain all I need to be an independent researcher. For example, if any reader finds this thesis well-written, I would refer the credit to Marco for his pushing me to sharpen my writing skill and for all the painful time he had been through when reading my drafts of all our papers.

Next, I am thankful for Nien-En who guided me to join Marco's group. During my days in the group, he gave me valuable insights to initialize my understanding of the core research of Marco's lab and new ideas about possible extension. He generously involved me in his projects, by asking me for help which I don't think he needed at all. Besides academia, Nien-En is truly a good PhD life partner. He is my daily PokemonGo training rival and the one who invited me to do my first half-marathon in my life. Without a doubt, Nien-En alone can define my work-life balance in the past 7 years.

I am also grateful for my collaborators in Europe, Maurizia and Davide. Their knowledge on exciton is the foundation to build up all the researches presented in this thesis. In our group, I first present my thanks to Vastal and Shiyuan for their works extending the potential of my study on radiative lifetime, and to Jin-Jian and Luis for technical help on using (pre-)Perturbo codes. I need to thank Benjamin for being made fun of by me without complaining but asking me for help when he needs. Last, I thank all members, I-Te, Austin, Megan, Xiao, Jinsoo, Raffaello, Ivan, and Dhruv, who stood along with me during these times.

Beyond research, I would like to present my sincere appreciation to my roommate, Yu-Li. He kept me company through all my worst times, taught me how to face this unfair society, and strengthened my ideology and faith about how the world should function. Without him, I might be the same childish man as I was 7 years ago. I want to thank Yu-An, my physics teammate since high school time. We struggled together during my first few years in Caltech. It was a painful, dark age of my PhD life, but I

am glad to have him as partner and rival on the way pursuing excellence in physics. I also need to thank Wen-Hui (Sophia). She is the one who helped me to start a normal life in the US. From setting up bank accounts to buying a car, she civilized me from middle-age barbarian life. I thank my half-marathon team members (I guess there was a team name called "CalTai1"), Kung-Yi, Shun-Jia, Yun-Ting, Tzu-Chieh, Yu-An, William, and Kuang-Ming, for all n×13-mile adventures we had run through together. I treasure all the times I enjoyed with my Taiwanese friends, Ying-Hsuan, Min-Feng, Chun-Lin, Albert (Chern), Hsieh-Chen, Chen-Chih, Lucas (Peng), Yu-Hong (Old Chao), Ho-Husan, Jeffrey (Uncle Hui), Yu-Hsien (Hwang Fu), Hui (Chiu), Kyle, Wei-Hsiang, Han-Hsin, Wei-Hsuan, Kuan-Chang, Sandy (Wong), Yu-Chen (and her pet Yen-Yung), Chien-I, Chien-Han, Steve, Cyuan-Han, and Howard (Lin).

Outside Caltech, I present my special thanks to Yi-Chun, Neng-Chieh, Ching-Yao, Chien-Yi, Po-Wen, and Yi-Jui. With them being here, I can re-visit those good-old days in high-school and in NTU which gave me courage to fight against bad-new days in LA. I also need to thank Po-Ta, Ke-Chih, and Chi-Shi, who guided me having fun in NYC during my most depressed time (wait, maybe not KC...he ditched us!) and Yen-Der for inviting me twice to be his groomsman. Our friendship across the US continent supported me and my dream from the beginning all the way to the end of this journey. For people in Taiwan, I need to thank Tsung-Hsuan and my undergraduate advisor, Heng-Yu. They are the initial condition of this whole story, and gave me critical suggestions whenever I met troubles and needed someone to consult. I also have to thank Hong-Yu (Lai) for her emotion support cheering me up during those days when my life lost its color.

Most of all, I need to express my greatest appreciation to all my family members, with those new joining and some who left forever from my life. I want to say thanks and sorry to my parents for their understanding of my absence during these days and especially the moments when they needed their son. I would like to thank my sisters and brother-in-laws for taking care of my parents and bringing my lovely niece and nephew to the world (distracting my parents' attention from me) and always keeping my place at home for my return anytime. Last, I want to address my miss of my grandfather who always had high expectation on me and was waiting for my return from abroad.

As a historical remark, at the time when this thesis was written, the world was fighting with the most serious pandemic after the 1918 Spanish flu. More than

three million lives had been taken by the COVID-19 which was identified in Wuhan, China, in December 2019 and broke out in early 2020. So, from September 2020 to February 2021, I spent my life working from home, literally from my lovely home in Taiwan which is the safest country in the world, thanks to all the effort done by the Taiwanese government and cooperation of our people. I never imagined that I could have my time with my family for such a long period after my departure from TPE airport on September 10th 2014, the same day I started my life in the US.

“Dance," said the Sheep Man. “Yougottadance. Aslongasthemusicplays. Yougotta dance. Don’teventhinkwhy. Starttothink, yourfeetstop. Youfeetstop, wegetstuck. Wegetstuck, you’restuck. Sodon’tpayanymind, nomatterhowdumb. Yougottakeepthestep. Yougottalimberup. Weknowyou’re tired, tiredandscared. Happenstoeveryone, okay? Justdon’tletyourfeetstop."

— Murakami, Haruki, *Dance Dance Dance*

ABSTRACT

Excitons are bound electron-hole pairs that dominate the optical response of semiconductors and insulators, especially in nanoscale and wide bandgap materials where the Coulomb interaction is weakly screened. Excitons can enhance light-matter coupling at certain wavelengths, thus making their host materials candidates for optoelectronic, photovoltaic, and quantum technology devices. For instance, two-dimensional transition metal dichalcogenides have a large and tunable optical response and hold promise for next-generation ultrathin light-emitting diodes. It is remarkable that exciton properties such as the binding energy and radiative lifetime can vary by orders of magnitude in different materials and can be further tuned by material properties like defects and lattice vibrations. Therefore, quantitative studies of exciton interactions and dynamics can advance understanding of the optical response of complex materials and play a role in the design of future devices. Among theoretical studies, numerical approaches based on density functional theory (DFT) can quantitatively address the electronic structure in real materials and their response to external perturbations, enabling accurate calculations of the conductivity and dielectric properties. These first-principle methods, which employ numerical quantum mechanics and use only the atomic structure of the material as input (making no use of empirical parameters) have revolutionized studies of materials and condensed matter physics. Over the last few years, first-principles methods for studies of excitons have focused on the GW-Bathe-Salpeter equation (GW-BSE) method to compute exciton energies and optical absorption spectra. However, going beyond calculations of exciton energetics to address the exciton dynamical processes remains challenging and is an exciting new frontier of first-principles studies.

This thesis develops theory and novel numerical approaches to study exciton radiative and nonradiative interactions from first-principles. For the radiative processes, we demonstrate a systematic derivation of exciton radiative lifetimes in materials ranging from bulk to nanostructures and molecules. The results correctly reproduce the observed power-law temperature dependence of the radiative lifetimes. To benchmark our calculations, we study exciton radiative lifetimes in gas-phase molecules, obtaining excellent agreement between theory and experiment. Our framework is then applied in three different studies. First, we extend the radiative lifetime formula to account for the dependence on light polarization and valley occupation and investigate exciton recombination in two-dimensional transition metal

dichalcogenides (2D-TMDs). We show that excitons emit light anisotropically upon recombination when they are in any quantum superposition state of the K and K′ inequivalent valleys. When averaged over the emission angle and exciton momentum, our new treatment recovers the temperature-dependent radiative lifetimes derived in early literature. Second, we use the exciton energy and radiative lifetimes to identify the atomic structure of the defects in monolayer hexagonal boron nitride (h-BN). In the study, we narrow down the potential structures to nine candidates and identify the highest-likelihood structure as the V_NN_B defect, consisting of a nitrogen vacancy plus a carbon replacing boron in h-BN. Finally, we generalize the discussion of isotropic bulk system to accurately compute the exciton radiative lifetimes in bulk uniaxial crystals, focusing on wurtzite GaN. Our computed radiative lifetimes are in very good agreement with experiments at low temperature. We show that taking into account excitonic effect and spin-orbit coupling (to include the exciton fine structure) is essential for computing accurate radiative lifetimes. A model for exciton dissociation into free carriers allows us to compute the radiative lifetimes up to room temperature.

In the study of exciton non-radiative process, we focus on the exciton-phonon (ex-ph) interaction, which plays an important role to understand the dynamics of excitons in materials. We establish and implement a first-principle formalism to compute the ex-ph coupling constants by combining the electron-phonon couplings and the exciton wavefunctions from the GW-BSE approach. Using the computed ex-ph coupling matrix elements, we calculate the ex-ph relaxation times as a function of exciton energy, momentum, temperature, and phonon mode in bulk h-BN. Our calculations reveal the dominant ex-ph coupling with the longitudinal optical (LO) mode and identify the threshold for LO phonon emission with an associated ~15 fs LO emission characteristic time. In addition, we derive the phonon-assisted photoluminescence (PL) from the ex-ph interaction and correctly reproduce the PL spectrum observed in h-BN at both 8 K and 100 K. Based on our successful study of ex-ph interactions in bulk h-BN, we extend the discussion to materials with strong spin-orbit coupling. We investigate the bright exciton linewidth broadening and PL in monolayer WSe_2. The numerical results show an increase of linewidth by 20 meV from 0 K to 250 K as observed in early experiments and identify the main PL peak as a consequence of LA phonon emission while the side band is due to optical phonons. Lastly, we present results from a joint theory-experiment study of the ultrafast exciton dynamics in WSe_2. We develop a Boltzmann equation for excitons and employ it to model ultrafast exciton relaxation due to ex-ph processes. The simulation and experiment

both show a ~70 fs time delay for the electron intervalley scattering from the K- to the Q-valley due to exciton dynamical effects. We also develop accurate simulations of time-domain angle-resolved photoemission (ARPES) experiments, which are becoming a powerful experimental probe of exciton dynamics in condensed matter. In summary, this thesis work paves the way to quantitative studies of exciton radiative and non-radiative processes, as well as exciton ultrafast dynamics, and quantitative modeling of pump-probe experiments in materials with strongly bound excitons.

PUBLISHED CONTENT AND CONTRIBUTIONS

[1] H.-Y. Chen, D. Sangalli, and M. Bernardi, "Real-time exciton dynamics and time-domain ARPES simulations using first-principles exciton-phonon interactions", In Preparation., (2021),
H.-Y. Chen contributed to the code implementation, numerical calculations, and manuscript writing.

[2] S. Dong, H.-Y. Chen, D. Sangalli, M. Bernardi, and R. Ernstorfer, "Resolving exciton dynamics in monolayer WSe_2 via time-resolved ARPES: pump and probe measurement and real-time ab initio simulation", In Preparation., (2021),
Joint theory-experiment paper. H.-Y. Chen contributed to the theory part, including code implementation, numerical calculations, and manuscript writing.

[3] H.-Y. Chen, D. Sangalli, and M. Bernardi, "Exciton-phonon interaction and relaxation times from first principles", Phys. Rev. Lett. **125**, 107401 (2020). DOI: 10.1103/PhysRevLett.125.107401.
H.-Y. Chen contributed to theory derivations, code implementation, numerical calculations, and manuscript writing.

[4] S. Gao, H.-Y. Chen, and M. Bernardi, "Radiative properties and excitons of candidate defect emitters in hexagonal boron nitride", NPJ Comput. Mater. 2020 (Accepted for publication) (2020),
H.-Y. Chen contributed to the theory derivation.

[5] N.-E. Lee, H.-Y. Chen, J.-J. Zhou, and M. Bernardi, "Facile ab initio approach for self-localized polarons from canonical transformations", arXiv preprint arXiv:2011.03620 (2020),
H.-Y. Chen contributed to the theory derivation.

[6] N.-E. Lee, J.-J. Zhou, H.-Y. Chen, and M. Bernardi, "Ab initio electron-two-phonon scattering in GaAs from next-to-leading order perturbation theory", Nat. Commun. **11**, 1–7 (2020). DOI: https://doi.org/10.1038/s41467-020-15339-0.
H.-Y. Chen contributed to the theory derivation.

[7] H.-Y. Chen, V. A. Jhalani, M. Palummo, and M. Bernardi, "Ab initio calculations of exciton radiative lifetimes in bulk crystals, nanostructures, and molecules", Phys. Rev. B **100**, 075135 (2019). DOI: 10.1103/PhysRevB.100.075135.
H.-Y. Chen contributed to theory derivations, code implementations, numerical calculations, and manuscript writing.

[8] V. A. Jhalani, H.-Y. Chen, M. Palummo, and M. Bernardi, "Precise radiative lifetimes in bulk crystals from first principles: the case of wurtzite gallium ni-

tride", J. Condens. Matter Phys. **32**, 084001 (2019). DOI: https://doi.org/10.1088/1361-648X/ab5563.
H.-Y. Chen contributed to the theory derivation.

[9] H.-Y. Chen, M. Palummo, D. Sangalli, and M. Bernardi, "Theory and ab initio computation of the anisotropic light emission in monolayer transition metal dichalcogenides", Nano Lett. **18**, 3839–3843 (2018). DOI: 10.1021/acs.nanolett.8b01114.
H.-Y. Chen contributed to theory derivations, code implementations, numerical calculations, and manuscript writing.

TABLE OF CONTENTS

Acknowledgements . . . iii
Abstract . . . vii
Published Content and Contributions . . . x
Table of Contents . . . xi
List of Illustrations . . . xiv
List of Tables . . . xv
Chapter I: Introduction . . . 1
1.1 Research Statement . . . 1
1.2 Methodology . . . 5
1.3 Thesis Outline . . . 11
Chapter II: Exciton Radiative Properties . . . 12
2.1 Theoretical Approach for Exciton Radiative Lifetimes . . . 13
2.2 Benchmark Calculations in Gas Molecules and Bulk GaAs . . . 21
2.3 Anisotropic Light Emission in 2D Monolayer Transition Metal Dichalcogenides . . . 26
2.4 Exciton Radiative Lifetime in h-BN Defect Structures . . . 32
2.5 Exciton Recombination and Dissociation in 3D Wurtzite GaN . . . 37
2.6 Conclusion . . . 44
Chapter III: Exciton-Phonon Interaction and Ultrafast Dynamics . . . 46
3.1 Theory and Numerical Method . . . 48
3.2 Exciton-Phonon Signature in Bulk Hexagonal Boron Nitride . . . 54
3.3 Exciton-Phonon Dynamics in Monolayer Tungsten Diselenide . . . 66
3.4 Joint Study on Exciton-Phonon Relaxation in Monolayer Tungsten Diselenide . . . 72
3.5 Conclusion . . . 78
Chapter IV: Conclusion and Future Directions . . . 81
Appendix A: Second Quantization of Light in Anisotropic Materials . . . 85
Appendix B: Derivation of the Radiative Recombination Rate in Isotropic 3D Materials . . . 88
Appendix C: Derivation of the Radiative Recombination Rate in 2D Materials 90
Appendix D: Derivation of the Radiative Recombination Rate in 0D Systems 93
Appendix E: Radiative Lifetime of Excitons with Linear Dispersion . . . 94
Appendix F: Numerical Information for the Computation of Excitons in 2D Hexagonal Boron Nitride Defects . . . 95
Appendix G: Electron-Phonon Interaction in First-Order Perturbation Theory 96
Appendix H: Numerical information for Ex-ph dynamics Calculation in Hexagonal Boron Nitride . . . 98
Appendix I: Numerical information for Ex-ph dynamics Calculation in Monolayer Tungsten Diselenide . . . 100

Appendix J: Excitonic tr-ARPES Spectrum in Log-Scale in Monolayer Tungsten Diselenide 102
Bibliography 103

LIST OF ILLUSTRATIONS

Number *Page*

1.1 Dyson equation for the one-electron Green's function. 7
1.2 The Bethe-Salpeter equation 9
2.1 Schematic of the exciton and photon quantities 16
2.2 Chosen target molecules 22
2.3 Exciton radiative lifetimes in GaAs 25
2.4 Anisotropic Photoluminescence in 2D TMD 28
2.5 Exciton decohnerence signature in Photoluminecense 32
2.6 DFT transition energy of defect states in 2D h-BN 35
2.7 Exciton radiative lifetime of selected defects in 2D h-BN 36
2.8 Exciton intrinsic lifetimes 42
2.9 Exciton effect lifetimes with eciton dissociation effect in GaN 43
3.1 Schematic of the exciton-phonon interaction 53
3.2 Exciton-phonon dynamics numerical workflow 54
3.3 Absorption spectrum of bulk h-BN 55
3.4 Ex-ph self-energy diagram 56
3.5 Ex-ph relaxation time and scattering rate 59
3.6 Ex-ph relaxation and coupling strength map 61
3.7 Temperature dependence of ex-ph scattering rate 62
3.8 Phonon-assisted photoluminescence diagram 64
3.9 Phonon-assisted photoluminescence in h-BN 65
3.10 Bright exciton linewidth in WSe_2 68
3.11 Phonon-assisted photoluminescence in WSe_2 69
3.12 Exciton depolarization in WSe_2 from BTE 71
3.13 Exciton band structure in monolayer WSe_2 73
3.14 Snap shots of exciton relaxation process and ARPES spectrum 75
3.15 Momentum-resolved intervalley carrier dynamics. 77
3.16 Exciton scattering map in WSe_2 79
C.1 Exciton ratiation phase space 91
H.1 Convergence of ex-ph scattering rate calculation 99
I.1 Substrate effect on exciton energy in WSe_2 101
J.1 Snap shot of predicted ARPES in log-scale 102

LIST OF TABLES

Number *Page*

2.1 Radiative lifetimes for chosen molecules 23
2.2 Exciton properties in selected 2D h-BN defects 36

Chapter 1

INTRODUCTION

1.1 Research Statement

Background

Dating back to 1930s, when researchers studied the optical properties of insulators, energy dilution was found during the light absorption. Comparing the energy quanta with the atomic vibration mode, Frenkel concluded the energy transfer among atoms to be in the form of "electron excitation wave" rather than the common heat carrier, Debye wave, i.e. the phonon [1, 2]. The excitation consists of an electron outside the closed electronic shell and a relic hole replacing the absent electron state. Due to the opposite charge between them, the electron-hole pair forms a neutral bound state and is no longer confined to any certain atom. Therefore, the pair locating at a single atomic site can hop to neighboring atom and carry way the energy, resulting the energy dissipation. This "excitation wave" today is called the *Frenkel Exciton*.

This idea was further generalized to semiconductors [3, 4] where the electron doesn't belong to a single atom but has wave function spreading in the crystal, and the electron closed shells mixes with each other forming the valence band. Contradictory to metals, semiconductors have finite dielectric constant ($\varepsilon = 1 \sim 10$) such that the electron and hole can form bound state with radius across several unit cells without dissociating into free particles. Further, provided the electron-hole pair nearly freely moving in the crystal under mutual Coulomb attraction, excitons in semiconductor have the equation of motion identical to the hydrogen atom, having the discrete spectrum indexed by principal quantum number. To emphasize the fundamental difference of its long electron-hole separation and hydrogen-like energy level compared to Frenkel exciton, exciton of thie kind is called the *Wannier-Mott Exciton*.

The signature of the excitonic effect is commonly realized in optical process. In direct-gap semiconductor, the lowest lying exciton state equals to the optical excited the electron-hole pair. The formation of exciton requires less energy than the among for a valence electron to jump to the conduction band, which lowers the threshold of the photon absorption. The difference between this "optical gap" and the true

electronic gap equals to the exciton binding energy which characterizes the stablility of exciton in a thermal bath [5, 6]. In general, the exciton binding energy is of 0.1-1 eV for Frenkel exciton and ~10 meV for Wannier-Mott exciton. Beside the renormalization on the band gap, the formation of exciton also re-constructs the transition dipole. The hydrogen-like equation of motion imposes symmetries on exciton such that the optical transition is required to obey parity conditions. Electron-hole in exciton states following correct parity can recombine by photon emission. They possess a stronger dipole moment than the normal Bloch wave state in crystal and result in a resonant pole in the absorption spectrum. This kind of exciton is called the *bright exciton* for its high optical sensitivity. Otherwise, excitons robust under optical perturbation are called *dark exciton*. Besides the dipole, exciton can have different reasons for being dark. The first one is the relative spin between the electron and hole. In non-magnetic system with weak spin-orbital coupling, spin component along certain direction is a good quantum number. Since light emission conserves the electronic spin, only the electron-hole pair in the spin-singlet form can radiatively recombine while the spin-triplet exciton remains dark. This spin-forbidden exciton can be "brightened" by external magnetic field and observed in the magento-photoluminescence experiment [7, 8]. The other case is the indirect exciton in which has electron and hole locate at different points in the Brillouin zone [5]. The finite momentum difference forbids the light emission which can violate the momentum conservation since photon momentum is in general negligible compared to the crystal wave vectors. In semiconductor of indirect band gap, the lowest lying exciton is an indirect state such that the bright exciton resonant peak only appears in the absorption spectrum but absent in the emission one. Nevertheless, the indirect exciton can still contribute to the optical response once electronic states couple to the lattice vibration. By absorbing or emitting phonons, the exciton can transfer the exceeding momentum to atoms and meet the momentum restriction for optical process [9]. Early studies were performed on the absoprtion spectra [10–12] while more on photoluminescence (PL) rencetly [13–15].

In early semiconductor technology, the application of excitons is limited by their weak binding energy; No stable exciton feature can operate in room temperature. This difficulty was overcome until the break through in the synthesis of low dimensional nano structure, mainly like graphene, carbon nanotube and two-dimensional transition metal dichalcogenide (TMD) family [16–18]. The reduction of the dimension weakens the screening effect, promoting the Coulomb interaction by orders of magnitude. Further, in the confined 2D system, the modified effective potential

has weaker short range attraction [19] which leaves the exciton Bohr radius to be in order of a few nanometers when the binding energy is of ~500 meV. Excitons in nano structure is then categorized between the Frenkel exciton and the Wannier-Mott exciton and possess advantages from both of them, including stability at room temperature [20], domination in the optical response [21, 22], and mobility for transport properties [23, 24].

Current application of exciton mainly focus on the optical device. Optoelectronics uses the strong electric field or injects electron and hole through p-n junction to foster the formation of exciton and control the following light emission intensity. This technique realizing exciton as the light emission source is matured on III-V semiconductors, including GaAs, GaP, and InP, and more recently III-nitride semiconductors (GaN, InN, AlN) as well as their alloy, in the form of quantum dot, while the engineering on 2D heterostructure makes the TMD the emerging candidate for next generation light emitter [25–30]. In terms of the opposite process, the exciton also brings out a revolution in light absorption device, mainly the solar cell [31]. The formation of exciton provides a different mechanism from conventional silicon based solar cell in which the photon generated free electron-hole pair is separated at the designed p-n junction to create the electric potential. In excitonic solar cell, with the energy offset at a heterointerface matches with the optical gap of the material, the stable exciton in bulk will dissociate at this "electronic trap site", separating the electron and hole into different sides of the interface. This new design utilizing the exciton binding energy can break the limit of photovoltage met in conventional solar cell. Current excitonic solar cell researches are focusing on the organic materials [32, 33] while design based on 2D TMD is also proposed as ultrathin and ultralight photovoltaic devices [34, 35].

Exciton also promises new method for information storage. Current memory device use the electron spin up/down to store binary information, while researchers are looking for new binary quantum states for new information storing bits. One of the candidate is the "valley" degree of freedom, denoting the inequivalent conduction band minimum in the Bernoulli zone which can be controlled by applying symmetry-breaking strain or magnetic field to manipulate the electronic states [36, 37]. Early studies focused on Silicon and AlAs [38–40] but had no decisive advantage to industrialize this valleytronics technique over the conventional spintronics. Recent progress on excitonic physics in 2D TMD provides the valleytronics an opportunity to challenge the lead of spintronics again [41, 42]. The spin-valley locking effect

in 2D TMD provides a polarization selection rule in the light emission/absorption process; the light with opposite circular polarization can couple to electron-hole pair in different valley exclusively [43]. Enhanced by exciton effect, this strong light-valley coupling can serve as an high efficient readout tool which is not accessible in AlAs [44]. Further, this light-controlled bit can be easier to integrate as qubit for the application in quantum computing [45, 46]. However, the sensitivity to light shortens the lifetime of the valley degree of freedom [47, 48], making the information storage unstable and impractical. Thus, current research on TMD valleytronics are seeking for long lifetime time exciton which can sustain the spontaneous and external decoherence, like heterobilayer interlayer exciton [49, 50] and defect-bound exciton [51, 52].

Problems & Research Subjects

Current understanding on exciton physics is progressing with the advance of synthesis, engineering and spectroscopic technology. However, pure experimental approach is insufficient to fully reveal the properties of excitons. For instance, the light emission efficiency is controlled by the quantum yield (QY) which is determined by the ratio of exciton radiative lifetime and the non-radiative relaxation time and highly depends on the sample quality. Different synthesis methods and sample preparations can result in totally opposite conclusion due to inevitable factors like impurities and interaction from the substrate [53, 54]. Besides, experiment measurement always contain a thermal average effect which can only be lowered in cryogenic system but never excluded. The effective quantity may not sufficient to represent the intrinsic property and, in some examples, can deviate from the true value by orders of magnitude [48]. Thus, theoretical approach is mandatory to study the intrinsic behavior of the electronic state without influence from environment.

Beyond the intrinsic exciton traits, the underlying mechanism connecting microscopic properties and macroscopic quantities, like QY and PL, is also the critical information to gain. In system of low exciton density, the exciton-phonon (ex-ph) interaction dominates the coupled dynamics while the exciton-exciton or charged carrier-exciton interaction are minor and negligible. The ex-ph interaction can be extracted indirectly from the homogeneous linewidth broadening [47] or directly by time-domain spectroscopies. However, direct measurement is challenging, for general carrier-phonon scattering occurring in femtosecond times scale, and requires ultrafast resolution. Recently, ultrafast spectroscopy are emerging as powerful tool to time stepping the electron relaxation [55–57] while some of them are applied on

exciton physics [58–60]. On the other hand, theorists using first-principle method, including density functional perturbation theory (DFPT) [61] plus Boltzmann Transport Equation (BTE) [62] and real-time Time-dependent density functional theory (rt-TDDFT) [63–65], have successfully simulated electron-atom interaction in system from molecule to extend crystal [66–68]. However, a corresponding study on exciton-phonon dynamics is still missing.

In this dissertation, we present theoretical research on exciton intrinsic radiative lifetimes, investigate the ex-ph interaction from first-principles, and shed light on their ultrafast dynamics. This work fills up the gap knowledge of the exciton radiative properties by developing a general tool to probe exciton recombination in all novel materials. Besides, this work carry out an unprecedented *ab initio* algorithm to compute the ex-ph matrix element and enable further quantitative calculations. Our development on real-time exciton relaxation simulation for the first time provide a bona fide theoretical tool to access the ultrafast exciton behavior from femtosecond to picosecond without any empirical parameters. Overall, we open up the gate to the first-principle research on exciton dynamics in the field of computational physics.

1.2 Methodology

Our methodology is based on density functional theory (DFT) [69], the GW-Bethe-Salpeter-Equation (BSE) method [70, 71], and density functional perturbation theory (DFPT) [61]. These methods are part of the mainstream first-principles tools to model the electronic structure of real materials. They are characterized by their ability to make accurate predictions using as the only input the crystal structure and atomic positions of materials. These "*ab initio*" approach are thus uniquely equipped to bridge the knowledge gap between the theory and experiment. In the following, we provide a concise discussion on each method to setup the toolbox used throughout this work.

Density Functional Theory (DFT)

Current DFT relies on the pioneering work of Hohenberg and Kohn (HK) in 1960s [72]. HK proposed that, in Schrodinger equation, all ground state properties have a one-to-one correspondence to the electron density and the external potential. This breakthrough advance has enabled a computationally convenient reformulation of the many-electron problem. In a follow-up work, Kohn and Sham (KS) [69] introduced a fictitious non-interacting many electron Hamiltonian which is expected

to have the same electron density as the target system. The resulting *Kohn-Sham Equation* is written as:

$$\left[\frac{-\hbar^2}{2m}\nabla^2 + \int d\mathbf{r}' \frac{n(\mathbf{r}')}{|\mathbf{r}-\mathbf{r}'|} + v_{\text{ext}}(\mathbf{r}) + v_{xc}[n(\mathbf{r})]\right]\psi_i(\mathbf{r}) = E_i[n(\mathbf{r})]\psi_i(\mathbf{r}) \tag{1.1}$$

where the second term is the Hartree potential from the mean-field electron density, the third term is the electric attraction from the nuclei, and $n(\mathbf{r}) = \sum |\psi_i(\mathbf{r})|^2$ is the electron density. The last term in the LHS is the auxiliary "*exchange-correlation*" potential encoding electronic interactions beyond the Hartree term. According to the HK-theorem, once the total energy is minimized with respect to the density, the one-to-one condition will guarantee that the density in the KS Hamiltonian equals that of the real many-electron system..

In principle, solving the KS-equation self-consistently can provide the exact ground state properties of the system. However, the exact form of v_{xc} is not known and thus this term needs to be approximated. Among various approximations, two widely adopted methods also used in this work are the local density approximation (LDA) [73] and the generalized gradient approximation (GGA) [74], used alternatively depending on the system at hand. Further, since calculating all the electron states in a certain atom is too costly, only the valence electrons are treated explicitly, while the core electrons, which typically do not contribute to bonding and optical transitions, are included in the pseudopotentials employed to represent the v_{ext} potential from the nuclei plus core electrons of each atom. Libraries of pseudopotentials, obtained from DFT calculations on isolated atoms, are available to DFT users and employed in this thesis work [75].

After the success of KS-equation, the concept of density in HK-theorem is generalized. The one-to-one corrspondence no longer restricted between the electron density and energy terms. The first one was proposed to solved the intrinsic Born-Oppenheimer approximation in KS's approach. Kreibich and Gross introduced the "density" of the nuclei position in a equal footing as the electron density [76] such that v_{xc} depends on both electron density and the generalized nuclei density and involves all the mutual interaction in a nonadiabatic manner. This generalization opens up a wide application of DFT. Examples like the magnetization in spin-DFT [77] and superconductivity order parameter in superconductor DFT [78, 79] can be found in literature.

This body of work has established the DFT framework as the standard approach for material modeling. Several open source codes implement DFT and related

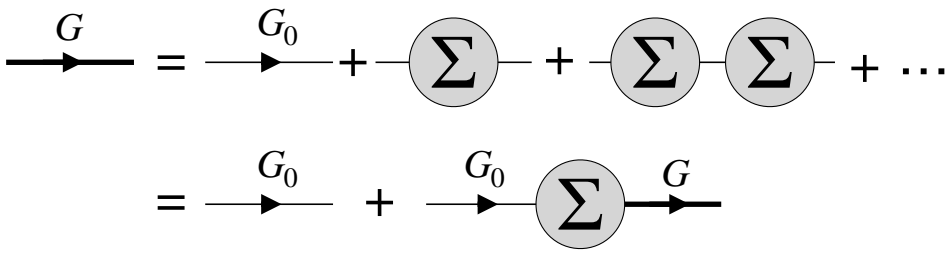

Figure 1.1: **Dyson equation for the one-electron Green's function.**

approaches, including the widely used QUANTUM ESPRESSO [80], ABINIT [81], and VASP [82] codes, which have become mainstream packages applied in the computation physics community.

GW-Bethe-Salpeter Equation (GW-BSE)

The using of approximated v_{xc} raises the insufficiency of DFT. The incapability to include the full exchange-correlation energy in general results in underestimating the band gap [70]. To correct the missed energy, the idea of quasi-particle (QP) is applied. In many-body perturbation theory (MBPT), one particle propagation is modulated by the "self-energy", which is the correction from quantum fluctuation and can be rigorous obtained based on the quantum field theory. Fig. 1.1 shows how the bare particle is dressed by the self-energy Σ and become the QP in Dyson equation. In terms of one-particle quantum mechanics, the Schrodinger equation can be written:

$$\left[\frac{-\hbar^2}{2m}\nabla^2 + v_{\text{ext}}(\mathbf{r}) + v_H(\mathbf{r})\right]\psi_i(\mathbf{r}) + \int d\mathbf{r}'\Sigma(\mathbf{r},\mathbf{r}')\psi_i(\mathbf{r}') = E_{i,\text{MBPT}}\psi_i(\mathbf{r}) \tag{1.2}$$

where the Hartree term v_H is extracted out from the self-energy Σ. The form of the self-energy depends on the coupling to be considered. In most of the cases and system discussed in this work, the main interaction is the Coulomb interaction, Thus we adpot the so called GW-approximation, using the selfenergy:

$$\Sigma = iGW, \tag{1.3}$$

where G is the QP propagator and W is the screened Coulomb potential $W = \epsilon^{-1}v_c$. By comparing Eq. (1.1) and Eq. (1.2), to the lowest order of perturbation theory we can obtain:

$$E_{i,\text{MBPT}} - E_{i,\text{DFT}} \approx \langle\psi_i|\Sigma - v_{xc}|\psi_i\rangle \tag{1.4}$$

which is the missed energy to be added back.

Besides the correction on the one-body QP energy, MBPT can also provide us the two particle propagation which corresponds to the electron-hole pair with the correct time ordering. In terms of functional derivative, the exciton Green's function can be derived from the QP propagator [83]:

$$L(12;1'2') = \frac{\delta G(1,1')[\mathcal{J}]}{\delta \mathcal{J}(2',2)}, \tag{1.5}$$

where L is the full connected four point correlation function representing the propagation of the exciton, $\mathcal{J}$ is some auxiliary nonlocal source proportional to the strength creating and annihilating particles at different space and time for which we use numbers as a composited coordinates, i.e., $1 = (\mathbf{r}_1, t_1)$. Applying the Dyson equation for one particle propagation, we arrive a Dyson-like equation for the exciton:

$$L(12;1'2') = L_0(12;1'2') + L_0(1\bar{4};1'\bar{3})K(\bar{3}\bar{5};\bar{4}\bar{6})L(\bar{6}2;\bar{5}2'), \tag{1.6}$$

which is the *Bethe-Salpeter Equation* (BSE), shown diagrammatically in Fig. 1.2. Here, we use the overlines denote dummy integration variables to simplify the notation. Compared to L, $L_0(12;1'2') = G(1,2')G(2,1')$ is its non-interacting counterpart, while the key ingredient in the BSE is the kernel $K(\bar{3}\bar{5};\bar{4}\bar{6})$, which encodes the interaction between the electron and hole. Within the GW approximation, it can be written as

$$K(35;46) = -i\delta(3,4)\delta(5^-,6)v_c(3,6) + i\delta(3,6)\delta(4,5)W(3^+,4), \tag{1.7}$$

where the first term is the exchange energy and the second is the screened Coulomb interaction.

To solve Eq. (1.6), we project the BSE in the "transition space" [83] which is Hilbert space formed by the direct product of electron and hole states which, in a periodic system, are Bloch wave functions characterized by the band index and crystal momentum. In this space, the wave function of an exciton state S with center-of-mass momentum $\mathbf{Q}$ can be written as

$$|S\mathbf{Q}\rangle = \sum_{vc\mathbf{k}} A^{S\mathbf{Q}}_{vc\mathbf{k}} |v\mathbf{k}\rangle_h |c\mathbf{k}+\mathbf{Q}\rangle_e \ , \tag{1.8}$$

where v labels the valence and c the conduction bands, $\mathbf{k}$ is the electron crystal momentum, and the subscripts e and h denote electron and hole states, respectively[1].

[1] We apply the Tamm-Dancoff approximation, which ignores antiresonant transition terms [84].

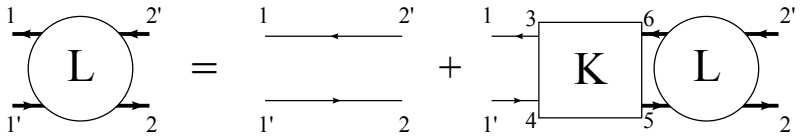

Figure 1.2: **The Bethe-Salpeter equation** in its Dyson form, shown using Feynman diagrams. For details, see Ref. [83].

Applying Eq. (1.8) to write down the Lehmann representation of Green's function in Eq. (1.6), we can convert the self-consistent BSE into an effective Hamiltonian [83, 85]:

$$(E_{c\mathbf{k+Q}} - E_{v\mathbf{k}})A^{S\mathbf{Q}}_{vc\mathbf{k}} + \sum_{v'c'\mathbf{k}'} K_{vc\mathbf{k},v'c'\mathbf{k}'}A^{S\mathbf{Q}}_{v'c'\mathbf{k}'} = E_S(\mathbf{Q})A^{S\mathbf{Q}}_{vc\mathbf{k}}, \tag{1.9}$$

where $E_{c\mathbf{k+Q}}$ and $E_{v\mathbf{k}}$ are the electron and hole quasiparticle energies, and the kernel $K_{vc\mathbf{k},v'c'\mathbf{k}'}$ can be written in the electron-hole basis as [85]:

$$K_{vc\mathbf{k},v'c'\mathbf{k}'} = i\psi_{v\mathbf{k}}(\bar{4})\psi^*_{c\mathbf{k+Q}}(\bar{3})K(\bar{3}\bar{5},\bar{4}\bar{6})\psi^*_{v'\mathbf{k}'}(\bar{5})\psi_{c'\mathbf{k}'+\mathbf{Q}}(\bar{6}), \tag{1.10}$$

where $\psi_{c(v)\mathbf{k}}$ are conduction (valence) single-electron Bloch wavefunctions. The exciton expansion coefficients $A^{S\mathbf{Q}}_{vc\mathbf{k}}$ can be obtained from the eigenvector of Eq. (1.9) and the exciton energy is the corresponding eigenvalue.

In practice, the *a*b initio BSE is solved by constructing the kernel (typically from the static RPA dielectric function) and diagonalizing Eq. (1.9) with a linear algebra package. Several codes implement this workflow, including Yambo [86], Abinit [87], and BerkeleyGW [88].

Density Functional Perturbation Theory (DFPT)

Lattice vibration mode, i.e. the phonon, and its interaction with carriers is the base to study the dynamics of electrons, holes, and excitons. The general idea about the atomic vibration is derived from the Tylor expansion of the total energy respective to the atom displacement:

$$E(\{\mathbf{u}_s(l)\}) = E_0 + \frac{1}{2}\sum_{sl\alpha,tm\beta}\frac{\partial^2 E}{\partial u^\alpha_s(l)\partial u^\beta_t(m)}u^\alpha_s(l)u^\beta_t(m), \tag{1.11}$$

where $u^\alpha_s(l)$ is the atomic displacement away from the equilibrium position of s-th atom in the l-th unit cell along α-direction. With the position indices s and l converted into momentum space, the dynamical matrix, $\partial^2 E/\partial u\partial u$, can be solved

to obtain the characteristic frequency and collective atomic motions of a lattice vibration quanta with a specific momentum $\mathbf{q}$.

Several first-principle methods have been developed, like the multicomponent DFT [76] and finite-displacement approach in the TDDFT [63]. Among them, the density functional perturbation theory (DFPT) [61], which solves the linear atomic perturbation (the Sternheimer equation [89]) in the KS-equation, stands out with their computational advantage. DFPT can calculate the atom vibration eigenmode under any wavelength without the construction of supercell.

DFPT also benefits in providing the electron-phonon matrix element [62]. During solving the Sterheimer equation, the deformation potential is also computed from the change of KS-potential:

$$\Delta V^{\mathrm{KS}} = \sum_{sl\alpha} \frac{\partial V^{\mathrm{KS}}}{\partial u_s^{\alpha}(l)} u_s^{\alpha}(l), \tag{1.12}$$

where V^{KS} is the collection of all potential terms in KS-equation, Eq. (1.1). With the phonon solution, obtained from diagonalization of the dynamical matrxi, we can rewrite the displacement function by the phonon operator in terms of second quantization:

$$u_s^{\alpha}(l) = \sum_{\nu\mathbf{q}} \left(\frac{\hbar}{2M_s \omega_{\nu\mathbf{q}} \mathcal{N}} \right)^{1/2} \mathrm{e}_{\nu\mathbf{q}}^{s\alpha} e^{i\mathbf{q}\cdot\mathbf{R}_l} \left(\hat{b}_{\nu\mathbf{q}} + \hat{b}_{\nu-\mathbf{q}}^{\dagger} \right) \tag{1.13}$$

where $\mathcal{N}$ is the number of unit cell, M_s is the mass of s-th atom in the l-th unit cell locating at $\mathbf{R}_l$, $\omega_{\nu\mathbf{q}}$ and $\hat{b}_{\nu\mathbf{q}}$ are the frequency and the operator for the ν-th phonon mode with momentum $\mathbf{q}$ with $\mathrm{e}_{\nu\mathbf{q}}^{s\alpha}$ being the atom displacement along α in the phonon mode. Under this representation, the electron-phonon coupling constant characterizing the transition from Bloch state $|n\mathbf{k}\rangle$ to $|m\mathbf{k}+\mathbf{q}\rangle$ can be written down:

$$g_{mn\nu}(\mathbf{k},\mathbf{q}) = \frac{1}{\sqrt{2\omega_{\nu\mathbf{q}}}} \langle m\mathbf{k}+\mathbf{q} | \Delta_{\nu\mathbf{q}} V^{\mathrm{KS}} | n\mathbf{k} \rangle \tag{1.14}$$

with

$$\Delta_{\nu\mathbf{q}} V^{\mathrm{KS}} = \sum_{s\alpha} \frac{\mathrm{e}_{\nu\mathbf{q}}^{s\alpha}}{\sqrt{M_s}} \sum_{l} \frac{e^{i\mathbf{q}\cdot\mathbf{R}_l}}{\sqrt{\mathcal{N}}} \frac{\partial V^{\mathrm{KS}}}{\partial u_s^{\alpha}(l)}. \tag{1.15}$$

Throughout this work, we use the QUANTUM ESPRESSO [80] code to carry out the DFT and DFPT calculate to obtain the basic electron wave function, band energy and the phonon quantities. For exciton, we use the YAMBO [86] code to build and solve the BSE to get the exciton energy and coefficient. When discussing carrier dynamics, we use the PERTURBO [90] to calculate the electron-phonon matrix element.

1.3 Thesis Outline

Based on the first-principles approaches for excitons introduced above, this thesis presents forefront research on exciton radiative and non-radiative dynamics, with each topic articulated into separate chapters.

In chapter 2, we focus on the topic of exciton radiative emission. We first provide a derivation of exciton radiative lifetimes for materials with any dimensioinality, from bulk to nanostructure and isolated system (Sect. 2.1). Following the theoretical study and a benchmark of this approach (Sect. 2.2), we present a series of applications, including the prediction of the anisotropic PL in monolayer transition metal dichalcogenide (Sect. 2.3), determinaing defect structures in monolayer boron nitride (Sect. 2.4), and analysis on the temperature dependence of exciton radiative lifetime in bulk gallium nitride (Sect. 2.5). The theoretical approach we have developed is general and can be applied to crystalline materials of any dimension and symmetries. The applications of this framework shed light on specific open problems related to light emission in bulk crystal and nanostructured materials.

In chapter 3, we focus on the exciton-phonon interaction and exciton dynamics. We first provide a rigorous derivation of the exciton-phonon coupling in the framework of ab initio electron-phonon interactions and BSE excitons. We then introduce the workflow and numerical implementation (Sect. 3.1). With the ex-ph coupling in hand, we apply the method to study exciton relaxation, PL, and emission linewidth in bulk hexagonal boron nitride and monolayer tungsten diselenide (Sect. 3.2 and Sect. 3.3). Last, we present a joint theory-experiment effort on understanding ultrafast exciton dynamics and the related photoemission spectroscopic signatures in monolayer tungsten diselenide (Sect. 3.4).

In chapter 4, we summarize the thesis work and outline future research directions.

Chapter 2

EXCITON RADIATIVE PROPERTIES

This chapter contains contents from following publications:

[1] H.-Y. Chen, M. Palummo, D. Sangalli, and M. Bernardi, "Theory and ab initio computation of the anisotropic light emission in monolayer transition metal dichalcogenides", Nano Lett. **18**, 3839–3843 (2018). DOI: 10.1021/acs.nanolett.8b01114.

[2] H.-Y. Chen, V. A. Jhalani, M. Palummo, and M. Bernardi, "Ab initio calculations of exciton radiative lifetimes in bulk crystals, nanostructures, and molecules", Phys. Rev. B **100**, 075135 (2019). DOI: 10.1103/PhysRevB.100.075135.

[3] V. A. Jhalani, H.-Y. Chen, M. Palummo, and M. Bernardi, "Precise radiative lifetimes in bulk crystals from first principles: the case of wurtzite gallium nitride", J. Condens. Matter Phys. **32**, 084001 (2019). DOI: https://doi.org/10.1088/1361-648X/ab5563.

[4] S. Gao, H.-Y. Chen, and M. Bernardi, "Radiative properties and excitons of candidate defect emitters in hexagonal boron nitride", NPJ Comput. Mater. 2020 (Accepted for publication) (2020),

Exciton as a photon-excited electronic state has proved its importance in optical absorption process [85]. The formation of exciton creates large oscillator strength, resulting in the strong resonant pole at exciton energy in the absorption spectrum. However, the research on the inverse process, i.e. light emission during the exciton recombination, is still lacking. In particular, the radiative lifetime featuring the stability of the exciton is an essential quantity for future application as light emitter and information storage. Currently, calculations of radiative properties typically employ simplified empirical models that can only qualitatively explain or fit the experimental data [91, 92], or are carried out in the independent-particle picture [93, 94], neglecting excitons altogether. While desirable, first-principles approaches that can accurately predict exciton radiative recombination and light emission are still in their infancy − only a few examples exist in the literature [48, 95].

These approaches employ the *a*b initio Bethe-Salpeter equation (BSE) [83, 85] as a starting point to compute the exciton radiative lifetimes. A calculation of this kind was proposed by Spataru et al. [95] to compute the radiative lifetimes in a

one-dimensional (1D) system (carbon nanotubes) and was followed by Palummo et al. [48] with the discussion in novel two-dimensional (2D) semiconductors which enabled accurate predictions of the exciton radiative lifetimes, as well as their temperature dependence. However, for the main light emitters of technological interest, including bulk crystals, molecules, single quantum emitters, quantum dots, and other zero-dimensional (0D) systems, an *ab initio* approach for computing exciton recombination and the associated radiative lifetimes has not yet been rigorously derived.

In this chapter, we carry out an universal treatment to compute exciton radiative lifetimes and demonstrate three applications in nanotechnologies each of their own interest in the field. We first derive and review exciton radiative lifetime formula in bulk crystals, 2D and 1D materials, and 0D isolated systems in Sect. 2.1. In Sect. 2.2, we present our benchmark calculation in gallium arsenide (GaAs) crystal and in chosen gas phase organic molecules. In Sect. 2.3, we extend the lifetime formalism in 2D system to photon emission and predict the anisotropic PL in 2D-TMDs. In Sect. 2.4, we present the application on identifying the defect structure in monolayer hexagonal boron nitride (h-BN). Sect. 2.5 studies the exciton radiative lifetime in wurtzite gallium nitride (GaN), followed by conclusions in Sect. 2.6.

2.1 Theoretical Approach for Exciton Radiative Lifetimes

In this section, we first depict a general approach to compute the exciton radiative lifetimes and discuss the formula in systems of different dimensions, respectively. The derivation starts from the exciton wavefunction, Eq. (1.8) obtained by solving the BSE, Eq. (1.9). With the wavefunction $|S\mathbf{Q}\rangle$ for an exciton in state S with center-of-mass momentum $\mathbf{Q}$, we use the minimal coupling Hamiltonian to describe the interaction between electrons and photons, $H_{int} = -\frac{e}{m}\mathbf{A}\cdot\mathbf{p}$, where $\mathbf{p}$ is the momentum operator and $\mathbf{A}$ the vector potential in second quantized form which is reviewed in Appendix A (here and below, e and m are the electron charge and mass, respectively, and we use SI units) [96]. The radiative recombination rate at zero temperature can be written using Fermi's golden rule as

$$\begin{aligned}\gamma_S(\mathbf{Q}) &= \frac{2\pi}{\hbar}\sum_{\lambda\mathbf{q}}\left|\langle G, 1_{\lambda\mathbf{q}}|H_{int}|S\mathbf{Q},0\rangle\right|^2\delta(E_S(\mathbf{Q})-\hbar\omega_{\lambda\mathbf{q}}) \\ &= \frac{\pi e^2}{\epsilon_0 m^2 V}\sum_{\lambda\mathbf{q}}\frac{1}{\omega_{\lambda\mathbf{q}}}\left|\mathbf{e}_{\lambda\mathbf{q}}\cdot\mathbf{p}_S(\mathbf{Q})\right|^2\delta(E_S(\mathbf{Q})-\hbar\omega_{\lambda\mathbf{q}}),\end{aligned} \tag{2.1}$$

where the initial state $|S\mathbf{Q}, 0\rangle$ consists of an exciton and zero photons, and the final state $|G, 1_{\lambda\mathbf{q}}\rangle$ is the electronic ground state plus one emitted photon with polarization λ and wavevector $\mathbf{q}$, and V is the volume of the system. The summation runs over the two photon polarizations and all possible wavevectors $\mathbf{q}$ of the emitted photon, which has energy $\hbar\omega_{\lambda\mathbf{q}}$, while the delta function imposes energy conservation. The transition dipole $\mathbf{p}_S(\mathbf{Q}) = \langle G|\mathbf{p}|S\mathbf{Q}\rangle$ is in general a vector with complex-valued components (in 2D and 1D systems, the only nonzero components are those in the plane or line containing the material, respectively). In practice, we use the velocity operator and compute the transition dipole as $\mathbf{p}_S(\mathbf{Q}) = (-im/\hbar)\langle G|[\mathbf{x}, H_{\mathrm{KS}}]|S\mathbf{Q}\rangle$ to correctly include the nonlocal part of the Kohn-Sham Hamiltonian, H_{KS} [97]. For light emission, the values of $\mathbf{Q}$ compatible with energy conservation are very small. For this reason, we approximate the dipole of an exciton $|S\mathbf{Q}\rangle$ as $\mathbf{p}_S(\mathbf{Q}) \approx \mathbf{p}_S(0)$ by solving the BSE at $\mathbf{Q} = 0$.

The radiative lifetime at finite temperature T for a given exciton state S can be computed by assuming that the exciton momentum $\mathbf{Q}$ has a thermal equilibrium distribution, which is a good approximation when (as is common) the thermalization process is much faster than radiative recombination [98]. We can thus write the radiative rate of the exciton state S as the thermal average

$$\langle\gamma_S\rangle(T) = \frac{\int d\mathbf{Q}\; e^{-E_S(\mathbf{Q})/k_BT}\,\gamma_S(\mathbf{Q})}{\int d\mathbf{Q}\, e^{-E_S(\mathbf{Q})/k_BT}}. \tag{2.2}$$

The radiative lifetime is defined as the inverse of the radiative rate, $\langle\tau_S\rangle = \langle\gamma_S\rangle^{-1}$. We employ an isotropic effective mass approximation for the exciton dispersion,

$$E_S(\mathbf{Q}) = E_S(0) + \frac{\hbar^2 Q^2}{2M_S}, \tag{2.3}$$

where the exciton mass M_S is approximated as the sum of the electron and hole effective masses, $M_S = m_e^* + m_h^*$.

Note that the exciton dispersion and effective mass tensor can also be computed (rather than assumed) by solving the BSE with a finite exciton momentum [99, 100]; this is particularly important in those cases in which a non-parabolic exciton dispersion is expected. For example, Cudazzo et al. [101] have shown that in 2D materials the exciton dispersion can be either linear or parabolic, depending on the character of the exciton wavefunction at finite $\mathbf{Q}$, and Qiu et al. [100] have shown that of the two lowest-energy bright excitons in MoS_2, one has a linear and the other a parabolic dispersion. Here we focus on computing the radiative

lifetime for excitons with a parabolic dispersion, and show in Appendix E the corresponding results for excitons with a linear dispersion. In the following, we will also assume that the exciton mass is large enough for us to set in the delta functions $E_S(\mathbf{Q}) - \hbar\omega_{\lambda\mathbf{Q}} \approx E_S(0) - \hbar\omega_{\lambda\mathbf{Q}}$.

When only the lowest-energy bright exciton contributes to the PL, Eq. (2.2) is a good approximation for the radiative rate. When multiple exciton states are occupied, an additional average is needed to include the contributions from all occupied exciton states. Assuming that the exciton states are occupied according to a thermal equilibrium distribution, the effective radiative rate one expects to observe experimentally is:

$$\langle\gamma(T)\rangle_{eff} = \frac{\sum_S \langle\gamma_S\rangle e^{-E_S(0)/k_BT}}{\sum_S e^{-E_S(0)/k_BT}}. \tag{2.4}$$

Below, we derive the exciton radiative recombination rate as a function of temperature in materials with different dimensionality. The key quantities employed in the derivations, including the coordinates, the exciton momentum $\mathbf{Q}$ and transition dipole $\mathbf{p}_S$, and the photon polarization vectors $\mathbf{e}_{\lambda\mathbf{q}}$, are shown schematically in Fig. 2.1 for each case discussed below. The equations for the bulk and 0D cases are derived here from scratch, while the 2D and 1D cases, which have been previously investigated, are reviewed briefly for completeness.

Bulk (3D) Materials

We consider a non-magnetic and non-absorbing [1] anisotropic bulk crystal, in which the static (zero-frequency) dielectric tensor can be written as

$$\boldsymbol{\epsilon}_r = \mathrm{diag}(\epsilon_x, \epsilon_y, \epsilon_z). \tag{2.5}$$

In crystals with cubic, tetragonal, orthorhombic and hexagonal symmetry, we orient the crystallographic axes along the $\{x, y, z\}$ cartesian directions, and in the uniaxial (tetragonal and hexagonal) cases we additionally orient the principal axis along the z direction. In crystal classes with lower symmetry, including monoclinic and triclinic, we orient the principal axes (i.e., the eigenvectors of $\boldsymbol{\epsilon}_r$) along the cartesian directions. With these choices, our treatment is general and can account for any crystal symmetry [102]. The photon energy in such an anisotropic material is modified according to the dielectric tensor. For a given photon wavevector $\mathbf{q}$ =

[1] For the sake of studying light emission, this assumption has negligible effects as it amounts to neglecting re-absorption or other dynamical processes of the emitted photons.

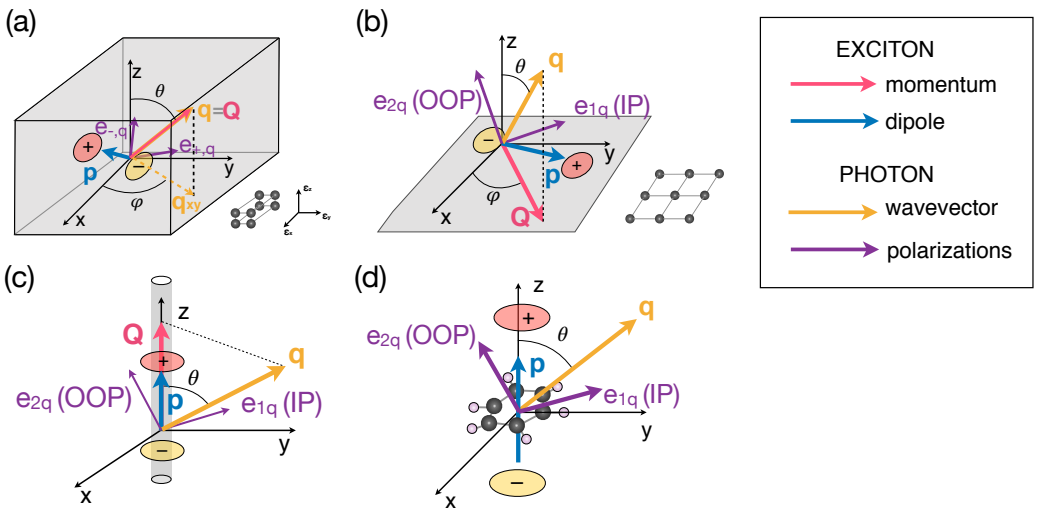

Figure 2.1: **Schematic of the exciton and photon quantities.** Each panel corresponds to a different dimensionality. (a) Bulk (three-dimensional) anisotropic material, in which momentum conservation requires $\mathbf{q} = \mathbf{Q}$, and the photon polarizations are nondegenerate and specified by the solution of the Maxwell equations [see Eq. (A.15) in Appendix A]. (b) Two-dimensional material, in which the exciton transition dipole $\mathbf{p}_S$ lies in the xy plane containing the material, and the in-plane projection of the emitted photon wavevector equals the exciton momentum, namely $\mathbf{Q} = (\mathbf{q} \cdot \hat{Q})\hat{Q}$. (c) One-dimensional material, where both the exciton momentum and transition dipole lie along the material direction z, and momentum conservation imposes $\mathbf{Q} = \mathbf{q} \cdot \hat{z}$. (d) Isolated (zero-dimensional) system, with no constraints on the exciton momentum, photon wavevector and transition dipoles. In all cases, when the two photon polarizations are degenerate, the polarization vectors $\mathbf{e}_{\lambda\mathbf{q}}$ are chosen as in-plane (IP) and out-of-plane (OOP), where the IP component is in the xy plane and the OOP in the $\mathbf{q} - \hat{z}$ plane.

(q_x, q_y, q_z), there are two propagating modes as solutions to Maxwell's equations; they correspond to the two photon polarizations [103], and their frequencies $\omega_{\pm\mathbf{q}}$ are the solutions of Eq. (A.15) in Appendix A:

$$\omega^2_{\pm\mathbf{q}} = \frac{-\left(\frac{\bar{q}_x^2}{\epsilon_x} + \frac{\bar{q}_y^2}{\epsilon_y} + \frac{\bar{q}_z^2}{\epsilon_z}\right) \pm \tilde{\omega}^2_{\mathbf{q}}}{2\mu_0\epsilon_0}, \tag{2.6}$$

with

$$\tilde{\omega}^2_{\mathbf{q}} = \sqrt{\left(\sum_\alpha \frac{\bar{q}_\alpha^2}{\epsilon_\alpha}\right)^2 - 4q^2 \sum_\alpha \frac{q_\alpha^2 \epsilon_\alpha}{\epsilon_x \epsilon_y \epsilon_z}}\,, \tag{2.7}$$

where α denotes the cartesian coordinates $\{x, y, z\}$, and $\bar{q}_\alpha^2 = q_\alpha^2 - q^2$. The corresponding polarization vectors for the two modes are

$$\mathbf{e}_{\pm\mathbf{q}} = \frac{1}{\Lambda_q}\begin{pmatrix} q_x(\omega_{\pm\mathbf{q}}^2\,\mu_0\epsilon_0\epsilon_x - q^2) \\ q_y(\omega_{\pm\mathbf{q}}^2\,\mu_0\epsilon_0\epsilon_y - q^2) \\ q_z(\omega_{\pm\mathbf{q}}^2\,\mu_0\epsilon_0\epsilon_z - q^2) \end{pmatrix} \tag{2.8}$$

up to a normalization constant Λ_q; for details, see Appendix A. This solution applies to photons propagating in anisotropic materials with $\epsilon_x \neq \epsilon_y \neq \epsilon_z$. For materials with axial or cubic symmetry, in which, respectively, two or three of the diagonal components of the macroscopic dielectric tensor are equal, the frequencies and polarization vectors have simpler expressions, which can be derived from the general case discussed here.

For an exciton in state $|S\mathbf{Q}\rangle$ with momentum $\mathbf{Q} = (Q_x, Q_y, Q_z)$, we obtain the radiative recombination rate by applying Fermi's Golden rule [see Eq. (2.1)]. Momentum conservation fixes the emitted photon wavevector to $\mathbf{q} = \mathbf{Q}$ [see Fig. 2.1(a)], and the summation over λ adds together the contributions from the $\omega_{\pm\mathbf{q}}$ solutions. As mentioned before, we approximate the transition dipole by evaluating it at $\mathbf{Q} = 0$,

$$\langle G|\mathbf{p}|S(\mathbf{Q})\rangle \approx \langle G|\mathbf{p}|S(0)\rangle = p_{Sx}\hat{\mathbf{x}} + p_{Sy}\hat{\mathbf{y}} + p_{Sz}\hat{\mathbf{z}}, \tag{2.9}$$

with complex components $p_{S\alpha}$. Using these results, the exciton radiative recombination rate at zero temperature becomes

$$\gamma_S^{3\mathrm{D}}(\mathbf{Q}) = \frac{\pi e^2}{\epsilon_0 m^2 V} \times \sum_{\lambda=\pm}\left|\sum_\alpha \frac{p_{S\alpha}\, q_\alpha(\omega_{\lambda\mathbf{Q}}^2\mu_0\epsilon_0\epsilon_\alpha - q^2)}{\Lambda_q}\right|^2 \frac{\delta\left(E_S(\mathbf{Q}) - \hbar\omega_{\lambda\mathbf{Q}}\right)}{\omega_{\lambda\mathbf{Q}}}. \tag{2.10}$$

Next, we specialize our discussion to cubic or isotropic materials with a dielectric constant ϵ [i.e., with dielectric tensor $\boldsymbol{\epsilon}_r = diag(\epsilon, \epsilon, \epsilon)$]. Radiative lifetime calculations for an axial symmetric bulk crystal will be presented in Sect. 2.5. Due to symmetry, in the cubic or isotropic case the two modes in Eq. (2.6) become degenerate, with polarization vectors perpendicular to each other and to the direction of photon propagation. For a consistent notation for later discussion, we orient one of the two polarization vectors to lie in the xy plane, and call this vector "in-plane" (IP). The other polarization vector then has a nonzero z component, and is called "out-of-plane" (OOP). These two polarization vectors can be written in spherical coordinates as

$$\mathrm{IP} \quad : \quad \mathbf{e}_{1\mathbf{q}} = \frac{1}{\sqrt{\epsilon}}(-\sin\varphi, \cos\varphi, 0)$$

$$\text{OOP} \quad : \quad \mathbf{e}_{2\mathbf{q}} = \frac{1}{\sqrt{\epsilon}}(-\cos\theta\cos\varphi, -\cos\theta\sin\varphi, \sin\theta), \tag{2.11}$$

where θ is the polar and φ the azimuth angle of the photon wavevector $\mathbf{q}$ [see Fig. 2.1(a)]. Substituting in Eq. (2.10), we obtain the radiative rate at zero temperature for cubic or isotropic bulk materials (see Appendix B):

$$\gamma_S^{\text{3D, iso}}(\mathbf{Q}) = \frac{\pi e^2}{\epsilon_0 m^2 V c\, Q\sqrt{\epsilon}} \left\{ \left| \frac{p_{Sx}Q_y - p_{Sy}Q_x}{Q_{xy}} \right|_{\text{IP}}^2 + \left| \frac{Q_x p_{Sx} + Q_y p_{Sy}}{Q_{xy}} \frac{Q_z}{Q} - p_{Sz}\frac{Q_{xy}}{Q} \right|_{\text{OOP}}^2 \right\} \delta\left(E_S(Q) - \frac{\hbar c Q}{\sqrt{\epsilon}} \right). \tag{2.12}$$

The radiative recombination rate of a given exciton state S at temperature T, for isotropic bulk crystals under the assumption that the exciton momentum has a thermal equilibrium distribution, is obtained using Eq. (2.2) as (see Appendix B)

$$\langle \gamma_S^{\text{3D, iso}} \rangle(T) = \frac{8\sqrt{\pi\epsilon}\, e^2 \hbar\, p_S^2}{3\epsilon_0 m^2 V E_S(0)^2} \left(\frac{E_S(0)^2}{2M_S c^2 k_B T} \right)^{3/2}, \tag{2.13}$$

where the exciton energy $E_S(0)$ and the transition dipole $\mathbf{p}_S$ (and $p_S^2 = |\mathbf{p}_S|^2$) are obtained by solving the BSE. The $T^{-3/2}$ temperature dependence of the radiative rate (and thus, the $T^{3/2}$ temperature dependence of the radiative lifetime) is consistent with previous semiempirical theoretical treatments [104] and with low-temperature experimental data [105].

For bulk crystals with a low exciton binding energy (< 0.1 eV), additional thermal effects include exciton dissociation and equilibration with free carriers [98]. This topic has been studied extensively experimentally and will be discussed further in Sect. 2.5; the net effect of the coexistence between excitons and carriers is an increase in the radiative lifetime, which can be important near room temperature and can cause the radiative lifetime to deviate significantly from the $T^{3/2}$ trend [105]. Such coupled exciton-carrier dynamics can be treated with kinetic models but is still beyond the reach of first-principles calculations.

Two-Dimensional Materials

Novel 2D semiconductors, such as TMDs and related layered materials, exhibit unique optical properties and strongly bound excitons that govern their light absorption and emission [106]. Exciton radiative lifetime study in 2D system has been carried out before [48], and here we provide a review for completeness. The exciton

recombination in 2D is still following the Fermi Golden rule in Eq. (2.1). However, due to the lower dimensionality, the transition dipole is restricted to the 2D plane containing the material:

$$\mathbf{p}_S = p_{Sx}\hat{\mathbf{x}} + p_{Sy}\hat{\mathbf{y}}, \tag{2.14}$$

with complex components p_{Sx} and p_{Sy}. Furthermore, since translation symmetry applies only in the plane containing the material, momentum conservation is imposed on the in-plane projection of the emitted photon wavevector, using $(\mathbf{q}\cdot\hat{Q})\hat{Q} = \mathbf{Q}$ [see Fig. 2.1(b)]. Unlike the bulk case, photons are emitted into the vacuum surrounding the 2D material (unless a substrate is present), and thus the emitted photons exhibit two degenerate polarizations for which, following the same convention as in the isotropic bulk case, we choose the IP and OOP polarizations as in Eq. (2.11) with $\epsilon = 1$. Upon integrating over all final photon states, we obtain the radiative recombination rate of an exciton S with momentum $\mathbf{Q}$ in a 2D material at zero temperature (See Appendix C):

$$\gamma_S^{2\mathrm{D}}(\mathbf{Q}) = \gamma_S^{2\mathrm{D}}(0)\cdot\left(\frac{E_S(0)}{\sqrt{E_S^2(Q)-\hbar^2c^2Q^2}}\right) \times\left\{\left|-\frac{p_{Sx}}{p_S}\sin\varphi+\frac{p_{Sy}}{p_S}\cos\varphi\right|_{\mathrm{IP}}^2+\frac{E_S(Q)^2-\hbar^2c^2Q^2}{E_S(Q)^2}\left|\frac{p_{Sx}}{p_S}\cos\varphi+\frac{p_{Sy}}{p_S}\sin\varphi\right|_{\mathrm{OOP}}^2\right\}, \tag{2.15}$$

where $\gamma_S^{2\mathrm{D}}(0) = \frac{e^2p_S^2}{\epsilon_0 m^2 cAE_S(0)}$ is the recombination rate for $\mathbf{Q} = 0$ and A is the area of the system in the xy plane. Note that due to momentum conservation there is an upper limit of Q_0 to the momentum of an exciton that can recombine radiatively; this limit occurs when a photon is emitted in the plane of the material, in which case $E_S(\mathbf{Q}) = \hbar cQ_0$. Excitons with momentum $Q > Q_0$ cannot emit a photon, and their radiative recombination rate vanishes since energy and momentum cannot be simultaneously conserved upon photon emission.

At finite temperature T, the exciton radiative lifetime can be computed by assuming, similar to the bulk case, a parabolic exciton dispersion $E_S(\mathbf{Q}) = E_S(0)+\frac{\hbar^2Q^2}{2M_S}$, where M_S is an in-plane isotropic exciton effective mass. Taking the thermal average in Eq. (2.2) of the 2D radiative rate in Eq. (2.15), we obtain the radiative lifetime:

$$\langle\tau_S^{2\mathrm{D}}\rangle(T) = \gamma_S^{2\mathrm{D}}(0)^{-1}\times\frac{3}{4}\left(\frac{2M_Sc^2k_BT}{E_S(0)^2}\right). \tag{2.16}$$

This formula has been applied by Palummo et al. [48], giving temperature dependent radiative lifetimes in excellent agreement (within 5−10 %) with experimental results

obtained by transient photoluminescence. Gao et al. [107] also recently applied this formula to study light emission in bilayer TMDs. A similar equation was also employed by Cudazzo et al. [108] to investigate light emission in 2D materials, but it employed a prefactor that is incorrect for the 2D case.

One-Dimensional Materials

Excitons have been studied extensively in 1D materials, and first-principles calculations of exciton radiative lifetimes have been employed to investigate light emission in single-walled carbon nanotubes [95, 109]. Since defects and intertube interactions broaden and wash out the exciton spectrum, measuring exciton lifetimes is challenging in carbon nanotubes, and *ab initio* calculations have provided key microscopic insight into exciton recombination in carbon nanotubes [95].

In a 1D material, such as a nanotube or nanowire, the dimensionality constrains the exciton transition dipole to the direction of the material, which we take to be the z direction. The transition dipole can then be written as $\mathbf{p}_S = p_{Sz}\hat{\mathbf{z}}$, and momentum conservation along the z axis imposes a condition on the emitted photon wavevector, $\mathbf{q} \cdot \hat{\mathbf{z}} = \mathbf{Q}$, for the recombination of an exciton with momentum $\mathbf{Q}$ [see Fig. 2.1(c)]. Using Fermi's Golden rule in Eq. (2.1), the exciton decay rate in a 1D material at zero temperature can be written as [95]:

$$\gamma_S^{1D}(\mathbf{Q}) = \gamma_S^{1D}(0) \cdot \frac{E_S(\mathbf{Q})^2 - \hbar^2 c^2 Q^2}{E_S(\mathbf{Q})^2}, \tag{2.17}$$

where $\gamma_S^{1D}(0) = \frac{e^2 p_{Sz}^2}{\epsilon_0 m^2 \hbar c^2 L_z}$ and L_z is the length of the system along the z direction. The radiative recombination rate decreases monotonically with Q, and is zero when $Q_0 = E_S(Q_0)/\hbar c$. Similar to the 2D case, $Q = Q_0$ is an upper limit to the exciton momentum for radiative recombination, and excitons with $Q > Q_0$ cannot recombine radiatively and emit light.

The finite temperature radiative rate is computed using the thermal average in Eq. (2.2). Assuming a parabolic exciton dispersion, the exciton radiative lifetime in a 1D material reads

$$\langle \tau_S^{1D} \rangle (T) = \gamma_S^{1D}(0)^{-1} \times \frac{3}{4} \left(\frac{\sqrt{2\pi M_S k_B T}}{E_S(0)/\hbar c} \right). \tag{2.18}$$

Using this equation, Spataru et al. obtained radiative lifetimes in carbon nanotubes in good agreement with experiment [95].

Atoms, Molecules, and Other Isolated (0D) Systems

We refer to an atom, molecule, quantum dot or other isolated light emitter as a 0D system [see Fig. 2.1(d)]. The approach presented here applies to both these isolated emitters and to atoms, ions or other single quantum emitters embedded in an isotropic material. Since there is no translation symmetry, the crystal momentum can be taken to be zero and ignored, and we keep only one quantum number to denote the discrete energy levels. Using these conventions, we rewrite the exciton wavefunction Eq. (1.8) as

$$|S\rangle = \sum_{vc} A^S_{vc} |v\rangle_h |c\rangle_e, \tag{2.19}$$

where v and c are quantum numbers associated with occupied and unoccupied orbitals, respectively. In general, when there are no symmetry constraints, the transition dipole is a complex vector, as in Eq. (2.9). When the system is embedded in an isotropic material with dielectric constant ϵ (for the 0D system in vacuum, one should set $\epsilon = 1$), Fermi's Golden rule gives the exciton recombination rate at zero temperature (see Appendix D):

$$\gamma_S^{0\mathrm{D}} = \frac{\sqrt{\epsilon} e^2 p_S^2 E_S}{3\pi\epsilon_0 m^2 c^3 \hbar^2}. \tag{2.20}$$

In CGS units, in which $\epsilon_0 = 1/4\pi$, we recover the known result $\gamma_S^{0\mathrm{D}} \propto 4/3\, p_S^2 E_S$ for the radiative rate of an isolated emitter or a defect embedded in a crystal [110], which is also known as the Einstein A coefficient [111] in the thermodynamic treatment of light emission. While light is quantized in our approach, we obtain the same formula as in Dexter's work in Ref. [110], where radiation is treated classically. Due to the absence of crystal momentum for an isolated emitter, all the excitons satisfying the selection rules with nonzero transition dipole can undergo an optical transition and emit a photon. At finite temperature, since there is no momentum, we take a thermal average only over different exciton states [using Eq. (2.4)], and obtain for the effective radiative recombination rate:

$$\langle \gamma^{0\mathrm{D}}(T) \rangle_{eff} = \frac{\sqrt{\epsilon} e^2}{3\pi\epsilon_0 m^2 c^3 \hbar^2} \frac{\sum_S p_S^2 E_S e^{-E_S/k_B T}}{\sum_S e^{-E_S/k_B T}}. \tag{2.21}$$

2.2 Benchmark Calculations in Gas Molecules and Bulk GaAs

To our knowledge, there are no examples in the literature of *ab initio* calculations of radiative lifetimes in bulk crystals and 0D isolated systems within the BSE

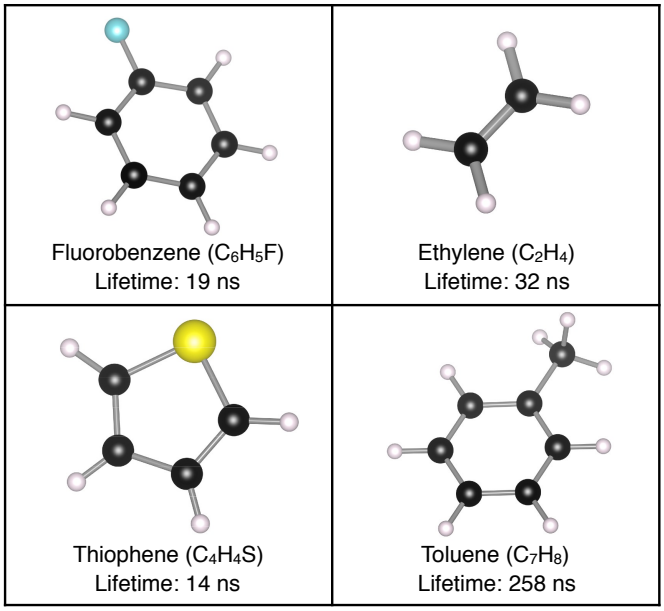

Figure 2.2: **Chosen target molecules.** The four molecules studied in this work – fluorobenzene, ethylene, thiophene and toluene – and their computed exciton radiative lifetimes.

framework. We apply our approach to compute from first principles the exciton radiative lifetimes in a bulk isotropic crystal of GaAs and in several small organic molecules in the gas phase to setup the benchmark of the developed formalism. With supporting data from previous work [48, 112] and provided in the following, this first-principle approach based on BSE can set its credibility in the computation of exciton radiative lifetimes.

Gas Molecules

For the gas-phase organic molecules, we use the experimental structure in all four cases — fluorobenzene, ethylene, thiophene, and toluene (see Fig. 2.2), and carry out calculations at the Γ-point only. The DFT calculations employ the PBE exchange-correlation functional [74] and a 90 Ry kinetic energy cutoff; we employ cubic simulation cells with sizes between 33 – 38 Bohr and use a truncated Coulomb interaction. In the BSE calculations, we use a 7 Ry cutoff for the statically screened Coulomb interaction, together with GW-corrected electron energy levels and up to 180 empty states to accurately converge the low-energy excitons.

We apply the radiative lifetime formula, Eq. (2.21), and compare our results with available experimental data [113] in Table 2.1. The predicted exciton lifetimes are

	τ (ns)	τ_{exp} (ns)	p_S^2 ($\times 10^6$)
Fluorobenzene	19	12 – 23	7.54
Toluene	258	185	0.59
Ethylene	32	–	4.59
Thiophene	14	–	11.5

Table 2.1: **Radiative lifetimes for chosen molecules.** Comparison of our computed radiative lifetimes, $\tau = (\gamma^{0D})^{-1}$ obtained using Eq. (2.20), with experimental data from Ref. [113]. For fluorobenzene, the experimental lifetime is given as a range, which is obtained by combining data from Refs. [117, 118] and the quantum yield from Ref. [119]. The symbol "–" means that we could not find experimental data. The square transition dipoles are provided in the last column in atomic units.

within a factor of 2 of the measured values, and thus in very good agreement with experiment. We find radiative lifetime of order 10–30 ns in fluorobenzene, ethylene and thiophene; the lifetime in toluene is significantly longer, roughly 250 ns and thus an order of magnitude longer than in the other molecules. To explain this trend, we show in Table 2.1 that the square of the transition dipole of the lowest bright exciton is an order of magnitude smaller in toluene than in the other molecules; since the radiative lifetime is inversely proportional to the square dipole [see Eq. (2.20)], the weaker transition dipole explains the longer lifetime in toluene. The simple intuition is that in molecules like toluene with small transition dipoles the electron and hole wavefunctions have a small overlap. Future work will attempt to correlate the lifetimes and dipoles with the molecular structure and exciton wavefunctions in a wider range of molecular structures.

One factor contributing to the small discrepancy with experiment is that we compute the radiative rate using the ground state molecular structure rather than its excited-state counterpart. The molecular structure typically relaxes in the excited state from which light is emitted [114], leading to the so-called Stokes shift – a redshift between the absorption onset and emission energy – which can be sizable in small organic molecules. Since the exciton energies and transition dipoles are modified by the structural relaxation, these effects are expected to account for at least part of the small discrepancy between our computed radiative lifetimes and the experimental values. Future work will employ recently developed methods to relax the molecular structure in the excited state [115, 116] and investigate how the structure impacts the radiative lifetimes.

The formulas we obtain can be applied using transition dipole matrix elements that may or may not include electron-hole interactions. But correctly treating excitons through the BSE is essential whenever the exciton binding energy is sizeable and whenever the low-energy optical transitions are excitonic in nature, which is the case in most molecules and nanomaterials, and in crystals with a large band gap or low dielectric screening. For example, for the gas-phase molecules, in which the independent-particle picture fails altogether to describe the optical excitations due to the large exciton binding energy, neglecting the electron-hole interaction leads to large errors in the optical spectra and also in the lifetimes. In toluene, the lowest bright exciton is the 27th eigenstate of the BSE Hamiltonian in order of increasing energy; it has an energy of 4.92 eV and a lifetime of 258 ns (versus an experimental value of 185 ns). By contrast, the 27th transition in the independent-particle Hamiltonian gives a lifetime of 83,000 seconds; the lowest bright transition in the independent-particle picture has an energy of 8.2 eV and a lifetime of 350 ns. Therefore, it is clear that the independent-particle approximation for radiative lifetimes in molecules gives large and uncontrolled errors, and that correctly treating the excitons with the BSE is essential for computing radiative lifetimes in molecules.

GaAs

For GaAs, we perform DFT calculations on the relaxed zincblende structure, employing the PBEsol exchange-correlation functional [120]. We use fully relativistic norm-conserving pseudopotentials generated with Pseudo Dojo [75], and include spin-orbit coupling in all calculations. The BSE is solved on a $30\times30\times30$ **k**-point grid with a rigid scissor shift applied to the DFT band structure to match the experimental band gap [121]. We use a 6 Ry cutoff for the statically screened Coulomb interaction and the highest 4 valence bands and lowest 2 conduction bands to converge the low-energy excitons. In the radiative lifetime calculations, to remove a possible source of error we use experimental values for the static dielectric constant and effective masses [121, 122]. Due to the light electron mass, which leads to a steep conduction band valley, fully converging the radiative lifetimes in GaAs requires very fine Brillouin zone grids with a large computational cost. Using a double-grid technique, Kammerlander et al. [123] have shown that a $40\times40\times40$ **k**-point grid is sufficient to converge the BSE absorption spectrum. Since the radiative lifetimes depend on the energy and transition dipole of the lowest-energy excitons, the **k**-point convergence of the lifetimes is similar to that of the absorption spectrum. Using the standard BSE (without the double-grid technique of Ref. [123]), the finest

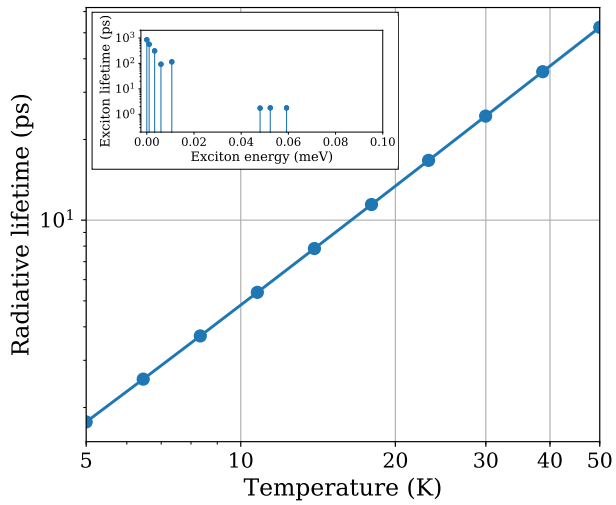

Figure 2.3: **Exciton radiative lifetimes in GaAs.** Computed radiative lifetimes in a GaAs crystal, shown as a function of temperature up to 50 K. The lifetimes are obtained using the thermal average in Eq. (2.4). The inset shows the excitons contributing to the thermal average along with their individual lifetimes at 10 K. In the inset, the zero of the energy axis is taken to be the lowest exciton energy.

grid we were able to reach is a $30 \times 30 \times 30$ **k**-point grid, which took over $10,000$ CPU cores to compute. Since our grid is close to the fully converged $40 \times 40 \times 40$ **k**-point grid, it allows us to obtain results close to convergence. Further refinement of the GaAs radiative lifetimes given here may be possible by using finer grids, though their computational cost is at present prohibitive. The computed radiative lifetimes in GaAs as a function of temperature are shown in Fig. 2.3. They are obtained as the thermal average in Eq. (2.4) of the BSE exciton radiative rates for a bulk isotropic crystal in Eq. (2.13). The inset of Fig. 2.3 shows the low-energy excitons contributing to this thermal average; the lowest 5 excitons are dark and associated with spin-forbidden transitions, and the 3 bright excitons at a slightly higher energy also contribute to the average. The dark states increase the average radiative lifetime by an order of magnitude compared to the average lifetime of the bright excitons alone.

The computed BSE radiative lifetimes are of order 1−50 ps below 50 K, and exhibit the $T^{3/2}$ trend expected for bulk crystals at low temperature [105]. Comparing these results with experiment is not simple. In GaAs, the radiative processes are known to be affected by the coupling of excitons with phonons and free electron-hole pairs, resulting in an intricate nonequilibrium dynamics that is still the subject of debate [124–126]. The interaction with phonons is particularly important in GaAs,

where exciton-phonon scattering is thought to provide the momentum needed by excitons to transition toward the radiative region [124, 125]. For this reason, the photoluminescence decay is expected to be much slower than the intrinsic exciton radiative lifetimes computed here. Consistent with this view, the measured photoluminescence decay times are a few ns at low temperatures [124–126], while our computed radiative lifetimes are a few ps in the same temperature range. This result confirms that the long lifetimes observed in GaAs by measuring the photoluminescence decay are the result of nonequilibrium exciton dynamics rather than an intrinsic exciton lifetime. Future work will investigate the coupled nonequilibrium dynamics of excitons and phonons, which will enable quantitative comparisons with photoluminescence data.

With supporting data from previous work [48, 112] and provided above, the first-principle approach based on BSE has set its credibility in the computation of exciton radiative lifetimes. In the following, we explore three applications in modern optic-technology based on the knowledge of exciton radiative lifetime.

2.3 Anisotropic Light Emission in 2D Monolayer Transition Metal Dichalcogenides

2D-TMDs are atomically thin semiconductors with chemical formula MX_2 (M=Mo or W, and X=S, Se, or Te) in the hexagonal lattice. Monolayer TMDs generally possess direct gaps, while their bulk types have indirect gaps [127, 128]. Monolayer TMDs can absorb light strongly [129] and emit light efficiently with intense photoluminescence (PL) quantum yield [53, 129, 130]. Thus, the TMD now serves a role as a promising material for applications in nanotechnologies, such as photodetectors, optoelectronics, and valleytronics [21, 22, 48, 53, 106, 129, 131–134]. While their radiative recombination has been investigated using time-resolved spectroscopy [59, 135–137] and *ab initio* calculations [48], microscopic understanding of light emission in 2D-TMDs remains incomplete.

The lack of inversion symmetry in monolayer TMDs leads to two inequivalent valleys at the K and K′ corners of the hexagonal Brillouin zone. Locking between the spin and valley degrees of freedom due to the strong spin-orbital splitting in valence band introduces optical valley selection rules [138–140], whereby circularly polarized light can be employed to selectively generate excitons in a specific valley, while linearly polarized light can excite excitons in a quantum superposition of the two valleys [41, 43, 44, 140, 141]. In terms of the inverse process, exciton in a

single K-valley can emit circularly polarized PL, and a superposition state of them can emit linearly polarized one. However, different from the circularly polarized counterpart, the linearly polarized PL is anisotropic [142–144] and exhibits an angular dependence that is still not completely understood. Provided the correlation between PL and microscopic exciton quantum state, theory and experiments have shed light on valley decoherence [142, 145–149], but quantifying exciton coherence and the PL remains an open problem. Since the anisotropic PL could enable novel light-emitting, optoelectronic, and photovoltaic devices, understanding exciton dynamics, decoherence, and light emission is critical to advancing 2D-TMDs.

Here, we derive and compute the radiative rates as a function of photon emission direction and polarization in monolayer TMDs based on the formalism developed in Sect. 2.1. The lowest-energy eigenvectors of the BSE are rotated in their degenerate subspace to form excitons with different valley superposition states. Polar plots of the PL generated when these excitons recombine can explain recent PL measurements under excitation with linearly polarized light, and predict new light emission regimes. Our approach is general, and it enables *ab initio* calculations of the PL in 2D semiconductors. Our results advance microscopic understanding of light emission in 2D-TMDs, explaining their PL anisotropy and its link to valley polarization and decoherence.

We carry out density functional theory (DFT) calculations within the generalized gradient approximation [74] using the QUANTUM ESPRESSO code [80]. Experimental lattice parameters are used, together with fully relativistic pseudopotentials that include the spin-orbit coupling and treat semi-core states as valence electrons[2] [48, 150]. The YAMBO code [86] is employed to solve the BSE using a $33\times33\times1$ **k**-point grid, and a rigid shift of the conduction band DFT eigenvalues is applied to obtain quasiparticle bandstructures computed in GW method [48].

We compute the dependence of the radiative rate on the polar angle θ between the photon emission direction and the layer normal (see Fig. 2.1). Using $E_S(Q)\approx E_S(0)$ due to the very small exciton momentum inside the light cone, together with simple geometric arguments, we have:

$$\frac{\sqrt{E_S^2(Q)-\hbar^2c^2Q^2}}{E_S(0)} \approx \frac{\sqrt{E_S^2(Q)-\hbar^2c^2Q^2}}{E_S(Q)} = \cos\theta. \tag{2.22}$$

[2]Orbitals of valence electrons are 5s2, 5p6, 5d4, and 6s2 for tungsten and 4s2 and 4p4 for Selenium.

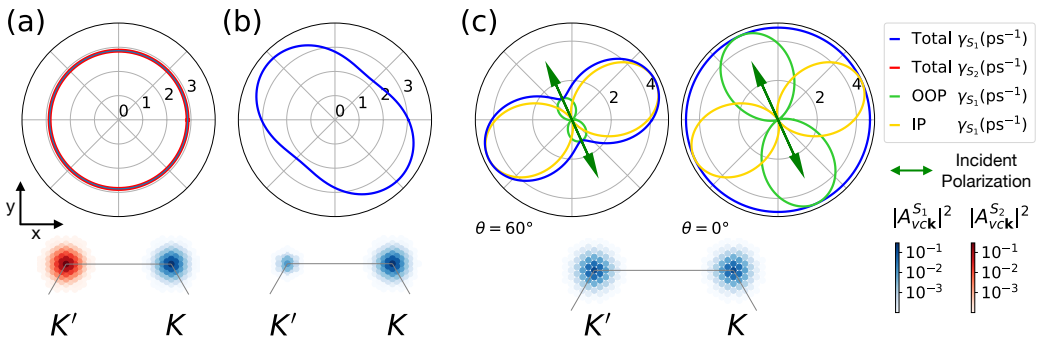

Figure 2.4: **Anisotropic photoluminescence in 2D TMD.** Polar plots of the radiative rates, and the corresponding exciton wavefunctions, shown for several cases. (a) Two distinct excitons entirely located, respectively, on the K and K′ valleys, and their isotropic radiative rate. (b) Exciton with unequal weights on the K and K′ valleys, and the resulting anisotropic radiative rate and PL emitted for $\theta = 60°$. (c) Exciton with equal weights on the K and K′ valleys, as generated by linearly polarized light, and its radiative rate emitted at a polar angle $\theta = 60°$ (left panel) and along the layer normal at $\theta = 0°$ (right panel). The rates for OOP and IP polarized light emission are shown along with their sum. The arrow shows the polarization direction of incident light.

Substituting in Eq. (2.15), and using $\gamma_S(\theta,\phi) = \gamma_S(\mathbf{Q})\cos(\theta)$ (see Appendix C), we obtain the radiative rates for light emitted with IP and OOP polarizations:

$$\gamma_S^{\mathrm{IP}}(\theta,\varphi) \;=\; \gamma_S(0)\left|-\frac{p_{Sx}}{p_S}\sin\varphi+\frac{p_{Sy}}{p_S}\cos\varphi\right|^2 \tag{2.23}$$

$$\gamma_S^{\mathrm{OOP}}(\theta,\varphi) = \gamma_S(0)\cos^2\theta\left|\frac{p_{Sx}}{p_S}\cos\varphi+\frac{p_{Sy}}{p_S}\sin\varphi\right|^2. \tag{2.24}$$

Since the intensity of light emitted at a given angle is proportional to the radiative rate, these equations can provide polar plots of the PL. The IP and OOP contributions, which can be measured separately in experiments able to discern the PL polarization, can be added together to obtain the total PL intensity.

An important point is that the lowest-energy exciton responsible for light emission (so-called bright A $1s$ exciton [21, 48]) is two-fold degenerate in 2D-TMDs due to the valley degeneracy. These degenerate excitons, called here $|S_1\rangle$ and $|S_2\rangle$, are orthogonal but randomly oriented in their degenerate subspace when the BSE Hamiltonian is diagonalized numerically at $\mathbf{Q} = 0$. They can be rotated in the degenerate subspace to new states $|S_i'\rangle = \mathbf{M}_{ij}|S_j\rangle$ using a unitary matrix $\mathbf{M}$ in SU(2) [151]:

$$\mathbf{M}(u,\theta_1,\theta_2) = \begin{pmatrix} u & \sqrt{1-|u|^2}e^{i\theta_1} \\ -\sqrt{1-|u|^2}e^{-i(\theta_1-\theta_2)} & u^* e^{i\theta_2} \end{pmatrix} \tag{2.25}$$

where u, θ_1 and θ_2 are independent parameters defining the transformation. Since excitons are represented by coefficients $A^S_{vc\mathbf{k}}$ in the electron-hole basis employed to solve the BSE [85, 86], the rotation is accomplished by transforming the exciton coefficients as $(A^{S'_1}_{vc\mathbf{k}}, A^{S'_2}_{vc\mathbf{k}})^T = \mathbf{M} \cdot (A^{S_1}_{vc\mathbf{k}}, A^{S_2}_{vc\mathbf{k}})^T$, where T is the transpose.

In the following, the transformed excitons $|S'_i\rangle$ are chosen as those physically relevant in selected excitation scenarios of interest. The square modulus of their coefficients, $|A^{S'_i}_{vc\mathbf{k}}|^2$, define the probability to find the exciton in the K and K′ valleys. The exciton dipoles, by virtue of their definition $\mathbf{p}_{S_i} = \langle G|\mathbf{p}|S_i\rangle$, transform in the same way as the exciton states, namely $\mathbf{p}'_i \equiv \mathbf{p}_{S'_i} = \mathbf{M}_{ij}\mathbf{p}_{S_j}$. The dipoles $\mathbf{p}'_{1,2}$ of the transformed excitons determine their radiative rate through Eq. (2.15).

Fig. 2.4 shows different excitation and light emission scenarios. For each case, we plot the exciton weights $\left|A^S_{vc\mathbf{k}}\right|^2$ on the two valleys and the radiative rate — which is proportional to the intensity of the PL signal — as a function of in-plane light emission angle φ at a fixed polar angle θ. The results shown here are for WSe_2, but similar trends also hold for other 2D-TMDs.

Fig. 2.4(a) focuses on excitons generated with circularly polarized light. We transform the BSE eigenvectors to obtain two excitons $|S_{1,2}\rangle$, each located entirely on one valley. We find that the PL for these excitons is isotropic about the layer normal, regardless of the angle θ at which light emission is detected. The isotropic PL is consistent with the fact that circularly polarized photons cannot break the in-plane rotational symmetry of 2D-TMDs. In Fig. 2.4(b), we form excitons with unequal weights on the K and K′ valleys, which can be directly excited with light or result from decoherence processes. By placing more weight on either valley, the isotropic PL pattern is broken – the radiative rate becomes greater along a specific direction, and the PL is anisotropic.

Fig. 2.4(c) focuses on excitons generated with incident light linearly polarized in the $\hat{\mathbf{E}}_{\text{inc}}$ direction. We form two excitons $|S_{1,2}\rangle$ with, respectively, dipoles $\mathbf{p}_1$ parallel and $\mathbf{p}_2$ perpendicular to $\hat{\mathbf{E}}_{\text{inc}}$. With this choice, only $|S_1\rangle$ is excited since $|\mathbf{p}_2 \cdot \hat{\mathbf{E}}_{\text{inc}}| = 0$. Consistent with the optical valley rule, the resulting exciton $|S_1\rangle$ is an equal superposition state of the K and K′ valleys, further proving the validity of our rotation procedure. The IP and OOP polarized emission rates, along with their sum, are shown for two emission polar angles, $\theta = 60°$ and $\theta = 0°$. The IP polarized emission is stronger than the OOP at $\theta = 60°$, leading to a total PL that is anisotropic and maximal in the in-plane direction normal to the incident polarization. For $\theta = 0°$ (i.e., in the layer-normal direction) the two contributions are equal in magnitude and

the resulting PL is isotropic. Both the IP and OOP polarizations lie in the xy plane in the $\theta \to 0$ limit, and the emitted photons are polarized in the $\hat{\mathbf{E}}_{\text{inc}}$ direction.

As seen from Eq. (2.23) and Eq. (2.24), the OOP and IP radiative rates and PL signals are rotated by $\varphi = \pi/2$ with respect to one another, and their ratio is:

$$\frac{\gamma_S^{\text{OOP}}(\varphi + \pi/2)}{\gamma_S^{\text{IP}}(\varphi)} = \cos^2(\theta) \leq 1. \tag{2.26}$$

This result explains why recent experiments [142] observe a stronger PL signal polarized in plane compared to out of plane. When the linear polarization direction of the light that excites the sample is rotated (not shown), we find that only the total phase of the exciton wavefunction changes, and the PL pattern in Fig. 2.4(c) is unchanged but reoriented according to the linear polarization direction, in agreement with the measurements in Ref. [142].

There is an important subtlety in the interpretation of recent PL measurements [142–144]. Due to the small size of the samples, the PL is typically collected through a microscope, measured in the layer-normal direction, and then passed through a polarizer or analyzer [143, 144]. The resulting polar plots of the PL as a function of the angle α between the polarizer and the incident polarization exhibit a $\cos(2\alpha)$ trend [142–144]. In these works, we think that the dependence of the PL on the polarizer angle α has not been clearly differentiated from the PL dependence on emission direction. We stress that the PL anisotropy computed as a function of emission angle φ in Fig. 2.4(b,c) is *distinct* from the PL anisotropy measured as a function polarizer angle α, which can be readily explained with our approach.

In the $\theta \to 0$ limit probed experimentally, the radiative rate in Eq. (2.1) is $\gamma_S \propto \sum_\lambda \left|\mathbf{e}_{\lambda\mathbf{q}} \cdot \mathbf{p}_S\right|^2$. For excitation with polarization along $\hat{\mathbf{x}}$, which induces a dipole $\mathbf{p}_S = p_S\hat{\mathbf{x}}$, collecting light through a polarizer oriented at angle α gives $\gamma_S \propto p_S^2 \sum_\lambda \left|(A_\alpha \mathbf{e}_{\lambda\mathbf{q}}) \cdot \hat{\mathbf{x}}\right|^2$, where A_α is the Jones matrix [152]

$$A_\alpha = \begin{pmatrix} \cos^2\alpha & \cos\alpha\,\sin\alpha \\ \cos\alpha\,\sin\alpha & \sin^2\alpha \end{pmatrix}. \tag{2.27}$$

For $\theta \to 0$, one obtains $\gamma_S(\alpha) \propto p_S^2 \cos^2\alpha$, a result that also holds for arbitrary θ. We thus predict a PL intensity as a function of polarizer angle $I(\alpha) = I_0 \cos^2\alpha = I_0[1 + \cos(2\alpha)]/2$ (see Fig. 2.5), which explains the $\cos(2\alpha)$ angular dependence observed in the PL measurements [142–144]. By contrast, in Fig. 2.4(c) excitation with linearly polarized light yields a PL with maximal intensity in the in-plane

direction *normal* to the exciton dipole (as in classical dipole radiation) rather than parallel to the exciton dipole as in the $I(\alpha)$ plots. To our knowledge, such direction dependent measurements have not yet been carried out.

Also shown in Fig. 2.5 is the expected PL intensity including exciton decoherence effects, which has a trend of $I(\alpha) = A_1 + A_2\cos(2\alpha)$ (A_i are numerical constants). Two mechanisms can induce exciton decoherence, including T_1 relaxation processes, in which the exciton weights on the K and K′ valleys vary due to intervalley scattering, resulting in exciton wavefunctions similar to Fig. 2.4(b), and T_2 relaxation processes, in which the valley weights remain equal, but the exciton dipole — and thus the polarization — rotates by a random angle. Decoherence due to both processes opens a neck in the $I(\alpha)$ PL polar plot (see Fig. 2.5) since a polarizer placed normal to the incident polarization will measure a non-zero signal. Recent measurements of T_2 times of ~350 fs [143, 144] at low temperature, where the radiative lifetime is of order 1−10 ps [48], justify the significant loss of polarization observed experimentally [143, 144].

While we treated the bright A $1s$ exciton as two-fold degenerate, recent work has shown that two exciton branches with a very small energy difference (~1 meV in MoS_2) are present at the light cone due to the exchange interaction [100]. These exciton branches correspond to a particular basis in the nearly degenerate pseudospin space. In our notation, excitons in the lower branch with parabolic dispersion couple only to IP polarized light, and excitons in the upper branch with v-shaped dispersion only to OOP polarized light [100]. Our approach, which treats these branches as degenerate, forms a single exciton $|S_1\rangle$ that contributes to both IP and OOP polarized emission, which is equivalent to summing over the nearly degenerate branches in Ref. [100].

Our treatment generalizes the radiative rates derived in the Ref. [48] under the assumption of isotropic exciton dipoles. When $\mathbf{p}_S$ is real and oriented along the $x=y$ direction, so that p_x and p_y are equal, Eq. (2.15) reduces to the formula derived in Ref. [48], $\gamma_S(\mathbf{Q}) = \gamma_S(0)\cdot\sqrt{1-\hbar^2c^2Q^2/E_S^2(\mathbf{Q})}$ [3]. The temperature dependence of the radiative rates in Ref. [48] can also be recovered. Averaging the radiative rate in Eq. (2.15) over momentum Q and emission angle φ (see Appendix C) gives the

[3] We remark that $\gamma_S(0) = \frac{e^2p_S^2}{\epsilon_0 m^2 cAE_S(0)}$ derived here is a factor of 2 smaller than in Ref. [48], where the unit vector along the exciton dipole was taken to be $\hat{\mathbf{x}}+\hat{\mathbf{y}}$, and thus incorrectly normalized to $\sqrt{2}$ instead of 1. Note also that here we use SI units, whereas Ref. [48] uses CGS units, in which $\epsilon_0 = 1/4\pi$, and further substitutes $p_S^2 = m^2E_S^2(0)\mu_S^2/\hbar^2$.

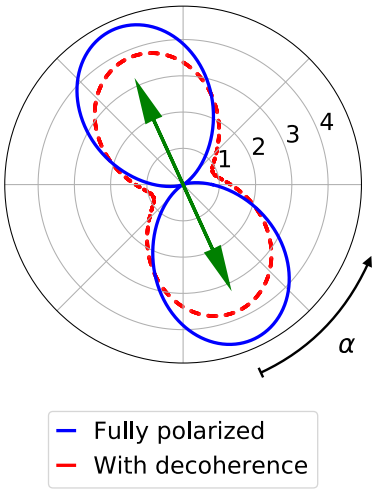

Figure 2.5: **Exciton decohnerence signature in Photoluminecense.** Polar plot of the PL as a function of the angle α between the polarizer and the incident polarization. Shown are the ideal case in which light is fully polarized along the excitation polarization direction (indicated by the arrow) and the case in which light is only partially polarized as a result of decoherence.

temperature dependent radiative lifetime derived in Ref. [48]:

$$\langle \tau_S \rangle(T) = \langle \gamma_S \rangle^{-1} = \gamma_S^{-1}(0) \cdot \frac{3}{4} \left(\frac{E_S(0)^2}{2M_S c^2 k_B T} \right)^{-1} . \tag{2.28}$$

The few ps lifetimes at low temperature and few ns room temperature lifetimes predicted with this formula in Ref. [48] have now been confirmed by several experiments [59, 135–137, 153].

In summary, in this section, we presented a general ab initio method to compute the radiative rate and PL as a function of direction and polarization in 2D semiconductors. The new treatment reveals the inherently anisotropic PL of 2D-TMDCs and its dependence on polarization, valley occupation, and decoherence. Future work can apply our approach to shed light on the PL of structurally anisotropic 2D materials, including $ReSe_2$ and black phosphorus, in which exciton anisotropy is expected to lead to novel PL regimes.

2.4 Exciton Radiative Lifetime in h-BN Defect Structures

Point defects in 2D h-BN have been found as platforms to host single-photon emitters (SPEs) [154]. Compared to defects in bulk crystals, such as diamond and silicon carbide [155–158], defects in 2D h-BN as emitters promise to be more easily ad-

dressed and controlled with a range of desirable properties, including high emission rate, room temperature stability, strong zero-phonon line (ZPL), and easy integration with other optical components [159–163].

A pressing challenge for defect emitters in 2D h-BN is identifying their atomic structure. Various possible structures have been proposed on the basis of density functional theory (DFT) calculations and their comparison with experiments [154, 164–170]. However, while DFT can provide valuable insight into the formation energy, symmetry and electronic structure of SPE defects, it cannot address key aspects of point-defect SPEs such as their excited states and radiative processes responsible for light emission. Similar to other 2D materials and their defects [129, 171, 172], optical transitions at defects in h-BN are dominated by excitonic effects [173], which require specialized first-principles calculations beyond the scope of DFT.

The BSE approach with its accurate predicting power, especially in the exciton energy and radiative lifetime, is the perfect tool to overcome the obstacle. Both properties are accessible observable in experimental setting; The exciton binding energy can be measured directly from fluorescence intensity decay, while the radiative lifetime plays an important role determining the shortest decay time constant in the second-order photon correlation function [96, 154, 161, 174]. Thus, applying the BSE method to defect emitters would enable direct comparisons between theory and experiment of the emission energy and radiative lifetime, providing valuable information to identify defect SPEs.

In this section, we employ our method developed in Sect. 2.1 to compute from first principles optical properties, transition dipoles, exciton energy and radiative lifetimes of atomic defects in h-BN. We examine a large pool of candidate SPE structures, spanning native defects and carbon or oxygen impurities, to correlate their atomic structures with their photophysics. We find that different quantum emitters exhibit radiative lifetimes spanning six orders of magnitude and emission energies from infrared to ultraviolet.

Our candidate defect structures consist of charge-neutral native defects and carbon or oxygen impurities occupying one or two atomic sites, for a total of 8 different native defects and 7 structures for each of carbon and oxygen impurities. We compute the ground state defect properties using DFT, employing fully relaxed defect atomic structures in $5 \times 5 \times 1$ supercells of monolayer h-BN. We refine the electronic structure of selected defects using GW calculations [70], followed

by BSE calculations to obtain the exciton energies and wave functions and from them the optical absorption, transition dipoles and radiative lifetimes. The detailed computation information is provided in Appendix F . In the following, we denote the defects in h-BN as $X_N Y_B$ if neighboring N and B atoms are replaced by species X and Y, respectively, where X and Y can be a vacancy (denoted by "V") or another element [154, 164]. We focus on emitters in the interior of the 2D crystal [175, 176] and do not consider defects that would likely appear at the sample edges or corners [177, 178].

The electronic energies obtained using DFT, while in general not representative of electronic or optical transitions, can be used for guidance and for estimating qualitative trends. Figure 2.6 shows the lowest spin-conserving transition (HOMO-LUMO) energy of the candidate defects, obtained from DFT, together with the emission polarization inferred from structural symmetry. The defect structures considered here exhibit three different types of local symmetries, D_{3h}, C_{2v}, and C_s. In the high symmetry D_{3h} structure, adopted by N_B, V_N, B_N, C_B, C_N, and O_N, emitted light cannot be linearly polarized. Conversely, linearly polarized emitted light, as observed experimentally in hBN SPEs [162], is possible in the C_{2v} and C_s symmetries. In the C_{2v} configuration, which is the most common among the defects investigated here, the 3-fold rotational symmetry is broken but all the atoms remain in-plane, preserving the mirror symmetry with respect to the crystal plane. The C_s symmetry found in the $V_N N_B$, $V_N C_B$, $V_N O_B$, and O_B defects is instead associated with an out-of-plane distortion that breaks the mirror symmetry about the plane. The DFT transition energies for the 22 defect structures range from 0 to 3.5 eV. In contrast, the ZPL of the measured SPEs are in the 1.6−2.2 eV energy range [162], as shown by the shaded region in Fig. 2.6. While candidate structures with D_{3h} symmetry can be ruled out, C_{2v} and C_s structures with exceedingly small or large DFT transition energies also appear unlikely on the basis of the DFT results.

Starting from the DFT ground state, for selected defects we compute the excited state properties with the GW-BSE method, obtaining the quasiparticle energies in the one-shot G_0W_0 approximation and the exciton energies and wave functions with the BSE, which captures electron-hole interaction and excitonic effects. We apply the method developed in Sect. 2.1 to compute the radiative lifetime of an exciton state from Fermi's golden rule. Generalizing Eq. (2.20) for isolated (0D) emitters to include anisotropic dielectric screening in h-BN, we obtain the radiative decay

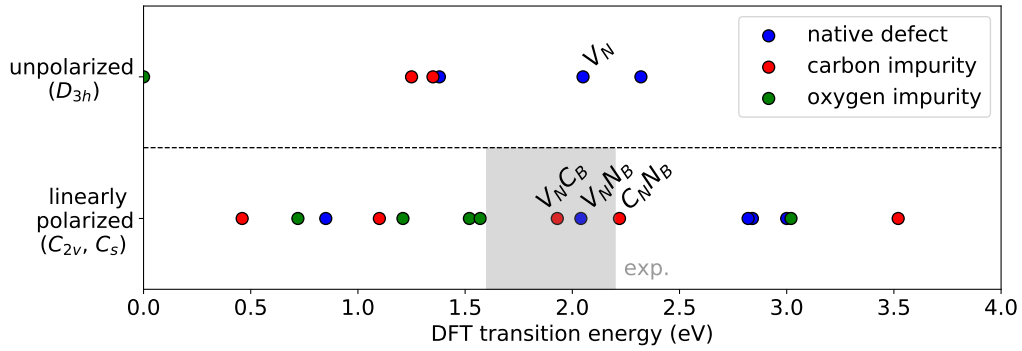

Figure 2.6: **DFT transition energy of defect states in 2D h-BN.** Distribution of the DFT transition energy, structural symmetry and emitted light polarization of 22 candidate defect structures. The shaded area shows the experimental range of values for SPEs in hBN.

rate $\gamma_S(q)$ of an exciton state S to emit photon with momentum $\mathbf{q}$:

$$\gamma_S(\mathbf{q}) = \frac{\sqrt{\epsilon_{xy}(q_{xy})}e^2 E_S}{3\pi\epsilon_0 m^2 c^3 \hbar^2}\left[\left(\frac{3}{4}+\frac{\epsilon_z}{4\epsilon_{xy}(q_{xy})}\right)|p_{S,xy}|^2+|p_{S,z}|^2\right], \tag{2.29}$$

where $\epsilon_{xy}(q_{xy})$ and ϵ_z are the in-plane and out-of-plane dielectric function of hBN, respectively, q_{xy} is the in-plane photon wavevector, E_S is the exciton energy and $p_{S,xy}$ and $p_{S,z}$ are the corresponding components of the exciton transition dipole. For monolayer h-BN we take into account the dependence on wavevector $\mathbf{q}$ as [179]:

$$\epsilon_{xy}(q) \approx 1 + 2\pi\alpha_{2D}q, \tag{2.30}$$

where α_{2D} is a constant equal to 0.4 nm [180]. In this approach, which is appropriate for 2D materials, the in-plane dielectric function of monolayer hBN reduces to a value of 1 when the wavevector q equals the wavevector of a photon at optical frequencies.

Figure 2.7 shows the computed radiative lifetimes and lowest bright exciton energies for nine selected defects, including V_N, B_N, V_NN_B, C_N, V_NC_B, C_NV_B, O_B, O_NV_B, and V_BO_N while the numerical data is summarized in Table 2.2. We find that the exciton energy can differ significantly — by as much as 1 eV — from the corresponding DFT transition energy, which fails to account for screening and electron-hole interaction effects. In addition, we find that the computed radiative lifetime for the selected structures span six orders of magnitude, from about 1 to 10^6 ns (1 ms), showing that the emission rate and brightness of quantum emitters in hBN can vary widely. The values typically found in experiments for the emission

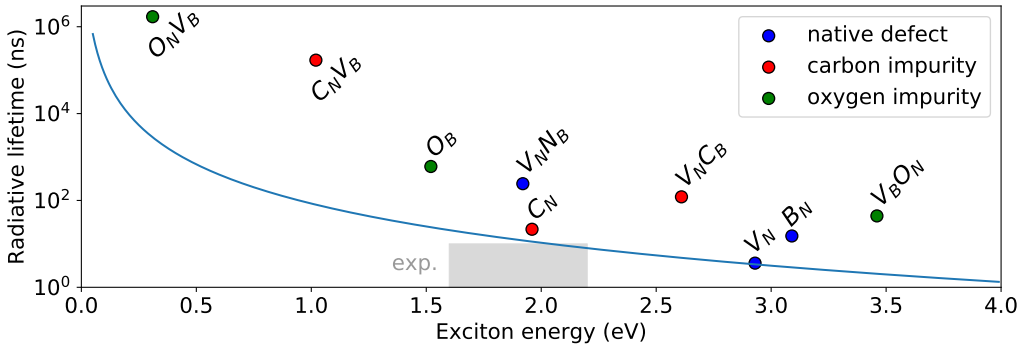

Figure 2.7: **Exciton radiative lifetime of selected defects in 2D h-BN.** Radiative lifetime and energy of the lowest bright exciton of candidate defect SPEs in hBN from GW-BSE calculations. The range of experimental values is shown as a shaded region. The blue line shows the radiative lifetime of an exciton with an assumed transition dipole moment of 6.9 Debye.

type	defect	polarized or not	energy (DFT, eV)	energy (GW-BSE, eV)	radiative lifetime (ns)
native defect	V_N	N	2.05	2.93	3.6
	B_N	N	2.20	3.09	15
	V_NN_B	Y	2.04	1.92	334
carbon impurity	C_N	N	1.25	1.96	21.7
	C_NV_B	Y	1.15	1.02	1.7×10^5
	V_NC_B	Y	1.93	2.61	121
oxygen impurity	O_B	Y	1.51	1.52	605
	O_NV_B	Y	0.72	0.31	1.7×10^6
	V_NO_B	Y	3.02	3.46	44
experiments		Y	1.6-2.2		2-10

Table 2.2: **Exciton properties in selected 2D h-BN defects.**

energy (1.6–2.2 eV) and radiative lifetime (1–10 ns) are also given for comparison in Fig. 2.7. Writing the exciton transition dipole in Eq. (2.29) as $\mathbf{p}_S = -(imE_S/\hbar e)\times e\,\mathbf{r}_S$ to highlight its physical meaning of an atomic-scale dipole, and setting $|\mathbf{r}_S| = |\langle 0|\mathbf{r}|S\rangle|$ equal to the in-plane B-N bond length (this choice gives a dipole of 6.9 Debye), the resulting radiative lifetime as a function of exciton energy gives a lower bound to the calculated radiative lifetimes (see the blue line in Fig. 2.7). The physical insight of this analysis is that due to incomplete overlap of the electron and hole

wavefunctions, the exciton transition dipole for most defects is significantly smaller than the bond length, leading to longer radiative lifetimes than this theoretical bound.

The main finding from the data in Table 2.2 is that the V_NN_B defect, which was originally proposed as a SPE in hBN on the basis of DFT calculations [154, 164, 169], possesses optical and radiative properties that most accurately match the experimental results, even after taking into account excitonic effects and radiative lifetimes. The next most likely structure is the oxygen impurity defect, O_B, with an emission energy of 1.52 eV just below the experimental range. On the other hand, we find that the V_NC_B defect, which is also considered a likely candidate in the literature based on DFT calculations [164, 169], has an emission energy of 2.6 eV that lies too far above the experimental energy range when excitonic effects are included, making it a less likely candidate. We note that although our analysis excludes the V_NC_B defect and other defects with higher emission energies as candidates for the 1.6−2.2 eV SPEs, they could still be good candidates for SPEs in the ultraviolet range [181, 182], which is not the focus of our discussion.

As the candidate defect structures have properties distributed across a wide range, it is challenging to pinpoint the correct defect structure from *ab initio* data only. As a result, members of our group provide a quantitative analysis of the relative likelihood of the various structures using Bayesian inference, a statistical approach for dealing with uncertainties and combining information from different categories, in which the probability of a hypothesis is updated as more evidence or information becomes available [183, 184]. The analysis arrived at the conclusion of V_NC_B being the most probable candidate defect structure which is in agreement with common believe [154, 164, 169], while a further study on the fine structure of V_NC_B attributes the large discrepancy between calculated radiative lifetime and experimental observation (334 ns and 10 ns) to its sensitive dependence on the out-of-plane N atom displacement as well as nonradiative process which can lower the quantum yield and render the time scale by an order of magnitude [184].

2.5 Exciton Recombination and Dissociation in 3D Wurtzite GaN

Gallium nitride (GaN) is widely employed for efficient light emission [185] and has been investigated extensively in crystalline, thin film, and heterostructure forms, both to understand its physical properties and to improve LED devices. Even though the exciton binding energy is rather weak in GaN (of order 20 meV [186]), accurately computing its absorption spectrum requires taking into account excitonic

effects [187], so one expects that excitons also play a role in light emission.

The radiative properties of GaN have remained the subject of debate [67, 105, 186, 188–190]. Investigations of radiative processes require PL spectroscopies or device experiments on pure samples. Since GaN films are typically grown epitaxially, and their doping is nontrivial, these measurements are affected by sample purity and competing non-radiative processes due to defects and interfaces [98]. In addition, typical theoretical treatments of radiative lifetimes employ simplified empirical methods that can only qualitatively interpret, or just fit, experimental data [91]. Accurate first-principles calculations of the *intrinsic* radiative properties of a GaN crystal would be highly desirable as they would serve as a benchmark for interpreting PL measurements and for guiding microscopic understanding and device design. Isolated examples of *ab initio* radiative lifetime calculations in bulk materials exist [94, 191], but they neglect key factors such as excitonic effects, the material anisotropy, and temperature dependence dictated by dimensionality.

In this section, we generalize the exciton radiative lifetime formula in isotropic 3D material, Eq. (2.13), to a uniaxial bulk crystal, and apply it to wurtzite GaN. The computed radiative lifetimes are in very good agreement (within a factor of two) with experiment up to 100 K, and we include thermal exciton dissociation to retain quantitative accuracy up to room temperature. In spite of the weak exciton binding energy in GaN, we show that including excitons is essential for quantitative accuracy as it improves substantially the agreement with experiment compared to the result obtained within the independent-particle picture (IPP). We also show that including spin-orbit coupling (SOC) and the related exciton fine structure is important in spite of the weak SOC in GaN. Our work advances the study of light emission in III-nitrides and anisotropic light emitters.

Exciton Radiative Lifetimes in Uniaxial Bulk Crystal

In uniaxial bulk crystal, the dielectric tensor is isotropic in the basal hexagonal plane, and different along the principal crystal axis (the z direction) such that Eq. (2.5) becomes:

$$\boldsymbol{\epsilon}_r = \mathrm{diag}(\epsilon_{xy}, \epsilon_{xy}, \epsilon_z). \tag{2.31}$$

Therefore, for a given wavevector $\mathbf{q}$, the two polarizations in the photon propagation mode can also be categorized as "in-plane"(IP) and "out-of-plane"(OOP) like

Eq. (2.11) but now with a more general form. For IP:

$$\frac{\omega_{\mathrm{IP}}}{c} = \sqrt{\frac{q^2}{\epsilon_{xy}}}, \quad \mathbf{e}_{\mathrm{IP}} = \frac{1}{\sqrt{\epsilon_{xy}}}\left(\frac{q_y}{q_{xy}}, -\frac{q_y}{q_{xy}}, 0\right). \tag{2.32}$$

and for OOP:

$$\frac{\omega_{\mathrm{OOP}}}{c} = \sqrt{\frac{\epsilon_{xy} q_{xy}^2 + \epsilon_z q_z^2}{\epsilon_{xy}\epsilon_z}}$$

with

$$\mathbf{e}_{\mathrm{OOP}} = \left(\frac{q_x}{q_{xy}}\sqrt{\frac{1/\epsilon_{xy}}{\left(1+\frac{\epsilon_{xy}q_{xy}^2}{\epsilon_z q_z^2}\right)}}, \frac{q_y}{q_{xy}}\sqrt{\frac{1/\epsilon_{xy}}{\left(1+\frac{\epsilon_{xy}q_{xy}^2}{\epsilon_z q_z^2}\right)}}, -\sqrt{\frac{1/\epsilon_z}{\left(1+\frac{\epsilon_z q_z^2}{\epsilon_{xy}q_{xy}^2}\right)}}\right), \tag{2.33}$$

where c is the speed of light and $q_{xy}^2 = q_x^2 + q_y^2$. The exciton radiative recombination rate can be obtain by applying Eq. (2.32) and Eq. (2.33) in Eq. (2.10) and becomes

$$\begin{aligned}\gamma_S(\mathbf{Q}) = \frac{\pi e^2}{\epsilon_0 m^2 V}\Bigg[&\frac{\sqrt{\epsilon_{xy}}}{cQ}\left|\frac{1}{\sqrt{\epsilon_{xy}}}\frac{p_{Sx}Q_y - p_{Sy}Q_x}{Q_{xy}}\right|_{\mathrm{IP}}^2 \delta\left(E_S(Q) - \frac{\hbar c Q}{\sqrt{\epsilon_{xy}}}\right) \\ &+ \frac{\sqrt{\epsilon_{xy}\epsilon_z}}{c\sqrt{\epsilon_{xy}Q_{xy}^2 + \epsilon_z Q_z^2}} \times \left|\frac{Q_x p_{Sx} + Q_y p_{Sy}}{Q_{xy}}\sqrt{\frac{1/\epsilon_{xy}}{1+\frac{\epsilon_{xy}Q_{xy}^2}{\epsilon_z Q_z^2}}} - p_{Sz}\sqrt{\frac{1/\epsilon_z}{1+\frac{\epsilon_z Q_z^2}{\epsilon_{xy}Q_{xy}^2}}}\right|_{\mathrm{OOP}}^2 \\ &\times\delta\left(E_S(Q) - \frac{\hbar c\sqrt{\epsilon_{xy}Q_{xy}^2 + \epsilon_z Q_z^2}}{\sqrt{\epsilon_{xy}\epsilon_z}}\right)\Bigg].\end{aligned} \tag{2.34}$$

To compute the effective lifetime at finite temperature T, we again assume the excitons to follow the thermal equilibrium distribution and apply the thermal average Eq. (2.2). In uniaxial material, the effective mass becomes anisotropic and has different IP and OOP components, M_{xy} and M_z, such that the exciton dispersion takes the form:

$$E_S(\mathbf{Q}) = E_S(0) + \frac{\hbar^2 Q_{xy}^2}{2M_{xy}} + \frac{\hbar^2 Q_z^2}{2M_z}, \tag{2.35}$$

where since BSE shows the lowest exciton states are composed of transitions from the two heavy-hole bands, we approximate the hole mass as the average of the two heavy-hole masses to compute M_{xy} and M_z. Applying Eq. (2.35) in Eq. (2.2), we can obtain the exciton effective recombination rate in axial symmetric materials:

$$\langle\gamma_S\rangle(T) = \left(\frac{E_S(0)^2}{2M_{xy}^{\frac{2}{3}}M_z^{\frac{1}{3}}c^2 k_B T}\right)^{3/2} \times \frac{\sqrt{\pi\epsilon_{xy}}e^2\hbar\left[\left(\frac{2\epsilon_z}{3\epsilon_{xy}}+2\right)\left(p_{Sx}^2 + p_{Sy}^2\right) + \frac{8}{3}p_{Sz}^2\right]}{\epsilon_0 m^2 V E_S(0)^2}, \tag{2.36}$$

where the exciton energies and transition dipoles are obtained by solving the BSE. The radiative lifetime is defined as the inverse radiative rate, $\langle \tau_S \rangle = \langle \gamma_S \rangle^{-1}$. Note also that Eq. (2.36) reduces to the bulk isotropic case in Eq. (2.13) if one put $\epsilon_{xy} = \epsilon_z$ and $M_{xy} = M_z$.

Finally, we take into account the fact that multiple exciton states can be occupied (including dark states with small transition dipoles, as is the case in GaN), and compute the radiative rate assuming a thermal equilibrium distribution:

$$\langle \gamma(T) \rangle = \frac{\sum_S \langle \gamma_S \rangle \, e^{-E_S(0)/k_B T}}{\sum_S e^{-E_S(0)/k_B T}}. \tag{2.37}$$

In the following, we use this thermal average formula, computed with the exciton radiative rates $\langle \gamma_S \rangle$ in Eq. (2.36), to study the *intrinsic* radiative lifetime $\langle \gamma(T) \rangle^{-1}$ in bulk wurtzite GaN.

Exciton Radiative Lifetime in GaN and Exciton Dissociation

We carry out first-principles calculations on a wurtzite GaN unit cell with relaxed lattice parameters. The ground state properties and electronic wave functions are computed using density functional theory (DFT) within the generalized gradient approximation [74, 120] with the Quantum ESPRESSO code [80]. Fully-relativistic norm-conserving pseudopotentials [192] generated with Pseudo Dojo [75] are employed, in which the shells treated as valence are the 3s, 3p, 3d, 4s, and 4p for Ga and the 2s and 2p for N. A non-linear core correction [193] is included for all remaining core shells for both atoms. We compute the quasiparticle band structure in GaN [194] with a "one-shot" GW calculation [71] with the Yambo code [86] using a plasmon-pole model for the dielectric function, a 25 Ry cutoff for the dielectric matrix, 300 empty bands, and a $14 \times 14 \times 10$ k-point grid. For the GW band structure, we start from DFT within the local-density approximation [73] and employ scalar-relativistic norm-conserving pseudopotentials for both Ga and N, where the 4s and 4p shells are treated as valence for Ga, and the 2s and 2p for N. A non-linear core correction is included to account for the 3d core states in Ga. The BSE is solved on a $24 \times 24 \times 18$ k-point grid using a 6 Ry cutoff for the static dielectric screening and the 6 highest valence bands and 4 lowest conduction bands. These settings are sufficient to converge the energies, transition dipoles and radiative lifetimes of the low-energy excitons, as we have verified. The IPP transition dipoles and energies are computed by neglecting the electron-hole interactions in the BSE. The exciton binding energy is converged by computing it with several k-point grids

from $12 \times 12 \times 9$ to $24 \times 24 \times 18$ and extrapolating it to a vanishingly small k-point distance (i.e., to an infinitely dense grid) [195] .

Our computed radiative lifetimes between 50-150 K are shown in Fig. 2.8a) along with experimental values from Ref. [105], which are ideal for our comparison since they were measured in a relatively pure GaN crystal. At low temperatures up to 100 K, our first-principles radiative lifetimes, with SOC included, are of order 200-900 ps and are in very good agreement (within less than a factor of two) with experiment. We attribute the remaining discrepancy to small uncertainties in the computed exciton effective mass, transition dipoles, energies and occupations, plus inherent uncertainties in the experimental data. Both the computed and experimental lifetimes exhibit the intrinsic $T^{3/2}$ trend predicted by our approach [see Eq. (2.37)]. As Fig. 2.8a) shows, when neglecting excitons and using IPP transition dipoles and energies, one greatly overestimates the radiative lifetime. The IPP lifetimes are greater by nearly an order of magnitude compared to our treatment, which correctly includes excitons, and by over a factor of three compared to experiment.

As seen in Fig. 2.8a), including SOC when computing the exciton states increases the radiative lifetimes by a factor of 2-3 and significantly improves the agreement with experiment. Though SOC is weak in GaN — the valence band splitting at γ is only 5 meV in our calculations — its inclusion is crucial for obtaining accurate exciton states. Fig. 2.8b) shows the individual radiative lifetimes $\langle \gamma_S \rangle^{-1}$and relative energies of the low-energy excitons contributing to the thermal average in Eq. (2.37), for both the cases where SOC is included and neglected. Without including spin and SOC, the exciton structure consists of three bright singlet excitons, two of which are degenerate. The lifetimes of all three excitons are nearly identical, and their value determines the radiative lifetime for the calculation without SOC. Including the SOC lifts the degeneracy of the two lowest bright excitons by ~5 meV, and resolves the exciton fine structure, splitting each exciton into four states due to a doubling of the number of valence and conduction states that compose the electron-hole transitions. With SOC, we find dark excitons with lifetimes roughly 3-10 orders of magnitude longer than the excitons found without SOC. When included in the thermal average, these dark states are crucial as they increase the radiative lifetime compared to the average lifetime of the bright excitons alone. The inclusion of SOC and the exciton fine structure are thus important for quantitative accuracy, even though SOC per se is weak in GaN. Note that spin is always important. Even in the limit of vanishingly small SOC, the triplet states with ideally infinite lifetime would still suppress the

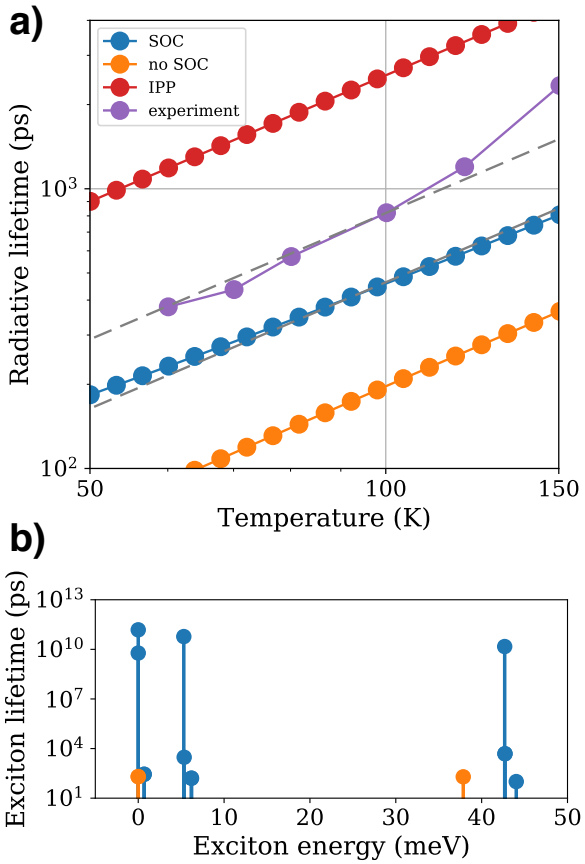

Figure 2.8: **Exciton intrinsic lifetimes.** a) Comparison of our radiative lifetimes computed by including (blue) or neglecting (orange) the SOC in the solution of the BSE, or obtained in the IPP by neglecting excitons (red). Experimental results from Ref. [105] (purple) are shown for comparison. The gray dashed lines show the $T^{3/2}$ trend predicted by our treatment at low temperature. b) The excitons contributing to the thermal average in Eq. (2.37), along with their individual lifetimes at 100 K, computed with (blue) and without (orange) SOC. The zero of the energy axis is taken to be the lowest exciton energy for each case.

average radiative rate in Eq. (2.37) by a factor of 4, and thus increase the radiative lifetimes by the same factor compared to a calculation that does not include spin.

Due to the small exciton binding energy in GaN, at high enough temperatures the excitons dissociate into free electrons and holes, which mainly recombine non-radiatively in GaN, giving rise to the lower radiative recombination rate and quantum yield seen experimentally above 100 K [105, 196]. As a result of exciton dissociation, the measured radiative lifetime above ~100 K increases more rapidly with temperature than the intrinsic $T^{3/2}$ trend [see Fig. 2.8a)]. Here We adopt a simple model to include exciton dissociation in our first-principles approach. Assuming

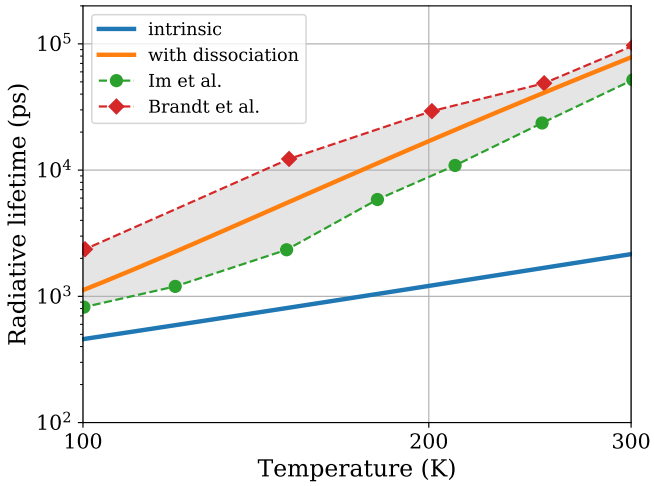

Figure 2.9: **Exciton effect lifetimes with eciton dissociation effect.** Comparison of our computed radiative lifetimes including exciton dissociation (orange) above 100 K with experimental data from Refs. [105] and [190]. Also shown is our computed intrinsic radiative lifetime (blue).

that excitons and free carriers are in thermal equilibrium, we write the mass-action law for their concentrations as [196]

$$\frac{n_e n_h}{n_{\text{exc}}} = \frac{[n_0 + \delta n]\delta p}{\delta n_{\text{exc}}} = \kappa(T), \tag{2.38}$$

where n_e, n_h, and n_{exc} are the electron, hole, and exciton densities, respectively, n_0 is the background electron density (from the doping), and δn, δp, and δn_{exc} are the excited electron, hole, and exciton densities, respectively, generated by an idealized optical pump or electrical current.The equilibrium constant $\kappa(T)$ is given by [196]

$$\kappa(T) = 2\left(\frac{m_{\text{red}} k_B T}{2\pi\hbar^2}\right)^{3/2} e^{-E_b/k_B T}, \tag{2.39}$$

where $m_{\text{red}} = m_h m_e/(m_h + m_e)$ is the reduced mass of the exciton and E_b its binding energy. We find a converged binding energy of 19.7 meV, in excellent agreement with the experimental value of 20.4 meV [186], and we use a typical doping of $n_0 = 2.5 \times 10^{-16}$ cm^{-3}, taken from Ref. [105].

Assuming that the relative recombination probability of free carriers and excitons is proportional to their concentration ratio, $P_{\text{carr}}/P_{\text{exc}} = \delta n/\delta n_{\text{exc}}$, and using $P_{\text{carr}} + P_{\text{exc}} = 1$, we can obtain the probabilities for exciton and free carrier recombination. The measured radiative rate will be a weighted average of the rates of the two recombination processes, $\Gamma_{\text{rad}} = \Gamma_{\text{carr}} P_{\text{carr}} + \Gamma_{\text{exc}} P_{\text{exc}}$. We assume that Γ_{carr} vanishes because free carriers recombine mainly via non-radiative channels,

such as defect trapping, which is justified by the reported low quantum yield seen experimentally near room temperature [105]. The measured radiative rate due to excitons in equilibrium with carriers becomes $\Gamma_{\text{rad}} \approx \Gamma_{\text{exc}}/(1+\kappa(T)/n_0)$. Using this result, together with our computed effective masses and converged exciton binding energy, we are able to predict the exciton radiative lifetimes also above 100 K.

Fig. 2.9 compares the computed radiative lifetimes up to 300 K with experimental results taken from PL measurements in Refs. [105, 190]. When thermal dissociation is included, the radiative lifetime agrees with experiment even in the 100–300 K temperature range, where the experimental data deviate from the intrinsic $T^{3/2}$ trend. Our ability to compute intrinsic exciton radiative lifetimes allows us to conclude that the radiative lifetime increase seen experimentally above 100 K is due to exciton thermal dissociation into free carriers. This conclusion is consistent with the results by Im et al. [105], who found that a similar exciton dissociation model could fit their experimental data at high temperature.

2.6 Conclusion

A unified approach based on DFT and the *ab initio* BSE method is presented to compute the radiative lifetimes in bulk crystals, 2D and 1D materials, and in 0D or isolated systems such as a molecule, quantum dot or single quantum emitter. Diagonalizing the BSE Hamiltonian in transition space is computationally expensive; since the size of the transition space scales quadratically with the number of atoms N, a straightforward diagonalization of the BSE Hamiltonian will scale as N^6. Nevertheless, once its eigenvalues and eigenvectors are obtained, the radiative lifetimes calculations shown here only add a small computational overhead. The temperature dependence of the exciton radiative lifetime at low temperature is predicted to be proportional to $T^{3/2}$ in bulk, T in 2D and $T^{1/2}$ in 1D materials. Our result provides a framework for predicting the *intrinsic* exciton radiative lifetimes in materials with any dimensionality. Since the BSE is considered a gold standard for computing optical absorption and excitons [197], it is expected to also provide accurate results for radiative processes and light emission.

Two benchmark calculations are demonstrated to support our method. The bulk crystal treatment is applied to a GaAs crystal, where our computed intrinsic radiative lifetimes are shorter than the values measured by photoluminescence, but consistent with their interpretation in terms of nonequilibrium dynamics of excitons coupled to phonons and free carriers. Computation for isolated emitters is applied to small

organic molecules in the gas phase, giving computed radiative lifetimes in good agreement with experiment, up to corrections due to structural relaxation in the excited state.

Three studies are carried out based on the developed formalism. We first reformulate the exciton radiative lifetime formula in 2D system to study the exciton PL. We point out the correlation between PL polarization and the valley coherence which can be revealed from the anisotropy in PL strength. The results shed light on the microscopic understanding in the underlying mechanism for TMD anisotropic light emission and provide a alternative direction for designs in valleytronics. Second, we investigate the excited state and radiative properties of many candidate defect SPEs in monolayer h-BN. Our calculations address the photophysics of these defect structures, including their optical transitions and radiative lifetimes, using calculations that accurately account for excitonic effects and anisotropic dielectric screening. Among the potential atomic structures, we identify the V_NN_B defect as the most likely candidate. This finding can greatly benefit the search on novel single emitters in future quantum technologies and lays out new insights in optoelectronic device. Last, we develop accurate first-principles radiative lifetime calculations in GaN, with both the electron-hole and spin-orbit interactions included. For excitonic effect in general neglected in perivous studies, applying BSE scheme allows us to compute intrinsic radiative lifetimes in very good agreement with experiment, and gain microscopic insight into the excitons associated with light emission in GaN. Further work can apply this analysis to nitride heterostructures and other solid state emitters such as InGaN.

For general applications and future extensions, calculations of this kind can provide a standard for materials in which intrinsic excitonic quantities are hard to access due to stonrg extrinsic effects from impurities and the ultrafast dynamics . They can also guide the interpretation of ultrafast spectroscopy measurements and the discovery of new quantum emitters with long radiative lifetimes in the form of quantum well, heterostructures, and semiconducting crystals.

Chapter 3

EXCITON-PHONON INTERACTION AND ULTRAFAST DYNAMICS

This chapter contains the publication:

[1] H.-Y. Chen, D. Sangalli, and M. Bernardi, "Exciton-phonon interaction and relaxation times from first principles", Phys. Rev. Lett. **125**, 107401 (2020). DOI: 10.1103/PhysRevLett.125.107401.

[2] H.-Y. Chen, D. Sangalli, and M. Bernardi, "Real-time exciton dynamics and time-domain ARPES simulations using first-principles exciton-phonon interactions", In Preparation., (2021),

[3] S. Dong, H.-Y. Chen, D. Sangalli, M. Bernardi, and R. Ernstorfer, "Resolving exciton dynamics in monolayer WSe_2 via time-resolved ARPES: pump and probe measurement and real-time ab initio simulation", In Preparation., (2021),

Exciton dynamics is probed with ultrafast optical or device measurements [198–200]; theories that can shed light on microscopic exciton processes and assist experiment interpretation are highly sought after. However, while first-principles methods to predict exciton binding energies, optical transitions [71, 85] and radiative lifetimes[1] are well established, accurate calculations of exciton dynamics and non-radiative processes are a research frontier.

The interaction between electrons and lattice vibrations (phonons) controls the dynamics of carriers and excitons. Recent advances have made *ab initio* calculations of electron-phonon (e-ph) interactions and scattering processes widespread [62], enabling studies of charge transport [201–203] and nonequilibrium carrier dynamics [67, 204] in materials. These methods achieve quantitative accuracy and can provide unprecedented microscopic insight into electron dynamics. In the typical workflow [62], one uses DFT to compute the electronic band structure and DFPT [61] to compute phonon dispersions, as well as the perturbation potential due to phonons. These quantities are combined to obtain the e-ph matrix elements[2] [62, 205],

$$g_{mn\nu}(\mathbf{k}, \mathbf{q}) = \langle m\mathbf{k} + \mathbf{q} | \Delta V_{\nu\mathbf{q}} | n\mathbf{k} \rangle, \tag{3.1}$$

[1] See chapter 2 and corresponding references.
[2] See Sect. 1.2 for detailed introduction.

which represent the probability amplitude for scattering from an initial Bloch state $|n\mathbf{k}\rangle$ to a final state $|m\mathbf{k}+\mathbf{q}\rangle$, by emitting or absorbing a phonon with mode index ν and wave vector $\mathbf{q}$, due to the perturbation of the Kohn-Sham potential, $\Delta V_{\nu\mathbf{q}}$, induced by the phonon [62].

Excitons pose new challenges to this framework, since one can no longer study independently the scattering of electrons or holes with phonons when the two carriers are bound together. Rather, the challenge is to address exciton-phonon (ex-ph) interactions, which govern, from low to high temperatures, photoluminescence linewidths, exciton diffusion, and ultrafast dynamics in broad families of materials with strongly bound excitons [18, 23, 147, 206–213]. Several analytical or semi-empirical models have been proposed for ex-ph interactions [9, 214–220]; recent work has put forward a many-body approach but did not present numerical results [221]. To date, rigorous *ab initio* calculations of ex-ph interactions and dynamical processes are still missing.

Here we provide a theoretical derivation within lowest-order perturbation theory and build up an algorithm to carry out ex-ph coupling matrix elements and corresponding physical phenomena from first principles. We apply the formalism to study the exciton dynamics in bulk h-BN and monolayer WSe_2. Our results show that the ex-ph interaction can be viewed as a quantum superposition of electron and hole scattering events with phonons, weighted by the exciton wave function in the transition basis. Our calculations in h-BN show a dominant coupling between excitons and longitudinal optical (LO) phonons. We find ex-ph relaxation times of order $5-100$ fs at 77 K; the relaxation times drop rapidly above the LO phonon emission threshold and become nearly temperature independent, while below the emission threshold they increase linearly with temperature. The dominant ex-ph coupling with optical phonon is also realized in the PL spectrum where two prominent optical phonon emission line are found in both experiment observation and our numerical results. In WSe_2, we investigate the homogeneous bright exciton linewidth and found a $\sim$20 meV increasing from 1 K to room temperature in agreement with experiment data. In addition, our analysis of the PL identifies the prevailing peak from longitudinal acoustic phonon emission and the lower energy sideband is attributed to the optical phonon emission. Last, we demonstrate a joint collaboration on exciton real time dynamics study in WSe_2. Our simulation correctly predicts the exciton relaxation time scale of $\sim$50 fs. The analysis in the exciton scattering process reveals the relaxation path ways. We also provide prediction of the time-resolved ARPES which

opens a new direction for future experimental research in 2D-TMDs. Our study provides microscopic insight into exciton thermal and dynamical processes while the method is general and ready to be applied in all exciton-hosting materials.

3.1 Theory and Numerical Method

To study the ex-ph interaction, we apply the first-order perturbation theory by introducing deformation potential from atomic displacements, while the ex-ph coupling constant will be derived as the matrix element. The derivation for e-ph interaction based on the same method can be found in Appendix G. A system with static atomic displacements $\{\mathbf{u}_{is}\}$ from the equilibrium positions provides a perturbed Kohn-Sham potential, given by a Taylor expansion about the equilibrium positions (See Eq. (1.12)):

$$V^{KS}(\{\mathbf{u}_{is}\}) = V_0^{KS} + \sum_{is\alpha} \frac{\partial V^{KS}}{\partial \mathbf{u}_{is\alpha}} \mathbf{u}_{is\alpha} + O(\{\mathbf{u}_{is}\}^2), \tag{3.2}$$

where i labels the unit cell, s the atom, and V_0^{KS} is the unperturbed Kohn-Sham potential, for which all $\mathbf{u}_{is} = 0$. The electronic wave functions and eigenvalues of the perturbed system depend on the atomic displacements $\{\mathbf{u}_{is}\}$. To obtain their change in the perturbed system, we apply first-order perturbation theory by keeping terms linear in $\{\mathbf{u}_{is}\}$. To first-order, the correction to the eigenvalues vanishes, while the correction to the wave functions ϕ_i can be written as:

$$\delta|\phi_i\rangle = \sum_{j\neq i} \frac{\langle\phi_j|\Delta V|\phi_i\rangle}{\epsilon_i - \epsilon_j}|\phi_j\rangle, \qquad \text{with} \quad \Delta V = \sum_{is\alpha} \frac{\partial V^{KS}}{\partial \mathbf{u}_{is}} \cdot \mathbf{u}_{is}, \tag{3.3}$$

where$|\phi_i\rangle$ are the unperturbed Kohn-Sham wave functions satisfying:

$$\left(\frac{-\hbar^2\nabla^2}{2m} + V_0^{KS}\right)|\phi_i\rangle = \epsilon_i|\phi_i\rangle. \tag{3.4}$$

In the following, we use the tilde for physical quantities of the perturbed system, and write the perturbed wave function as:

$$|\tilde{\phi}_i\rangle = |\phi_i\rangle + \delta|\phi_i\rangle = |\phi_i\rangle + \sum_{j\neq i} \Delta_{ij}|\phi_j\rangle \tag{3.5}$$

with

$$\Delta_{ij} \equiv \frac{\langle\phi_j|\Delta V|\phi_i\rangle}{\epsilon_i - \epsilon_j}. \tag{3.6}$$

With the change in the potential and wave function, we can define the unperturbed BSE Hamiltonian $H \equiv H(\{\mathbf{u}_{is}\} = 0)$ and the perturbed BSE Hamiltonian $\tilde{H} \equiv$

$H(\{\mathbf{u}_{is}\})$. The unperturbed BSE Hamiltonian is solvable and gives the exciton energies and wave functions by Eq. (1.9). On the other hand, the perturbed BSE Hamiltonian is not solved directly, but to first order it provides the ex-ph interactions. Using the known form of the BSE Hamiltonian, we write:

$$H_{vc,v'c'} = \langle vc|H|v'c'\rangle = (\epsilon_c - \epsilon_v)\,\delta_{vv'}\delta_{cc'} + K_{vc,v'c'} \tag{3.7}$$

and

$$\tilde{H}_{\tilde{v}\tilde{c},\tilde{v}'\tilde{c}'} = \langle \tilde{v}\tilde{c}|\tilde{H}|\tilde{v}'\tilde{c}'\rangle = (\tilde{\epsilon}_{\tilde{c}} - \tilde{\epsilon}_{\tilde{v}})\,\delta_{\tilde{v}\tilde{v}'}\delta_{\tilde{c}\tilde{c}'} + \tilde{K}_{\tilde{v}\tilde{c},\tilde{v}'\tilde{c}'}. \tag{3.8}$$

Here, $K_{vc,v'c'}$ is the BSE kernel, defined as:

$$K_{vc,v'c'} = \langle vc|K|v'c'\rangle = \int d\mathbf{x}_1 d\mathbf{x}_2 d\mathbf{x}_3 d\mathbf{x}_4\, \psi_v(\mathbf{x}_2)\psi_c^*(\mathbf{x}_1)K(\mathbf{x}_1\mathbf{x}_2\mathbf{x}_3\mathbf{x}_4)\psi_{v'}^*(\mathbf{x}_3)\psi_{c'}(\mathbf{x}_4), \tag{3.9}$$

where

$$K(\mathbf{x}_1\mathbf{x}_2\mathbf{x}_3\mathbf{x}_4) = -i\delta(\mathbf{x}_1,\mathbf{x}_2)\delta(\mathbf{x}_3,\mathbf{x}_4)v(\mathbf{x}_1,\mathbf{x}_4) + i\delta(\mathbf{x}_1,\mathbf{x}_4)\delta(\mathbf{x}_2,\mathbf{x}_3)W(\mathbf{x}_1,\mathbf{x}_2) \tag{3.10}$$

includes the bare Coulomb potential v and the screened Coulomb interaction W. In addition, $\tilde{K}_{\tilde{v}\tilde{c},\tilde{v}'\tilde{c}'}$ is the corresponding BSE kernel in the perturbed system with the phonon displacement frozen in:

$$\tilde{K}_{\tilde{v}\tilde{c},\tilde{v}'\tilde{c}'} = \langle \tilde{v}\tilde{c}|\tilde{K}|\tilde{v}'\tilde{c}'\rangle = \int d\mathbf{x}_1 d\mathbf{x}_2 d\mathbf{x}_3 d\mathbf{x}_4\, \tilde{\psi}_{\tilde{v}}(\mathbf{x}_2)\tilde{\psi}_{\tilde{c}}^*(\mathbf{x}_1)\tilde{K}(\mathbf{x}_1\mathbf{x}_2\mathbf{x}_3\mathbf{x}_4)\tilde{\psi}_{\tilde{v}'}^*(\mathbf{x}_3)\tilde{\psi}_{\tilde{c}'}(\mathbf{x}_4), \tag{3.11}$$

where

$$\tilde{K}(\mathbf{x}_1\mathbf{x}_2\mathbf{x}_3\mathbf{x}_4) = -i\delta(\mathbf{x}_1,\mathbf{x}_2)\delta(\mathbf{x}_3,\mathbf{x}_4)v(\mathbf{x}_1,\mathbf{x}_4) + i\delta(\mathbf{x}_1,\mathbf{x}_4)\delta(\mathbf{x}_2,\mathbf{x}_3)\tilde{W}(\mathbf{x}_1,\mathbf{x}_2). \tag{3.12}$$

Solving the BSE Hamiltonian in Eq. (3.7) gives the exciton wave functions $|S_n\rangle$ and energies E^{S_n}:

$$\sum_{v'c'} H_{vc,v'c'}A^{S_n}_{v'c'} = E^{S_n}A^{S_n}_{vc} \quad \text{with the exciton wave function} \quad |S_n\rangle = \sum_{vc} A^{S_n}_{vc}|vc\rangle. \tag{3.13}$$

While we do not solve Eq. (3.8) directly, we project the perturbed BSE Hamiltonian onto the unperturbed basis set and keep terms of first-order in the phonon perturbation; by comparing the result with the unperturbed BSE Hamiltonian in Eq. (3.7), the additional terms will define the ex-ph interaction. Also, since as mentioned above the correction to the electron energies is of second order, we will use $\tilde{\epsilon}_i = \epsilon_i$.

We first write the perturbed BSE Hamiltonian in the unperturbed exciton basis:

$$\begin{aligned}\tilde{H}_{mn} = \langle S_m|\tilde{H}|S_n\rangle &= \sum_{\tilde{v}\tilde{c},\tilde{v}'\tilde{c}'} \langle S_m|\tilde{v}\tilde{c}\rangle\langle\tilde{v}\tilde{c}|\tilde{H}|\tilde{v}'\tilde{c}'\rangle\langle\tilde{v}'\tilde{c}'|S_n\rangle \\ &= \sum_{vc,v'c'}\sum_{\tilde{v}\tilde{c},\tilde{v}'\tilde{c}'} \langle S_m|vc\rangle\langle vc|\tilde{v}\tilde{c}\rangle\langle\tilde{v}\tilde{c}|\tilde{H}|\tilde{v}'\tilde{c}'\rangle\langle\tilde{v}'\tilde{c}'|v'c'\rangle\langle v'c'|S_n\rangle, \quad (3.14)\end{aligned}$$

where we inserted the complete unperturbed and perturbed basis sets, $\sum_{vc}|vc\rangle\langle vc| = 1$ and $\sum_{\tilde{v},\tilde{c}}|\tilde{v}\tilde{c}\rangle\langle\tilde{v}\tilde{c}| = 1$, respectively. Using the BSE wave function $\langle v'c'|S_n\rangle = A^{S_n}_{v'c'}$, we write Eq. (3.14) as

$$\tilde{H}_{mn} = \langle S_m|\tilde{H}|S_n\rangle = \sum_{vc,v'c'} A^{S_m*}_{vc} A^{S_n}_{v'c'} \times \left[\sum_{\tilde{v}\tilde{c},\tilde{v}'\tilde{c}'} \langle vc|\tilde{v}\tilde{c}\rangle\langle\tilde{v}\tilde{c}|\tilde{H}|\tilde{v}'\tilde{c}'\rangle\langle\tilde{v}'\tilde{c}'|v'c'\rangle\right]. \quad (3.15)$$

We focus on the term in brackets and separate it into two parts:

$$\begin{aligned}&\sum_{\tilde{v}\tilde{c},\tilde{v}'\tilde{c}'} \langle vc|\tilde{v}\tilde{c}\rangle\langle\tilde{v}\tilde{c}|\tilde{H}|\tilde{v}'\tilde{c}'\rangle\langle\tilde{v}'\tilde{c}'|v'c'\rangle \\ &= \sum_{\tilde{v}\tilde{c},\tilde{v}'\tilde{c}'} \langle vc|\tilde{v}\tilde{c}\rangle \left[(\tilde{\epsilon}_{\tilde{c}} - \tilde{\epsilon}_{\tilde{v}})\,\delta_{\tilde{v}\tilde{v}'}\delta_{\tilde{c}\tilde{c}'} + \tilde{K}_{\tilde{v}\tilde{c},\tilde{v}'\tilde{c}'}\right]\langle\tilde{v}'\tilde{c}'|v'c'\rangle \\ &= \sum_{\tilde{v}\tilde{c}}\langle vc|\tilde{v}\tilde{c}\rangle\,(\epsilon_{\tilde{c}} - \epsilon_{\tilde{v}})\,\langle\tilde{v}\tilde{c}|v'c'\rangle + \sum_{\tilde{v}\tilde{c},\tilde{v}'\tilde{c}'}\langle vc|\tilde{v}\tilde{c}\rangle\tilde{K}_{\tilde{v}\tilde{c},\tilde{v}'\tilde{c}'}\langle\tilde{v}'\tilde{c}'|v'c'\rangle. \quad (3.16)\end{aligned}$$

Since the effect of the atomic displacements on the bare and screened Coulomb interactions can be ignored to first order, analogous to the GW approximation, $\tilde{W} \approx W$ [85, 222], we can approximate the perturbed kernel with the unperturbed one, $\tilde{K}_{\tilde{v}\tilde{c},\tilde{v}'\tilde{c}'} \approx \langle\tilde{v}\tilde{c}|K|\tilde{v}'\tilde{c}'\rangle$. With this approximation, we have:

$$\begin{aligned}&\sum_{\tilde{v}\tilde{c},\tilde{v}'\tilde{c}'} \langle vc|\tilde{v}\tilde{c}\rangle\tilde{K}_{\tilde{v}\tilde{c},\tilde{v}'\tilde{c}'}\langle\tilde{v}'\tilde{c}'|v'c'\rangle \\ &\approx \sum_{\tilde{v}\tilde{c},\tilde{v}'\tilde{c}'} \langle vc|\tilde{v}\tilde{c}\rangle\langle\tilde{v}\tilde{c}|K|\tilde{v}'\tilde{c}'\rangle\langle\tilde{v}'\tilde{c}'|v'c'\rangle = \langle vc|K|v'c'\rangle = K_{vc,v'c'} \quad (3.17)\end{aligned}$$

and thus the term in brackets in Eq. (3.15) becomes

$$\sum_{\tilde{v}\tilde{c},\tilde{v}'\tilde{c}'} \langle vc|\tilde{v}\tilde{c}\rangle\langle\tilde{v}\tilde{c}|\tilde{H}|\tilde{v}'\tilde{c}'\rangle\langle\tilde{v}'\tilde{c}'|v'c'\rangle = \sum_{\tilde{v}\tilde{c}}\langle vc|\tilde{v}\tilde{c}\rangle\,(\epsilon_{\tilde{c}} - \epsilon_{\tilde{v}})\,\langle\tilde{v}\tilde{c}|v'c'\rangle + K_{vc,v'c'}. \quad (3.18)$$

Next, we use Eq. (3.5) to expand $\sum_{\tilde{v}\tilde{c}}\langle vc|\tilde{v}\tilde{c}\rangle\,(\epsilon_{\tilde{c}} - \epsilon_{\tilde{v}})\,\langle\tilde{v}\tilde{c}|v'c'\rangle$ to order $O(\Delta)$. We work within the Tamm-Dancoff approximation and keep only the resonant part of the BSE Hamiltonian; as a consequence, only valence-valence and conduction-conduction e-ph scattering will take place, namely, $\Delta_{vc} = \Delta_{cv} = 0$.

Using Eq. (3.5), we get:

$$\begin{aligned}\langle vc|\tilde{v}\tilde{c}\rangle = \langle v|\tilde{v}\rangle\langle c|\tilde{c}\rangle &= (\delta_{v\tilde{v}} + \sum_{v''\neq\tilde{v}} \Delta_{\tilde{v}v''}\delta_{vv''})(\delta_{c\tilde{c}} + \sum_{c''\neq\tilde{c}} \Delta_{\tilde{c}c''}\delta_{cc''}) \\ &= \left(\delta_{v\tilde{v}}\delta_{c\tilde{c}} + \delta_{v\tilde{v}}\sum_{c''\neq\tilde{c}} \Delta_{\tilde{c}c''}\delta_{cc''} + \delta_{c\tilde{c}}\sum_{v''\neq\tilde{v}} \Delta_{\tilde{v}v''}\delta_{vv''}\right) + O(\Delta^2) \qquad (3.19)\end{aligned}$$

and similarly

$$\begin{aligned}\langle \tilde{v}\tilde{c}|v'c'\rangle &= \langle v'|\tilde{v}\rangle^*\langle c'|\tilde{c}\rangle^* \\ &= \left(\delta_{v'\tilde{v}}\delta_{c'\tilde{c}} + \delta_{v'\tilde{v}}\sum_{c''\neq\tilde{c}} \Delta^*_{\tilde{c}c''}\delta_{c'c''} + \delta_{c'\tilde{c}}\sum_{v''\neq\tilde{v}} \Delta^*_{\tilde{v}v''}\delta_{v'v''}\right) + O(\Delta^2) \qquad (3.20)\end{aligned}$$

Using these results, we find five first-order terms in $\sum_{\tilde{v}\tilde{c}}\langle vc|\tilde{v}\tilde{c}\rangle\,(\epsilon_{\tilde{c}} - \epsilon_{\tilde{v}})\,\langle\tilde{v}\tilde{c}|v'c'\rangle$, which we simplify using the δ's:

$$\begin{aligned}&\sum_{\tilde{v}\tilde{c}}\langle vc|\tilde{v}\tilde{c}\rangle\,(\epsilon_{\tilde{c}} - \epsilon_{\tilde{v}})\,\langle\tilde{v}\tilde{c}|v'c'\rangle \\ &\quad\approx (\epsilon_c - \epsilon_v)\,\delta_{vv'}\delta_{cc'} + \delta_{cc'}\sum_{\tilde{v}}(\epsilon_c - \epsilon_{\tilde{v}})\sum_{v''\neq\tilde{v}}\left(\Delta^*_{\tilde{v}v''}\delta_{vv''}\delta_{v'\tilde{v}} + \Delta_{\tilde{v}v''}\delta_{v'v''}\delta_{v\tilde{v}}\right) \\ &\qquad\qquad + \delta_{vv'}\sum_{\tilde{c}}(\epsilon_{\tilde{c}} - \epsilon_v)\sum_{c''\neq\tilde{c}}\left(\Delta_{\tilde{c}c''}\delta_{cc''}\delta_{c'\tilde{c}} + \Delta^*_{\tilde{c}c''}\delta_{c'c''}\delta_{c\tilde{c}}\right) \\ &\quad= (\epsilon_c - \epsilon_v)\,\delta_{vv'}\delta_{cc'} + \delta_{cc'}\left[\sum_{v''\neq v'}(\epsilon_c - \epsilon_{v'})\,\Delta^*_{v'v''}\delta_{vv''} + \sum_{v''\neq v}(\epsilon_c - \epsilon_v)\,\Delta_{vv''}\delta_{v'v''}\right] \\ &\qquad\qquad + \delta_{vv'}\left[\sum_{c''\neq c'}(\epsilon_{c'} - \epsilon_v)\,\Delta_{c'c''}\delta_{cc''} + \sum_{c''\neq c}(\epsilon_c - \epsilon_v)\,\Delta^*_{cc''}\delta_{c'c''}\right] \\ &\quad= (\epsilon_c - \epsilon_v)\,\delta_{vv'}\delta_{cc'} + \delta_{cc'}\,(\epsilon_{v'} - \epsilon_v)\,\Delta_{vv'} + \delta_{vv'}\,(\epsilon_c - \epsilon_{c'})\,\Delta^*_{cc'}, \qquad (3.21)\end{aligned}$$

where we used $\Delta_{ij} = -\Delta^*_{ji}$ to obtain the last line. Finally, the perturbed Hamiltonian in the exciton basis in Eq. (3.15) becomes:

$$\begin{aligned}\tilde{H}_{mn} &= \sum_{vc,v'c'} A^{S_m*}_{vc}A^{S_n}_{v'c'} \times \Bigg\{\left[(\epsilon_c - \epsilon_v)\,\delta_{vv'}\delta_{cc'} + K_{vc,v'c'}\right] \\ &\qquad\qquad + \delta_{cc'}\,(\epsilon_{v'} - \epsilon_v)\,\Delta_{vv'} + \delta_{vv'}\,(\epsilon_c - \epsilon_{c'})\,\Delta^*_{cc'}\Bigg\} \\ &= E^{S_m}\delta_{mn} + \sum_{vc,v'c'} A^{S_m*}_{vc}A^{S_n}_{v'c'}\cdot\left(\delta_{cc'}\,(\epsilon_{v'} - \epsilon_v)\,\Delta_{vv'} + \delta_{vv'}\,(\epsilon_c - \epsilon_{c'})\,\Delta^*_{cc'}\right), \qquad (3.22)\end{aligned}$$

where we use the fact that the unperturbed Hamiltonian is diagonalized by the Tamm-Dancoff exciton eigenvectors:

$$E^{S_m}\delta_{mn} = \sum_{vc,v'c'} A^{S_m*}_{vc}A^{S_n}_{v'c'} \times \left((\epsilon_c - \epsilon_v)\,\delta_{vv'}\delta_{cc'} + K_{vc,v'c'}\right). \qquad (3.23)$$

Therefore, the first term in the second line of Eq. (3.22) is the unperturbed Hamiltonian, while the second term is the ex-ph interaction,

$$\tilde{H}_{\text{ex-ph}} = \sum_{vc,v'c'} A_{vc}^{S_m *} A_{v'c'}^{S_n} \cdot \left(\delta_{cc'} \left(\epsilon_{v'} - \epsilon_v \right) \Delta_{vv'} + \delta_{vv'} \left(\epsilon_c - \epsilon_{c'} \right) \Delta_{cc'}^* \right). \tag{3.24}$$

To obtain the final result, we relabel all quantities in the ex-ph Hamiltonian for a periodic system. The wave functions are Bloch states

$$|\phi_i\rangle \rightarrow |\phi_{n\mathbf{k}}\rangle,$$

and the transition basis set for an exciton with center of mass momentum $\mathbf{Q}$ is $|vc\rangle = |v\mathbf{k}_v, c\mathbf{k}_c\rangle = |v\mathbf{k}_v, c\mathbf{k}_v + \mathbf{Q}\rangle$. We write the change in potential due to atomic displacements as a sum of phonon interactions (See Sect. 1.2):

$$\Delta V = \sum_{\nu\mathbf{q}} \left(\frac{\hbar}{2\omega_{\nu\mathbf{q}}} \right)^{1/2} \Delta_{\nu\mathbf{q}} V^{\text{KS}} (\hat{b}_{\nu\mathbf{q}} + \hat{b}_{\nu-\mathbf{q}}^\dagger), \tag{3.25}$$

where $\hat{b}_{\nu\mathbf{q}}^\dagger$ and $\hat{b}_{\nu\mathbf{q}}$ are phonon creation and annihilation operators. That the Δ_{ij} describing the transition from i-th state to j-th state becomes:

$$\Delta_{n\mathbf{k}n'\mathbf{k}'} = \frac{\langle n'\mathbf{k}'|\Delta V|n\mathbf{k}\rangle}{\epsilon_{n\mathbf{k}} - \epsilon_{n'\mathbf{k}'}} = \sum_{\nu\mathbf{q}} \frac{g_{nn'\nu}(\mathbf{k},\mathbf{q})\delta(\mathbf{k}' - \mathbf{k} - \mathbf{q})}{\epsilon_{n\mathbf{k}} - \epsilon_{n'\mathbf{k}'}} (\hat{b}_{\nu\mathbf{q}} + \hat{b}_{\nu-\mathbf{q}}^\dagger) \tag{3.26}$$

where $g_{nn'\nu}(\mathbf{k},\mathbf{q}) = (\hbar/2\omega_{\nu\mathbf{q}})^{1/2} \langle n'\mathbf{k}'|\Delta_{\nu\mathbf{q}} V^{\text{KS}}|n\mathbf{k}\rangle$ is the usual e-ph matrix element in Eq. (3.1).

By introducing exciton creation and annihilation operators, $\hat{a}_{S_n(\mathbf{Q})}^\dagger$ and $\hat{a}_{S_n(\mathbf{Q})}$, we rewrite the ex-ph Hamiltonian in Eq. (3.22) as:

$$\begin{aligned} \tilde{H} = & \sum_{n\mathbf{Q}} E_{S_n(\mathbf{Q})} \hat{a}_{S_n(\mathbf{Q})}^\dagger \hat{a}_{S_n(\mathbf{Q})} + \sum_{\nu\mathbf{q}} \hbar\omega_{\nu\mathbf{q}} \hat{b}_{\nu\mathbf{q}}^\dagger \hat{b}_{\nu\mathbf{q}} \\ & + \sum_{nm\nu,\mathbf{Q}\mathbf{q}} \mathcal{G}_{nm\nu}(\mathbf{Q},\mathbf{q}) \hat{a}_{S_m(\mathbf{Q}+\mathbf{q})}^\dagger \hat{a}_{S_n(\mathbf{Q})} (\hat{b}_{\nu\mathbf{q}} + \hat{b}_{\nu-\mathbf{q}}^\dagger), \end{aligned} \tag{3.27}$$

where we defined the exciton-phonon matrix elements as:

$$\begin{aligned} \mathcal{G}_{nm\nu}(\mathbf{Q},\mathbf{q}) = & \sum_{\substack{vcv'c' \\ \mathbf{k}_v\mathbf{k}_c\mathbf{k}'_{v'}\mathbf{k}'_{c'}}} A_{v\mathbf{k}_v,c\mathbf{k}_c}^{S_m(\mathbf{Q}+\mathbf{q})*} A_{v'\mathbf{k}'_{v'},c'\mathbf{k}'_{c'}}^{S_n(\mathbf{Q})} \\ & \times \left[\delta_{vv'} g_{c'cv}(\mathbf{k}'_{c'},\mathbf{q}) \delta(\mathbf{k}_c - \mathbf{k}'_{c'} - \mathbf{q}) - \delta_{cc'} g_{vv'v}(\mathbf{k}_v,\mathbf{q}) \delta(\mathbf{k}'_{v'} - \mathbf{k}_v - \mathbf{q}) \right]. \end{aligned} \tag{3.28}$$

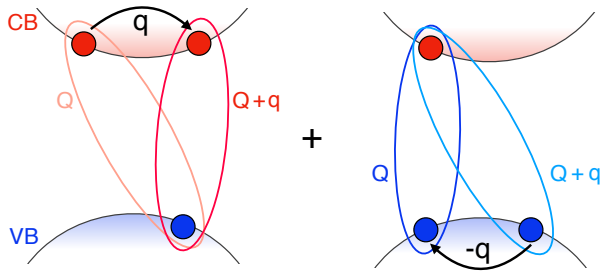

Figure 3.1: **Schematic of the exciton-phonon interaction** in Eq. (3.29). Ex-ph interaction can be viewed as a superposition of electron-phonon and hole-phonon scattering events, weighted by the wave functions of the initial and final exciton states.

The exciton-phonon coupling constant $\mathcal{G}_{nm\nu}(\mathbf{Q},\mathbf{q})$ is the probability amplitude for scattering from an exciton with band index n with center-of-mass momentum $\mathbf{Q}$ to an exciton with band index m and center-of-mass momentum $\mathbf{Q}+\mathbf{q}$. Since $A^{S(\mathbf{Q})}_{v\mathbf{k}_v,c\mathbf{k}_c} \neq 0$ only for $\mathbf{k}_c - \mathbf{k}_v = \mathbf{Q}$, in Eq. (3.28) we can impose three constraints, $\mathbf{k}_c - \mathbf{k}_v = \mathbf{Q}$, $\mathbf{k}'_c - \mathbf{k}'_v = \mathbf{Q}+\mathbf{q}$, and $\mathbf{k}'_c - \mathbf{k}_c = \mathbf{q}$ (or $\mathbf{k}'_v - \mathbf{k}_v = \mathbf{q}$). As a consequence, we drop three $\mathbf{k}$-point Brillouin zone (BZ) summations, and the final result for the ex-ph matrix element for a given exciton momentum $\mathbf{Q}$ and phonon momentum $\mathbf{q}$ becomes:

$$\mathcal{G}_{nm\nu}(\mathbf{Q},\mathbf{q}) = \sum_{\mathbf{k}} \left[\sum_{vcc'} A^{S_m(\mathbf{Q}+\mathbf{q})*}_{v\mathbf{k},c(\mathbf{k}+\mathbf{Q}+\mathbf{q})} A^{S_n(\mathbf{Q})}_{v\mathbf{k},c'(\mathbf{k}+\mathbf{Q})} g_{c'cv}(\mathbf{k}+\mathbf{Q},\mathbf{q}) - \sum_{cvv'} A^{S_m(\mathbf{Q}+\mathbf{q})*}_{v(\mathbf{k}-\mathbf{q}),c(\mathbf{k}+\mathbf{Q})} A^{S_n(\mathbf{Q})}_{v'\mathbf{k},c(\mathbf{k}+\mathbf{Q})} g_{vv'\nu}(\mathbf{k}-\mathbf{q},\mathbf{q}) \right]. \quad (3.29)$$

This ex-ph coupling, which is pictorially shown in Fig. 3.1, is a quantum superposition of electron- and hole-phonon scattering processes, weighted by the exciton wave functions of the initial and final states.

Numerical Implementation

Current algorithm is structured in two sections, see Fig. 3.2. The first part implements the Eq. (3.29) as a post-processing treatment combining the exciton wave function from YAMBO [86] and the e-ph coupling constant from PERTURBO [90] to calculate the ex-ph matrix element. The second part uses the ex-ph matrix element to compute physical observable, including features of:

1. Interpolation and plotting the electron-, exciton-band structure, and phonon dispersion

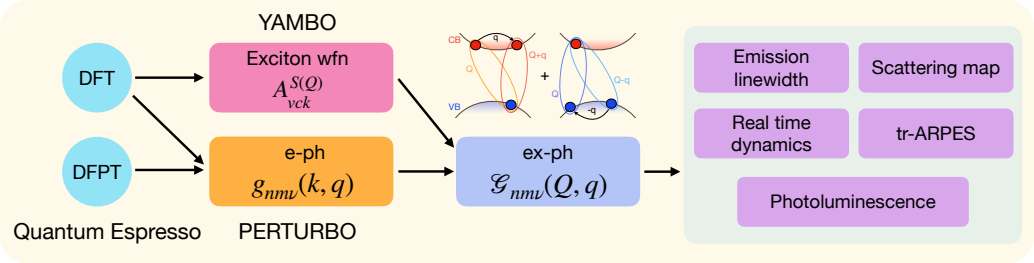

Figure 3.2: **Exciton-phonon dynamics numerical workflow.**

2. Calculating the ex-ph relaxation linewidth and its temprature dependence
3. Mapping out the exciton scattering path
4. Computing the phonon-assisted PL spectrum
5. Conducting real-time (RT) simulation using ex-ph Boltzmann transport equation (BTE)
6. Predicting the time-resoled ARPES signal using the result from BTE-RT simulation.

To our knowlegde, this computational routine is the only numerical scheme to calculate the ex-ph coupling and corresponding dynamics from first principle. The computation cost of ex-ph matrix element is expensive and scaling with $n_k^3 \times n_b^2 \times n_\nu$, where n_k is the number of k-points used, n_b is the number of exciton band involved in the later discussion on exciton dynamics, and n_ν is the number of phonon vibration modes. For instance, with energy cutoff and symmetry $\mathcal{G}_{mn\nu}(\mathbf{Q}+\mathbf{q}, -\mathbf{q}) = \mathcal{G}^*_{nm\nu}(\mathbf{Q}, \mathbf{q})$ implemented, in h-BN on $36\times36\times4$ k-gird, it costs $\gtrsim$10000 CPU hour to compute for 25 bands in full BZ. So far, some optimizating works are ongoing and all functions are now merging into the framework of the PERTURBO code.

In the following, based on the developed approach, we perform studies on the Bulk h-BN and monolayer WSe_2 to investigate the ex-ph dynamics and corresponding physical quantities.

3.2 Exciton-Phonon Signature in Bulk Hexagonal Boron Nitride

In this section, we apply our scheme to study excitons in bulk h-BN. The h-BN has attracted attention in past decades as a high efficient light emitter with large band gap (about 7 eV) deep in the UV spectrum. Even in the bulk-form, the weak Coulomb

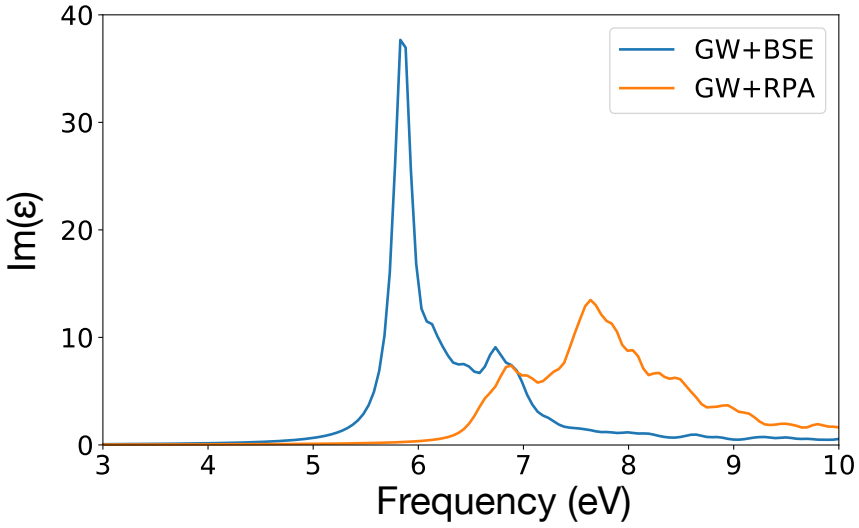

Figure 3.3: **Absorption spectrum of bulk h-BN**

screening effect along its stacking direction leaves strong electron-hole attraction which leads to the significant excitonic effect in the material. L. Wirtz et. al. [223] first used the GW-BSE method to compute the h-BN absorption spectrum and point out the importance of excitonic modulation in h-BN optical properties. As shown in Fig. 3.3, with electron-hole attraction included the absorption spectrum possesses a strong resonant pole below the electronic gap corresponding to the formation of exciton which is missed when the independent particle picture is employed under Random Phase Approximation (RPA). However, the inclusion of exciton effect didn't resolve the mystery of h-BN. As a material of indirect gap, h-BN has extraordinary quantum yield of 50 % which is believed to be observed only in direct-gap material [13]. Until a recent observation of h-BN PL, the strong light emission is concluded as a result of phonon interaction [224] which is later supported by a theoretical work [208] using TDDFT method. Provided with strong excitonic effect and fruitful phonon modulated optical properties, h-BN can serve as an idea material which hosts remarkable signatures of ex-ph interaction to investigate. In the following, we present the derivations and the computed results for observable, including the ex-ph relaxation time and phonon-assisted PL, while the numerical details are provided in Appendix H.

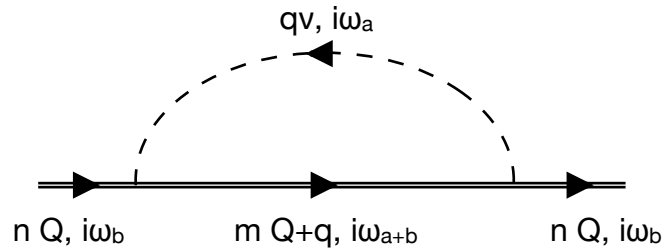

Figure 3.4: **Ex-ph self-energy diagram.** One-loop exciton self-energy due to the ex-ph interaction

Ex-ph Relaxation Time and Scattering rate

To study the ex-ph scattering rate, we derive the formalism based on the optical theorem, which relates the scattering rate (inverse of the relaxation time τ) and the imaginary part of the self-energy Σ:

$$\frac{1}{\tau} = -(2/\hbar)\mathrm{Im}\Sigma. \tag{3.30}$$

Consider the one-loop exciton self-energy, we utilize the method of Matsubara frequency summation to calculate the Feynman diagram in Fig. 3.4. Using the imaginary time coordinate and imaginary frequency, as is usual in the Matsubara technique, the propagator for a boson (here, an exciton or a phonon) is written as:

$$\mathcal{D}_n(i\omega_a, \mathbf{k}) = \frac{1}{i\omega_a - E_{n\mathbf{k}}} - \frac{1}{i\omega_a + E_{n\mathbf{k}}}, \tag{3.31}$$

where n is the band index for excitons or the mode index for phonons, $E_{n\mathbf{k}}$ is the on-shell energy, and the Matsubara frequency is defined as:

$$\omega_a = \frac{2\pi}{\beta}a \quad \text{with } a \in \mathbb{Z},\ \beta = \frac{1}{k_B T}. \tag{3.32}$$

More information on the optical theorem and Matsubara's method can be found in Ref. [225]. The self-energy diagram in Fig. 3.4 can be evaluated as follows:

$$\begin{aligned}
\Sigma_n(i\omega_b, \mathbf{Q}) &= \frac{-1}{\beta N_{\mathbf{q}}} \sum_{m\mathbf{q}\nu a} |\mathcal{G}_{nm\nu}(\mathbf{Q}, \mathbf{q})|^2 \mathcal{D}_m(i\omega_{a+b}, \mathbf{Q}+\mathbf{q}) \mathcal{D}_\nu(i\omega_a, \mathbf{q}) \\
&= \frac{-1}{\beta N_{\mathbf{q}}} \sum_{m\mathbf{q}\nu a} |\mathcal{G}_{nm\nu}(\mathbf{Q}, \mathbf{q})|^2 \\
&\quad \times \left[\frac{1}{i\omega_{a+b} - E_{m\mathbf{Q}+\mathbf{q}}} - \frac{1}{i\omega_{a+b} + E_{m\mathbf{Q}+\mathbf{q}}}\right] \left[\frac{1}{i\omega_a - E_{\nu\mathbf{q}}} - \frac{1}{i\omega_a + E_{\nu\mathbf{q}}}\right] \\
&= \frac{-1}{\beta N_{\mathbf{q}}} \sum_{m\mathbf{q}\nu a} |\mathcal{G}_{nm\nu}(\mathbf{Q}, \mathbf{q})|^2
\end{aligned}$$

$$\times \left[\left(\frac{1}{i\omega_{a+b} - E_{m\mathbf{Q}+\mathbf{q}}} - \frac{1}{i\omega_a - E_{\nu\mathbf{q}}} \right) \times \frac{1}{E_{m\mathbf{Q}+\mathbf{q}} - E_{\nu\mathbf{q}} - i\omega_b} \right.$$
$$- \left(\frac{1}{i\omega_{a+b} - E_{m\mathbf{Q}+\mathbf{q}}} - \frac{1}{i\omega_a + E_{\nu\mathbf{q}}} \right) \times \frac{1}{E_{m\mathbf{Q}+\mathbf{q}} + E_{\nu\mathbf{q}} - i\omega_b}$$
$$\left. + \left(\frac{1}{i\omega_{a+b} + E_{m\mathbf{Q}+\mathbf{q}}} - \frac{1}{i\omega_a + E_{\nu\mathbf{q}}} \right) \times \frac{1}{-E_{m\mathbf{Q}+\mathbf{q}} + E_{\nu\mathbf{q}} - i\omega_b} \right]. \quad (3.33)$$

To simplify the expression, we apply the identity for the Bose-Einstein statistics:

$$\mathcal{N}(\epsilon) = \frac{1}{e^{\beta\epsilon} - 1} = -\frac{1}{2} - \frac{1}{\beta} \sum_{n=-\infty}^{\infty} \frac{1}{2ni\pi/\beta - \epsilon}, \quad (3.34)$$

and get:

$$\Sigma_n(i\omega_b, \mathbf{Q}) = \frac{-1}{\mathcal{N}_\mathbf{q}} \sum_{m\mathbf{q}\nu} |\mathcal{G}_{nm\nu}(\mathbf{Q}, \mathbf{q})|^2$$
$$\times \left[\left(N_{\nu\mathbf{q}} - F_{m\mathbf{Q}+\mathbf{q}}\right) \times \left(\frac{1}{E_{m\mathbf{Q}+\mathbf{q}} - E_{\nu\mathbf{q}} - i\omega_b} - \frac{1}{-E_{m\mathbf{Q}+\mathbf{q}} + E_{\nu\mathbf{q}} - i\omega_b} \right) \right.$$
$$\left. - \left(N_{\nu\mathbf{q}} + 1 + F_{m\mathbf{Q}+\mathbf{q}}\right) \times \left(\frac{1}{-E_{m\mathbf{Q}+\mathbf{q}} - E_{\nu\mathbf{q}} - i\omega_b} - \frac{1}{+E_{m\mathbf{Q}+\mathbf{q}} + E_{\nu\mathbf{q}} - i\omega_b} \right) \right], \quad (3.35)$$

where we changed the notation to distinguish the exciton and phonon sectors by renaming $\mathcal{N}(E_{\nu\mathbf{q}}) \to N_{\nu\mathbf{q}}$ for phonons and $\mathcal{N}(E_{m\mathbf{Q}+\mathbf{q}}) \to F_{m\mathbf{Q}+\mathbf{q}}$ for excitons. Lastly, we use analytical continuation to extend the complex function Σ from the imaginary exciton energy to full complex plane, by setting $i\omega_b \to E_{n\mathbf{Q}} + i\epsilon$ with infinitesimal positive deviation ϵ from the real exciton energy axis. The ex-ph scattering rate is obtained by applying the optical theorem in Eq. (3.30) and computing the imaginary part of the self-energy through the identity:

$$\frac{1}{x + i\epsilon} = P\frac{1}{x} - i\pi\delta(x), \quad (3.36)$$

where ϵ is a positive infinitesimal and P takes the principal value of $1/x$. The total exciton scattering rate obtained this way consists of multiple terms, in which we denote the exciton energies as E and the phonon energies as $\hbar\omega$:

$$\Gamma_{n\mathbf{Q}}(T) = \frac{2\pi}{\hbar} \frac{1}{\mathcal{N}_\mathbf{q}} \sum_{m\mathbf{q}\nu} |\mathcal{G}_{nm\nu}(\mathbf{Q}, \mathbf{q})|^2$$
$$\left[\left(N_{\nu\mathbf{q}} - F_{m\mathbf{Q}+\mathbf{q}}\right) \times \left(\delta(E_{n\mathbf{Q}} - E_{m\mathbf{Q}+\mathbf{q}} + \hbar\omega_{\nu\mathbf{q}}) - \delta(E_{n\mathbf{Q}} + E_{m\mathbf{Q}+\mathbf{q}} - \hbar\omega_{\nu\mathbf{q}}) \right) \right.$$
$$\left. + \left(N_{\nu\mathbf{q}} + 1 + F_{m\mathbf{Q}+\mathbf{q}}\right) \times \left(\delta(E_{n\mathbf{Q}} - E_{m\mathbf{Q}+\mathbf{q}} - \hbar\omega_{\nu\mathbf{q}}) - \delta(E_{n\mathbf{Q}} + E_{m\mathbf{Q}+\mathbf{q}} + \hbar\omega_{\nu\mathbf{q}}) \right) \right]. \quad (3.37)$$

The four terms in Eq. (3.37) correspond to phonon absorption, two excitons combining into a phonon, phonon emission, and 3-particle annihilation, respectively. We ignore the two terms due to two excitons combining into a phonon and annihilation of two excitons and a phonon since they are not relevant here (the 3-particle annihilation process is also prohibited by energy conservation), keeping only the phonon emission and absorption terms. We thus obtain the ex-ph scattering rate:

$$\Gamma^{\text{ex-ph}}_{n\mathbf{Q}}(T) = \frac{2\pi}{\hbar}\frac{1}{\mathcal{N}_{\mathbf{q}}}\sum_{m\nu\mathbf{q}}|\mathcal{G}_{nm\nu}(\mathbf{Q},\mathbf{q})|^2 \times\Big[(N_{\nu\mathbf{q}}+1+F_{m\mathbf{Q}+\mathbf{q}})\times\delta(E_{n\mathbf{Q}}-E'_{m\mathbf{Q}+\mathbf{q}}-\hbar\omega_{\nu\mathbf{q}}) +(N_{\nu\mathbf{q}}-F_{m\mathbf{Q}+\mathbf{q}})\times\delta(E_{n\mathbf{Q}}-E'_{m\mathbf{Q}+\mathbf{q}}+\hbar\omega_{\nu\mathbf{q}})\Big], \quad (3.38)$$

where N and F are phonon and exciton occupations, $\mathcal{N}_{\mathbf{q}}$ is the number of $\mathbf{q}$-points, and the first and second terms in bracket correspond, respectively, to an exciton emitting or absorbing one phonon. Within this approach, the temperature dependence of the relaxation times is due to the phonon and exciton occupation factors, while the exciton wave functions and energies are computed with the BSE on a fixed atomic structure at zero temperature.

Using Eq. (3.38), we compute the exciton relaxation time and the ex-ph scattering rate in bulk h-BN and summarize the results in Fig. 3.5. We first show the exciton band structure along a high-symmetry line for the lowest 8 exciton bands, overlaid with the ex-ph relaxation times at 77 K using color code in Fig. 3.5(a). Our exciton band structure agrees well with previous results [226, 227], apart from a small rigid energy shift; the global minimum is located close to a point called here Q, the halfway point between Γ and K, which corresponds to the excitation across the indirect electronic band gap of h-BN. Note also that in our calculation the degeneracy between the 3rd and 4th exciton bands at Γ is lifted due to the inclusion, different from Refs. [226, 227], of the $\mathbf{G} = 0$ Hartree term in the BSE kernel, which splits transverse and longitudinal excitons.

Our computed ex-ph relaxation times are of order 5−100 fs, corroborating the widely used assumption that excitons thermalize rapidly before recombining. The relaxation times are strongly energy dependent. At 77 K, they are of order 100 fs near the exciton energy minima, and drop rapidly to ∼15 fs above the threshold for LO phonon emission, located 160 meV above the exciton energy minima [at exciton energy of 4.95 eV; see Fig. 3.5(a)]. Analysis of the ex-ph coupling strength [Fig. 3.5(c)] and scattering rate due to each individual phonon mode reveals that

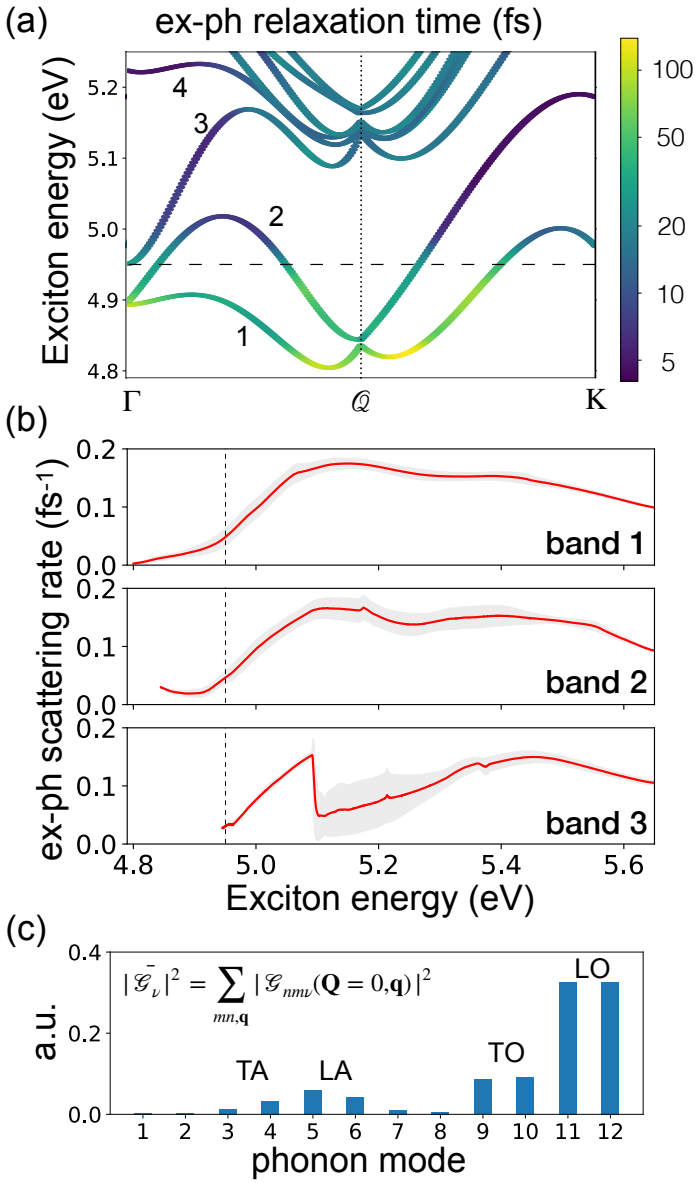

Figure 3.5: **Ex-ph relaxation time and scattering rate.** (a) Exciton band structure for the four lowest-energy exciton bands, together with a log-scale color map of ex-ph relaxation times at 77 K. Note the drop in the relaxation times above the LO emission threshold at 4.95 eV, which is shown with a dashed line. (b) Average ex-ph scattering rates as a function of exciton energy, up to 5.7 eV for three chosen exciton states. The shaded region gives the standard deviation of the momentum-dependent scattering rate at each energy. (c) The squared ex-ph coupling strength (in arbitrary units) for the 12 phonon modes of h-BN.

above this threshold the strongest scattering channel is the emission of an LO phonon with average phonon energy of 160 meV. Since the exciton energy minimum is at 4.8 eV, only excitons with energy greater than 4.95 eV can emit an LO phonon and scatter to a final exciton state, which explains the much shorter relaxation times above the LO emission threshold. This trend is analogous to the e-ph scattering rates in polar semiconductors (e.g., GaAs), where electrons couple strongly with LO phonons and the relaxation time drops rapidly above the LO emission threshold [201].

Fig. 3.5(b) shows the ex-ph scattering rates as a function of exciton energy, averaged over exciton momentum, for exciton bands 1−3. For the lowest-energy excitons in band 1, the scattering rate increases monotonically with energy between 4.8−5.05 eV, with a change of slope at 4.95 eV due to the onset of LO phonon emission. We find an LO phonon emission time of ∼15 fs for excitons at 77 K, a value comparable to LO phonon emission times for electrons in polar semiconductors [201]. Compared to excitons in band 1, the scattering rate is higher at low energy for excitons in band 2, which can emit phonons with a range of energies and transition to band 1. Excitons in band 3 exhibit a drop in the scattering rate at 5.1 eV due to the energy minima near Q with significant energy gaps from the two lower bands. We have also verified that treating the electrons and holes as independent particles, thus computing the square ex-ph matrix element as the incoherent sum of the electron- and hole-phonon coupling, $|G|^2 \approx |g_{cc'}|^2 + |g_{vv'}|^2$, leads to order-of-magnitude errors in the ex-ph scattering rates compared to the correct treatment in Eq. (3.29) that includes excitonic effects.

The momentum dependence of the relaxation times is controlled by the exciton band structure, which provides the phase space for scattering, and by the ex-ph matrix elements. Fig. 3.6 analyzes the exciton relaxation times (for two specific bands, 2 and 4) as a function of exciton momentum in the Brillouin zone, together with the average ex-ph coupling strength, defined as $\bar{\mathcal{G}}_n(\mathbf{Q}) = \sum_{m\nu\mathbf{q}} |\mathcal{G}_{nm\nu}(\mathbf{Q},\mathbf{q})|^2$. Both the ex-ph coupling and relaxation times exhibit the six-fold symmetry of h-BN. As a general trend, we find that larger coupling strengths are associated with shorter relaxation times, consistent with Eq. (3.38). The relaxation times are maximal near the exciton local energy minima at Q (and also at Γ for band 2), where the anisotropic exciton dispersion gives rise to ellipsoid-shaped regions in momentum space with longer relaxation times.

Understanding how temperature affects exciton dynamics is crucial in experiments. Fig. 3.7 compares the temperature dependence of the ex-ph scattering rates for

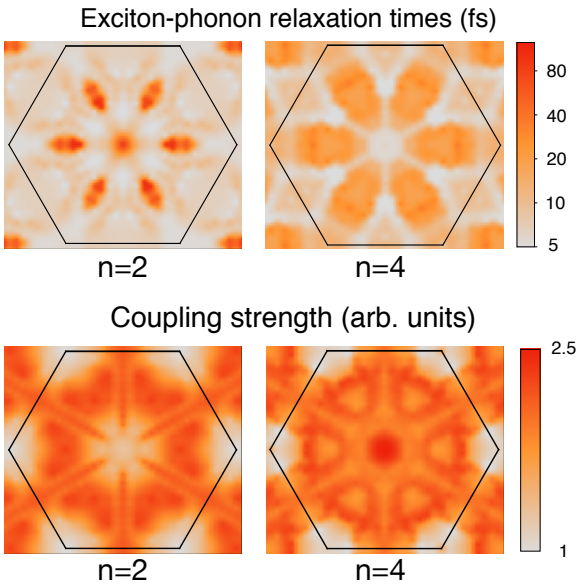

Figure 3.6: **Ex-ph relaxation and coupling strength map.** Exciton-phonon relaxation times at 77 K, shown as a function of exciton momentum in the Brillouin zone plane parallel to the h-BN layers. The lower panel shows the average coupling strength $\bar{\mathcal{G}}_n(\mathbf{Q})$ in arbitrary units, where red color indicates stronger coupling. In both panels, the color maps are given on a log-scale.

two exciton states, one above and one below the LO-phonon emission threshold. The scattering rate increases monotonically from 1 to 300 K for both states, but with rather different trends. For the state below the LO emission threshold, the scattering rate increases by over an order of magnitude between 1−300 K, while the increase for the state above the LO emission threshold is much smaller, only about 10 percent over the same temperature range. We find similar trends when inspecting other states in these two energy windows. Analysis of the contributions to exciton scattering from the different phonon modes [see Fig. 3.7(c)] reveals that excitons below the LO emission threshold and close to the energy minima mainly scatter by absorbing low-energy acoustic phonons, which explains the strong temperature dependence. On the other hand, at energies above the LO emission threshold, scattering is dominated by LO phonon emission, a weakly temperature dependent process with rate proportional to N+1 [see Eq. (3.38)].

Phonon-Assisted Photoluminescence

The photoluminescence intensity $I(\omega)$ is defined as the number of photons with frequency ω emitted per unit time. The source of emitted photons is the radiative

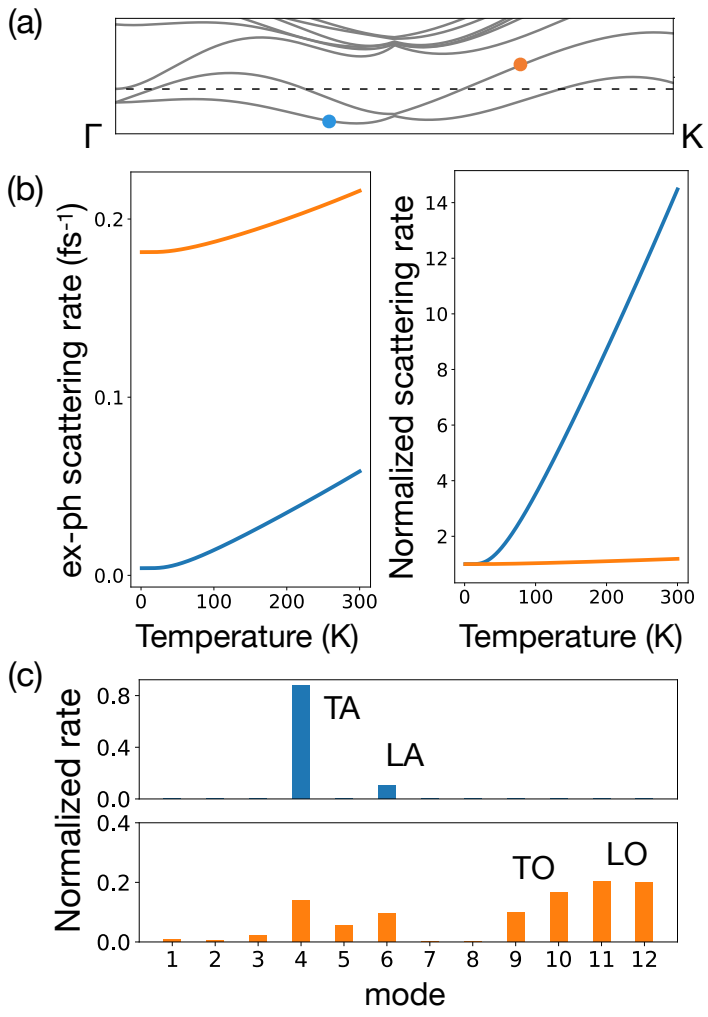

Figure 3.7: **Temperature dependence of ex-ph scattering rate.** Ex-ph scattering rate as a function of temperature for an exciton state below (blue) and above (orange) the LO-emission threshold. (a) The two states selected for the analysis are shown in the exciton band structure. (b) The absolute value of the scattering rates (left) and the same quantities normalized by the scattering rate at 1 K for each state (right) to emphasize the stronger temperature dependence for the state below the LO emission threshold. (c) Mode-resolved contribution to the scattering rate at 1 K, normalized by the total rate for each state.

decay of excitons, and thus we can write:

$$I(\omega) = \frac{dn_\omega}{dt} = -\sum_n \int d\mathbf{Q} \frac{dN_{n\mathbf{Q}}}{dt} = \sum_n \int d\mathbf{Q} \Gamma_n(\mathbf{Q}, \omega) N_{n\mathbf{Q}} \tag{3.39}$$

where n_ω is the number of photons with energy ω, $N_{n\mathbf{Q}}$ is the number of excitons in a given state (with exciton band n and momentum $\mathbf{Q}$), which follows the Bose-Einstein distribution at low exciton density, and $\Gamma_n(\mathbf{Q}, \omega)$ is the radiative rate of the same exciton state for emitting a photon with frequency ω. Due to momentum conservation, excitons with a large enough finite momentum cannot emit a photon directly. The next-order emission processes is phonon-assisted luminescence, in which an exciton can emit or absorb a phonon and change its momentum before emitting the photon. We again derive the process rate using the optical theorem, by computing the imaginary part of the self-energy diagram in Fig. 3.8 as:

$$\begin{aligned}\Sigma_n(i\omega_b, \mathbf{Q}) = \frac{-1}{\beta \mathcal{N}_\mathbf{q}} \sum_{m\mathbf{q}\nu a} |\mathbf{A} \cdot \mathbf{p}_m(\mathbf{Q}+\mathbf{q})|^2 \cdot |\mathcal{G}_{nm\nu}(\mathbf{Q}, \mathbf{q})|^2 \\ \times [\mathcal{D}_m(i\omega_{a+b}, \mathbf{Q}+\mathbf{q})]^2 \, \mathcal{D}_\nu(i\omega_a, \mathbf{q}) \mathcal{D}_\omega(i\omega_{a+b}, \mathbf{Q}+\mathbf{q}),\end{aligned} \tag{3.40}$$

where $\mathbf{q}$ is the phonon momentum and $|\mathbf{A} \cdot \mathbf{p}|$ is the standard exciton-photon interaction within minimal coupling. We impose several conditions to compute the physical process we are interested in. First, the photon momentum is negligible compared to the crystal momentum, and thus we can set $\mathbf{Q}+\mathbf{q} \approx 0$ (see Fig. 3.8). In h-BN, we take the lowest two bright excitons (with zero momentum) for the optically active exciton states; these two states are degenerate, with equal-in-magnitude but perpendicular dipole moment $\mathbf{p}$. Since we focus on photon emission in a temperature range where phonon absorption is negligible compared to phonon emission, we use only the emission part of the photon and phonon propagators:

$$\mathcal{D}_\nu(i\omega_a, \mathbf{q}) \approx -\frac{1}{i\omega_a + \hbar\omega_{\nu\mathbf{q}}}, \qquad \mathcal{D}_\omega(i\omega_a, \mathbf{q}) \approx \frac{1}{i\omega_a - \hbar\omega}. \tag{3.41}$$

Note that the different sign in the photon and phonon propagators is due to the opposite directions of the propagation arrows in the self-energy diagram in Fig. 3.8. For the same reason, since only the emission process is considered, the intermediate exciton state propagator becomes:

$$\mathcal{D}_m(i\omega_a, \mathbf{Q}) \approx \frac{1}{i\omega_a - E_{m\mathbf{Q}}}. \tag{3.42}$$

As a result, the self-energy takes a simpler expression, which with constants neglected reads:

$$\Sigma_n(i\omega_b, \mathbf{Q}) \quad \propto \quad \frac{-1}{\beta \mathcal{N}_\mathbf{q}} \sum_{m\nu a} |\mathcal{G}_{nm\nu}(\mathbf{Q}, -\mathbf{Q})|^2 \left[\frac{1}{i\omega_{a+b} - E_{m\Gamma}}\right]^2 \frac{-1}{i\omega_a + \hbar\omega_{\nu\mathbf{Q}}} \frac{1}{i\omega_{a+b} - \hbar\omega}$$

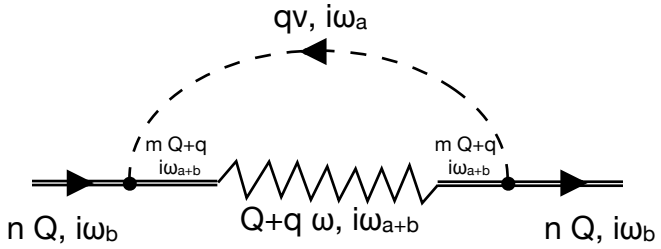

Figure 3.8: **Phonon-assisted photoluminescence diagram.** One-loop exciton self-energy due to ex-ph processes involving photon emission. From left to right, the exciton (double solid line) emits or absorbs a phonon with momentum $\mathbf{q}$ (dashed line), and then emits a photon (zigzag line) with momentum $\mathbf{Q}+\mathbf{q} \approx 0$. The process then rewinds to form the self-energy loop.

$$= \frac{-1}{\beta \mathcal{N}_{\mathbf{q}}} \sum_{m\nu a} \left(I^{(1)} + I^{(2)} + I^{(3)} \right), \tag{3.43}$$

where with some algebra we separate the self-energy into three terms:

$$\begin{aligned}
I^{(1)} &= \frac{-1}{(E_{m\Gamma} - \hbar\omega)^2} \frac{1}{i\omega_b - \hbar\omega - \hbar\omega_{\nu\mathbf{Q}}} \left(\frac{1}{i\omega_{a-b} + \hbar\omega_{\nu\mathbf{Q}}} - \frac{1}{i\omega_a - \hbar\omega} \right) \\
I^{(2)} &= \frac{1}{(i\omega_b - E_{m\Gamma} - \hbar\omega_{\nu\mathbf{Q}})^2} \frac{1}{E_{m\Gamma} - \hbar\omega} \left(\frac{1}{i\omega_a - E_{m\Gamma}} - \frac{1}{i\omega_{a-b} + \hbar\omega_{\nu\mathbf{Q}}} \right) \\
I^{(3)} &= \frac{1}{i\omega_b - E_{m\Gamma} - \hbar\omega_{\nu\mathbf{Q}}} \times \left[\frac{1}{E_{m\Gamma} - \hbar\omega} \frac{1}{(i\omega_a - E_{m\Gamma})^2} \right. \\
&\quad \left. + \frac{1}{(E_{m\Gamma} - \hbar\omega)^2} \left(\frac{1}{i\omega_a - E_{m\Gamma}} + \frac{1}{i\omega_{a-b} + \hbar\omega_{\nu\mathbf{Q}}} - \frac{2}{i\omega_a - \hbar\omega} \right) \right].
\end{aligned} \tag{3.44}$$

The terms $I^{(1)}$, $I^{(2)}$ and $I^{(3)}$ are arranged according to their pole behavior. In particular, $I^{(1)}$ has pole at $i\omega_b - \hbar\omega - \hbar\omega_{\nu\mathbf{Q}} = 0$, while $I^{(2)}$ and $I^{(3)}$ have a double and simple pole, respectively, at $i\omega_b - E_{m\Gamma} - \hbar\omega_{\nu\mathbf{Q}} = 0$. After setting $i\omega_b \longrightarrow E_{n\mathbf{Q}} + i\epsilon$, only the first pole at $i\omega_b - \hbar\omega - \hbar\omega_{\nu\mathbf{Q}} = 0$ is associated with our process of interest, in which the initial exciton emits a phonon and transitions to a virtual bright state before emitting light. The other pole corresponds to an on-shell intermediate state (rather than a virtual one) and is negligible at low temperature since there are no excitons with a high enough energy for this process to occur. Therefore, we keep only the $I^{(1)}$ term. Using the identity in Eq. (3.34) and ignoring overall constant factors, we obtain the phonon-assisted radiative rate:

$$\Gamma_n(\mathbf{Q}, \omega) \propto \sum_{m \in \text{bright exciton}} \left[\sum_{\nu} |\mathcal{G}_{nm\nu}(\mathbf{Q}, -\mathbf{Q})|^2 \cdot \frac{1 + N(\hbar\omega_{\nu\mathbf{Q}})}{(\hbar\omega - E_m)^2} \cdot \delta\left(\hbar\omega + \hbar\omega_{\nu\mathbf{Q}} - E_{n\mathbf{Q}}\right) \right]. \tag{3.45}$$

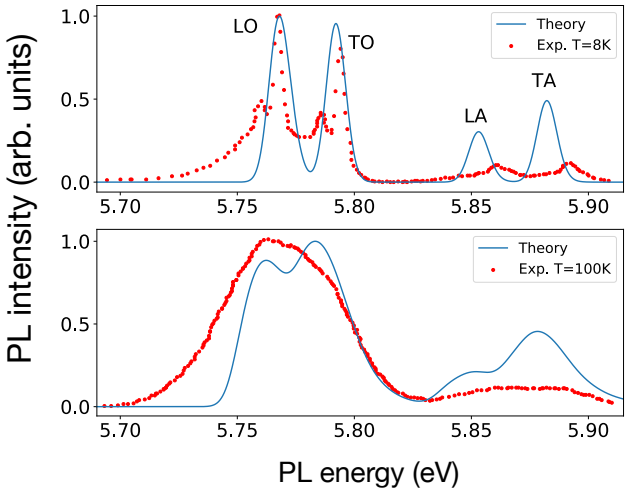

Figure 3.9: **Phonon-assisted photoluminescence in h-BN.** Comparison between the computed phonon-assisted PL intensity (blue curve) and experimental data from Ref. [228] (red dots). The calculated spectra were shifted by ∼1 eV and normalized to match the first peak of the measured spectra.

Substituting this rate in Eq. (3.39), we finally obtain phonon-assisted photoluminescence formula:

$$I(\omega) = \sum_{n} \int d\mathbf{Q} \Gamma_n(\mathbf{Q}, \omega) N_{n\mathbf{Q}}$$
$$\propto \sum_{nm\nu} |p_{S_m}|^2 \int d\mathbf{Q} \, |\mathcal{G}_{nm\nu}(\mathbf{Q}, -\mathbf{Q})|^2 \cdot N_{n\mathbf{Q}} \frac{1 + N(\hbar\omega_{\nu\mathbf{Q}})}{(\hbar\omega - E_m)^2} \cdot \delta\left(\hbar\omega + \hbar\omega_{\nu\mathbf{Q}} - E_{n\mathbf{Q}}\right). \tag{3.46}$$

Using Eq. (3.46), we compute the phonon-assisted PL spectrum in h-BN, obtaining results in agreement with PL experiments between 8−100 K up to a blue-shift of the spectrum[3] (see Fig. 3.9). At low temperature of 8 K, our computed PL exhibits all four peaks seen in experiment, which correspond to LO, TO, LA and TA phonon-assisted PL. We find dominant LO and TO peaks due to the strong ex-ph coupling of these phonon modes. At 100 K, the PL peak linewidths accurately match the experimental data. We have explicitly verified that including the real part of the ex-ph self-energy in our calculation only causes a rigid red shift of the PL spectrum by about 50 meV. Yet, the computed acoustic peaks are too intense, and the relative LO and TO peak intensities at 8 K (but not at 100 K) are sensitive to the broadening

[3]Note that in Ref. [213], which employs a self-consistent GW_0 approach to obtain an improved value of the band gap, a 0.3 eV blue shift sufficed to match the experimental PL spectrum. Our work employs G_0W_0, resulting in an underestimate of the quasiparticle band gap, so a larger blue shift is needed.

used in the PL intensity formula Eq. (3.45). Additional work is needed to fully converge these fine features of the PL spectra.

3.3 Exciton-Phonon Dynamics in Monolayer Tungsten Diselenide

While researchers has advanced the synthesis technology [229, 230] and optical spectroscopic techniques [17, 58, 231, 232] in TMDs and obtained great success in applying the BSE method to study bright exciton physics[4], a great part of the full genus of exciton and corresponding phenomena are unexplored. For instance, the PL spectra of TMDs as light emitters is not yet understood. Multiple emission peaks are observed below the main direct transition energy and play significant roles in cryogenic temperature, especially for materials with an indirect band gap [228, 233]. Besides, even for the bright exciton emission, the underlying mechanism for linewidth broadening and the instability of the polarization, i.e. the depolarization effect, is not revealed. Such signals are phenomenologically explained to be induced by lattice vibration but with no sufficient theoretical proof. In the following, we apply the ex-ph interaction formalism and discuss its effect in monolayer WSe_2. We investigate the general optical phenomena including emission linewidth as well as PL spectrum, and further develop an algorithm for realtime simulation to study the exciton valley depolarization effect in WSe_2. The results successfully predict the temperature trend of the bright exciton linewidth and correctly identify the phonon contribution in the PL spectrum. The real-time simulation quantify the exciton depolarization time scale of ~100 fs at 77 K. Overall, our results lay out new microscopic insight for phonon-modulated light emission behaviors and the valley depolarization mechanism in WSe_2 which can be generalized to the entire 2D-TMD family. The detailed computational information can be found in Appendix I.

Bright exciton linewidth and photoluminescence in monolayer WSe_2

The study of bright exciton linewidth can indirectly reveals the secret of the dark exciton via ex-ph interactions. The homogeneous broadening of the emission line is related to the exciton coherence lifetime [234] :

$$\sigma_{\text{exciton linewidth}} = \hbar\tau^{-1}_{\text{coherence lifetime}} = \hbar\Gamma(T), \tag{3.47}$$

where, in the right hand side, the Γ is the ex-ph relaxation rate, given in Eq. (3.38). Thus, the existence of dark exciton states can provide the scattering channel for

[4] See Sect. 2.3 and corresponding reference.

phonon-absorption and emission and thus shorten the coherence, resulting in the wideness of the bright peak in the emission spectrum. On the other hand, the analysis on PL spectrum can directly bring out the dark exciton structure and its phonon interaction. Indirect excitons possess finite-momentum electron-hole transition outside the light-cone region ($E > \hbar c|\mathbf{k}|$) [48] and are forbidden from radiative recombination. But with the modulation from lattice vibration, phonon interaction provides a path way for excitons to avoid this restriction, by first emitting or absorbing phonons to release its exceeding momentum to satisfy the light-cone condition and under go light emission [224]. Therefore, the PL spectrum involves information, including the dark exciton energy levels and ex-ph coupling strength, and serves as an idea physical quantity for dark exciton research, especially in material with indirect gap, like monolayer WSe_2.

Monolayer WSe_2, in early study, was believed as a material with direct band gap [127, 235, 236] which locates at the K/K′ corner of its hexagonal Brillouin zone, like other TMD memebers. However, recent measurements show more evidence on its indirect gap [237] with the true conduction band minimum lying at the middle of Γ-K line (denoted at Q point) which is lower by 80 ± 80 meV than the K-point minimum [128]. Our one-shot G_0W_0-correction, however, overestimates this difference which provides $E_K - E_Q > 300$ meV for the lowest conduction band. As a result, to avoid possible error, we employ the experimental measurement [128] as a reference to fine-tune our calculated band structure, by tilting and stretching the conduction bands to meet the 80 meV difference while maintaining the valence bands.

Based on the tuned electronic band structure we apply the ex-ph scheme and Eq. (3.38, 3.47) to compute the bright exciton linewidth under temperature from 0 K-250 K and present the result in Fig. 3.10(a). Here we focus on the bright exciton locating solely in one of the K-valley which corresponds to the excitation from the circularly polarized incident pumping. The result shows great agreement with the experimental data up to a rigid 9 meV shift [238]. We attribute the difference to temperature-independent factors, including the radiative decay and possible defect trapping. In addition to reproducing the experimental result, our calculations provide more information on the scattering path. By leaving out the summation over phonon momentum in Eq. (3.38) when applied in Eq. (3.47), we provide the momentum-resolved map in Fig. 3.10(b). It shows that the Γ-M scattering channel is the dominant path for bright exciton relaxation with Γ-Q scattering being the secondary, which also reflects the observation in earlier reports [239]. Furthermore,

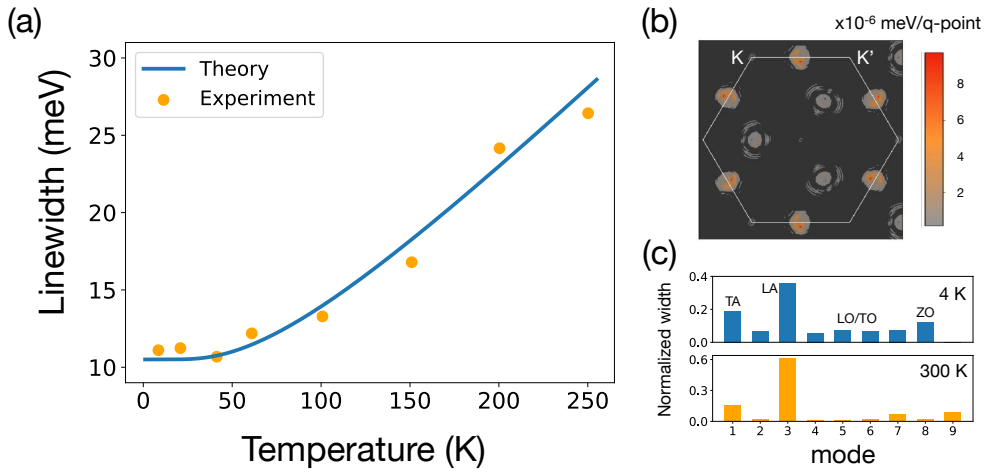

Figure 3.10: **Bright exciton linewidth in WSe_2.** (a) Emission linewidth of bright K exciton (excited by circularly polarized light) at temperature from 0 K to 250 K, compared with experiment. Inset shows two main ex-ph scatter processes for bright exciton relaxation, Γ to M and Γ to Q. (b) Phonon momentum resolved contribution to the linewidth at T= 300 K. In addition to the main scattering with **q**=M phonon, the secondary contribution lies in the coupling with **q** =Q′ (middle between Γ- and K′-point) phonons, but no **q** =Q phonons. (c) Phonon modes resolved contribution to the linewidth at T= 4 K and 300 K normalized by the total width at each temperature.

we find a chiral dependence of the Γ-Q scattering process [240]. The bright exciton in K-valley can be scattered by the Q′-phonon but not Q-phonon (Q′ is the middle point between Γ and K′ to be distinguished from Q-point). This fact inherits from the single electron property; an electron at K-point can absorb a Q′-phonon and transits to Q-point easily, but the absorption of a Q-phonon will lead it to M-point which is forbidden by energy conservation. Last, we analyze the phonon mode dependence of the linewidth. Previous research has provided a detailed discussion on phonon mode at K-point by symmetry analysis [233], but knowledge regarding Q- and M-phonon is still missing. At low temperature, both acoustic and optical phonons have significant contribution with ratio, $\Gamma^{ac.}_{\text{width}}/\Gamma^{op.}_{\text{width}} \sim 0.6/0.4$. However, with temperature raised to room temperature, the acoustic phonons dominate the scattering processes.

We present the predicted PL spectrum at T= 15 K in Fig. 3.11(a) accompanied by the experimental data [241] with the PL frequency normalized to the bright exciton energy. The result shows that our prediction is ∼ 45 meV red shifted below the experiment PL, which is within the error of the band edge measurement $\Delta E_{KQ} \sim \pm 80$ meV. Fig. 3.11(b) presents great agreement between our prediction

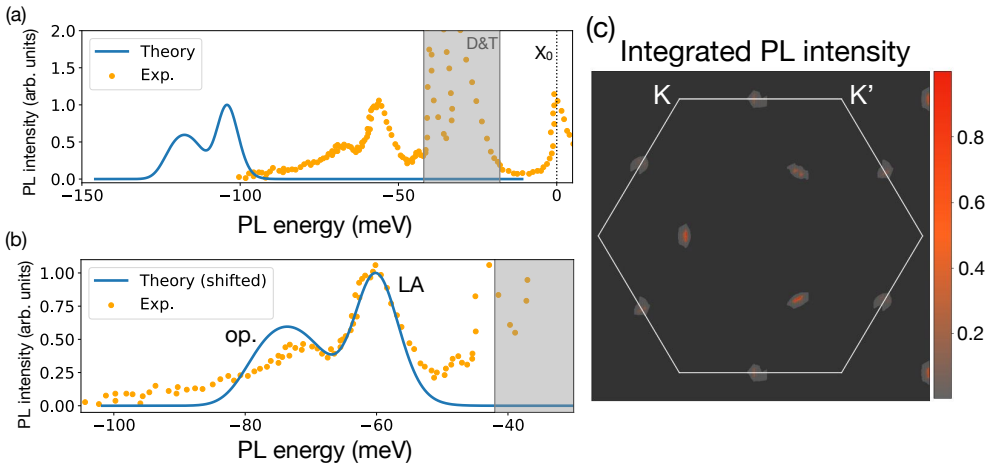

Figure 3.11: **Phonon-assisted photoluminescence in WSe_2.** (a) Raw theoretical prediction for PL signal at T= 15 K with bright exciton energy X_0 as reference zero point to compare with experimental data. Spectrum within E= $-40 \sim -20$ correspond to the emission from dark exciton and trion (D&T). (b) The predicted spectrum is shifted to match its peak with the experimental data. (c) Exciton momentum-resolved contribution to the integrated PL intensity. The main contribution lies in the Q′-valley.

and experimental result after we match the main PL peak. Further, our calculation also shows that the main peak is the result of longitudinal phonon emission while the sideband is the collective contribution from optical phonon emission. We also analyze the PL source, by leaving out the momentum integration but integrating the PL intensity in Eq. (3.45). The momentum resolved PL is presented in Fig. 3.11(c) which shows the $\mathbf{Q}$ =Q′ excitons have the main contribution while the $\mathbf{Q}$ =M excitons are the secondary resources. This is a result of the exciton spin structure; the lowest exciton eigenstate at $\mathbf{Q}$ =Q′ is spin-singlet but is spin-triplet at $\mathbf{Q}$ =M.

Exciton Depolarization in WSe_2

The phonon effect in exciton depolarization is generally ignored in previous treatments due to the spin-valley locking property and low spin-flipping phonon scattering in TMDs [43, 233]. However, a recent study [242] shows a significant contribution in intravally spin-flipping from *e*-ph coupling, which challenges this well adopted assumption. As a result, here we present a general discussion on phonon effect in exciton depolarization. Based on the BSE solution, exciton in K- and K′-valley are degenerate and orthogonal quantum states, independently evolving with time, while the interaction with phonon can mixing them. In general, the tran-

sition between a degenerate pair can be realized in quantum correction. As shown in Fig. 3.12(a), a particle in n_1 can emit(absorb) a phonon and re-absorb(emit) it, and transit into the other state n_2. While the initial state is the same as final state, $n_1 = n_2$, this process becomes the self-energy correction [225]. Focusing on these two states, we can write an effective 2×2 Hamiltonian:

$$H = H_0 + H_{\text{1-loop}} = \begin{pmatrix} E + \Sigma_{11} & \Sigma_{12} \\ \Sigma_{21} & E + \Sigma_{22} \end{pmatrix} \tag{3.48}$$

where E is the degenerate energy and the amplitude of the correction follows :

$$\begin{aligned} \Sigma_{n_1 n_2}(i\omega_b, \mathbf{Q} = 0) = \frac{-1}{\mathcal{N}_\mathbf{q}} \sum_{m\mathbf{q}\nu} \mathcal{G}_{n_1 m\nu}(0, \mathbf{q}) \cdot \mathcal{G}^*_{n_2 m\nu}(0, \mathbf{q}) \\ \left[\left(N_{\nu\mathbf{q}} - F_{m\mathbf{q}}\right) \times \left(\frac{1}{E_{m,\mathbf{q}} - E_{\nu,\mathbf{q}} - i\omega_b} - \frac{1}{-E_{m,\mathbf{q}} + E_{\nu,\mathbf{q}} - i\omega_b} \right) \right. \\ \left. - \left(N_{\nu\mathbf{q}} + 1 + F_{m\mathbf{q}}\right) \times \left(\frac{1}{-E_{m,\mathbf{q}} - E_{\nu,\mathbf{q}} - i\omega_b} - \frac{1}{+E_{m,\mathbf{q}} + E_{\nu,\mathbf{q}} - i\omega_b} \right) \right], \end{aligned} \tag{3.49}$$

where analytical continuation will take the complex parameter $i\omega_b$ back to the real energy axis by $i\omega_b = E$. Applying Eq. (3.49) to the WSe_2 bright exciton pair, numerical result provides an extremely weak transition amplitude Σ_{12} of μeV which is below our numerical accuracy. This vanishing amplitude indeed supports the argument to overlook the phonon contribution. However, a detailed analysis shows a delicate cancellation among the complex number $g_1 \cdot g_2^*$ in Eq. (3.49). On the other hand, if we replace $g_1 \cdot g_2^*$ by its absolute value $|g_1 \cdot g_2^*|$, we can obtain a transition amplitude of order of meV. Note that the summation of complex number is of nature of quantum mechanical superposition while, in classical procedure, the possibility is summed as real number. As a result, we propose that the exciton depolarization via phonon effect is forbidden in the quantum level but allowed in the classical process. To this end, we apply the classical Boltzmann Transport Equation (BTE) and make a real-time (RT) simulation of the bright exciton relaxation process to examine the depolarization effect which is schematically presented in Fig. 3.12(b). We applied the RT-BTE formula [62]:

$$\begin{aligned} \left(\frac{\partial F_{n\mathbf{Q}}}{\partial t}\right)^{\text{ex-ph}} = -\frac{2\pi}{\hbar} \frac{1}{\mathcal{N}_\mathbf{q}} \sum_{m\nu\mathbf{q}} |\mathcal{G}_{nm\nu}(\mathbf{Q}, \mathbf{q})|^2 \\ \times \left[\delta\left(E_{n\mathbf{Q}} - E_{m\mathbf{Q}+\mathbf{q}} + \hbar\omega_{\nu\mathbf{q}}\right) \cdot F_{\text{abs}}(t) + \delta\left(E_{n\mathbf{Q}} - E_{m\mathbf{Q}+\mathbf{q}} - \hbar\omega_{\nu\mathbf{q}}\right) \cdot F_{\text{em}}(t) \right], \end{aligned} \tag{3.50}$$

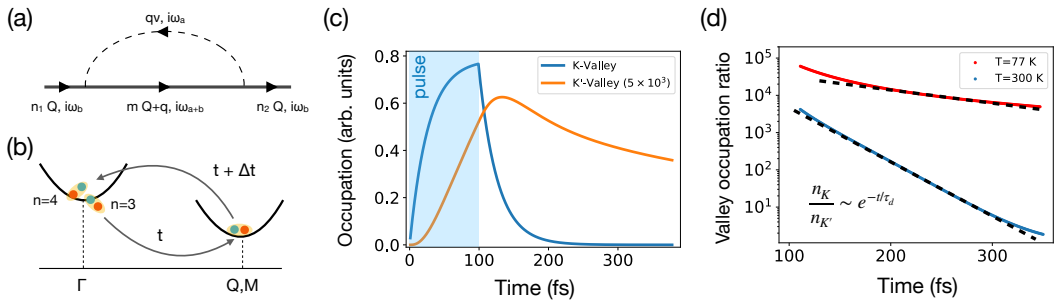

Figure 3.12: **Exciton depolarization in WSe_2 from BTE.** Realtime valley depolariztion at T=300 K. (a) Exciton occupation number in K/K′-valley respectively. (b) Occupation ratio between K/K′-valley after the illumination of circularly polarized lights. This corresponding depolarization time is $\tau_d = 29.8$ fs at 300 K and $\tau_d = 104.1$ fs at 77 K .

where $F_{\text{abs}}(t)$ and $F_{\text{em}}(t)$ are occupation factors for absorption and emission process:

$$F_{\text{abs}} = F_{n\mathbf{Q}} N_{\nu\mathbf{q}} (1 + F_{n\mathbf{Q+q}}) - (1 + F_{n\mathbf{Q}})(1 + N_{\nu\mathbf{q}}) F_{n\mathbf{Q+q}} \tag{3.51a}$$

$$F_{\text{em}} = F_{n\mathbf{Q}} (1 + N_{\nu\mathbf{q}})(1 + F_{n\mathbf{Q+q}}) - (1 + F_{n\mathbf{Q}}) N_{\nu\mathbf{q}} F_{n\mathbf{Q+q}}. \tag{3.51b}$$

where we suppress the time dependence for both F and N. In the absorption process, Eq. (3.51a), the first term means that there is no scattering when there is no exciton or no phonon ($F_{n\mathbf{Q}} = 0$ or $N_{\nu\mathbf{q}} = 0$), while for the emission, Eq. (3.51b), its first term requires non-zero exciton occupation to realize the process but not for phonons. For both scattering channels, the second terms are the time reversal process of their first term, respectively. The $(1 + F)$ structure reflects the bonsonic property of exciton which is $(1 - f)$ for e-ph scattering where f is the electron (fermion) occupation number [62]. We present the simulation with steady incident circularly polarized light for first 100 fs. During the process, we assume the phonon to be in thermal equilibrium with environment and kept at T= 300 K, satisfying the Bose-Einstein distribution. The evolution of exciton in K/K′-valley is presented as a function of time in Fig. 3.12(c). The K-valley exciton fastly increase in first 50 fs and gradually saturates near the end of the incident pulse. Once the pulse turned off after 100 fs, the occupation number immediately drops exponentially. On the other hand, the K′-valley exciton keeps increasing for 30 fs even after the incident pulse stops and decreases very slow (−30% in 250 fs) afterwards. We define the exciton depolarization by fitting the ratio of the occupation number between two valleys with:

$$\frac{n_{\text{K}}}{n_{\text{K'}}} = A e^{-(t-t_0)/\tau_d}, \tag{3.52}$$

where A and t_0 are constants depending on the simulation setting, such as pulse strength and pulse duration, and the time constant τ_d is the intrinsic depolarization time scale (Fig. 3.12(d)). Fitting data within 150 fs $\sim$ 300 fs, we obtain that the exciton depolarization time scale at T=300 K is about $\tau_d = 29.8$ fs, such that, 250 fs after the end of the pulse, excitons almost equally occupy the K/K′-valley. We also present a calculation at T= 77 K and obtain a $\tau_d = 104.1$ fs depolarization time. This result is consistent with the fact that the bright exciton relaxation time is about three short at 300 K compared to the time at 77 K.

3.4 Joint Study on Exciton-Phonon Relaxation in Monolayer Tungsten Diselenide

Optical measurements employed in excitonic research or discussed in previous section are limited to capture the electron-hole with zero-momentum transfer without spin-flipping while shading light only partially on finite-momentum exciton and spin-triplet pairing indirectly via ex-ph coupling. Directly probing the drak exciton, on the other hand, is achieved by the time- and angle-resolved photoemission spectroscopy (trARPES) which measures the energy-momentum distribution of photoemitted electrons in non-equilibrium systems on ultrafast timescales [243–245]. However, a corresponding theoretical description for dark exciton behavior is still missing which requires the knowledge of exciton-phonon interaction.

In this section, we present a joint research with experimental collaborators, Professor Ralph Ernstorfer and graduate student Shuo Dong in Max Planck Institute in Berlin, on exciton real-time formation and relaxation in monolayer WSe_2, by combining their trARPES technique and our first-principle ex-ph formalism. Our results identify the electron relaxation from K-valley to Q-valley under the correlation within an exciton and obtain a characteristic delay time of ~100 fs. Our theoretical analysis on ex-ph scattering map in full BZ suggests new path way that wasn't captured in former approaches which considered only K-K′ inter-valley transitions. Before closing the discussion, we provide predictions on energy-resolved ARPES spectrum for future validation which is not currently accessible due to the limited resolution in energy domain of instruments currently equipped.

Exciton band structure

As emphasized in Sect. 3.3, the question of whether the monolayer WSe_2 of direct gap or indirect gap is still under debating, and critically depends on the synthesis method.

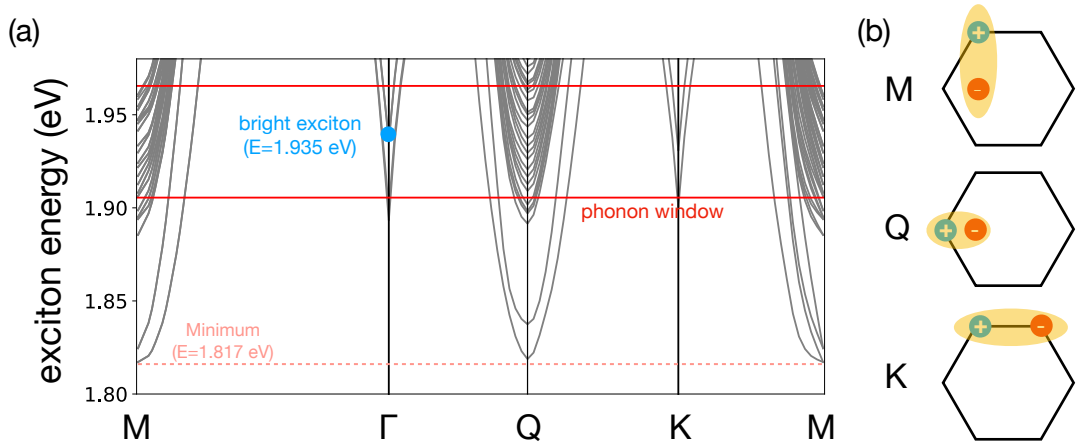

Figure 3.13: **Exciton band structure in monolayer WSe_2.** (a) Exciton energy-momentum relations (band structure) along chosen symmetry line. Global minimum (E_{min} = 1.817 eV) locate at M and Q points corresponding to indirect band gap transition between electron valance band maximum at K-point and conduction band minimum at Q-point. Lowest bright excitons are the n = 3,4 excitation at Γ-point with energy $E_{3,4,\Gamma}$ = 1.935 eV. Given phonon energy ~30 meV, the relaxation window for bright exciton is presented by horizontal red lines. (b) The independent particle picture for electron-hole pairing in Brillouin zone of excitons at high symmetry points: M, Q, and K.

Provided with our preliminary on bright exciton scattering path, the photo-excited Γ-exciton will be scattered mainly by M-phonon and Q-phonon (See Fig. 3.10) which corresponds to the scattering of electron from K-valley to Q-valley. As a result, the relative energy alignment between the local minimum at K- and Q-point in the conduction band plays a central rule in the early stage of the exciton relaxation process.

In this study, we adopt the band edge offset from our experiment collaborators, $\Delta E_{KQ} = E_K - E_Q$ = 118 meV. Solving the BSE[5], Eq. (1.9), for all **Q**−points in the BZ, we obtain the exciton eigenenergy and exciton wave function to study the dynamics. We present the resultant exciton energies in Fig. 3.13(a) and highlight the location of the lowest bright exciton at 1.935 eV. Multiple minima are found locating at high symmetry points. The global minima are the spin-singlet exciton with momentum **Q** = Q and the spin-triplet exciton with momentum **Q** = M with energy E_{min} = 1.817 eV, while the later is generally missed in the previous approach. For later discussion, given phonon frequency ~7 THz in WSe_2, we also specify

[5]The detailed computational information and a discussion on substrate effect can be found in Appendix I.

the bright exciton relaxation window at $E_{bright} \pm 30$ meV. The window shows that the available phase space in excitonic Q- and M-valley for bright exciton relaxation can be reduced by 50% once the bright exciton energy is lowered by 30 meV, reflecting the strong dependence of relaxation time on the energy offset ΔE_{KQ}. In Fig. 3.13(b), we show the relative position of electron-hole pair in the BZ for chosen exciton momentum. Note that since the highest valance band has only maximum at K/K′ points and has larger curvature than the lowest conduction band, the hole is less mobile than the electron and tends to stay in the K/K′ corner.

Ultrafast exciton relaxation and trARPES

The trARPES, like the standard ARPES, measures the electronic state, including energy and momentum, by XUV-photon probing but with additional power on time-resolution. The multidimensional signal $I(\mathbf{k}, \omega; t)$ is the product of electron occupation $n_a(\mathbf{k}; t)$ in a quasi-particle state $|a, \mathbf{k}\rangle$ at time t and corresponding spectral function $A_a(\mathbf{k}, \omega)$. Thus, provided with the normalization of the spectral function $\int d\omega A_a(\mathbf{k}, \omega) = 1$, the integration of trARPES intensity along energy domain can produce the electron occupation at each time step in the momentum space and reveal the electron re-distribution during carrier relaxation.

To simulate the exciton relaxation process, we apply the RT-BTE formula, Eq. (3.50) at room-emperature, 300K, in monolayer WSe_2, with a Gaussian pumping of 55 fs full width at half maximum (FWHM) acting equally on the K/K′-valley corresponding to the linearly polarized incident pulse employed in the experiment setting. With the time-evolution of the exciton occupation number, the corresponding ARPES signal can be obtained by [246]:

$$I(k, \omega; t) \propto \mathrm{Im}\left\{\sum_{m\mathbf{Q}} F_{m\mathbf{Q}}(t) \sum_{cv} \frac{|A^{m\mathbf{Q}}_{vc\mathbf{k}}|^2}{\omega - (E_{m\mathbf{Q}} + \epsilon_{v\mathbf{Q}-\mathbf{k}}) + i\eta}\right\}, \tag{3.53}$$

where $F_{m\mathbf{Q}}(t)$ is the exciton occupation from the RT-BTE result in the m-th exciton state with energy-momentum $(E_{m\mathbf{Q}}, \mathbf{Q})$ and $|A^{m\mathbf{Q}}_{cv\mathbf{k}}|^2$ is the probability to find the electron in the exciton state $(m, \mathbf{Q})$ with energy $E_{m\mathbf{Q}}$ above the hole energy $\epsilon_{v\mathbf{Q}-\mathbf{k}}$. η is the line width broadening, for which we set as a constant value temporally but can be determined by the line width calculation presented in Sect. 3.3. In Fig. 3.14, we demonstrate few snap shots of our results of real-time exciton relaxation simulation and the corresponding ARPES prediction. In the left side of Fig. 3.14, we use the size of the circle to represent the occupation along with the exciton band structure in the main panel, and the energy resolved and momentum resolved occupation are

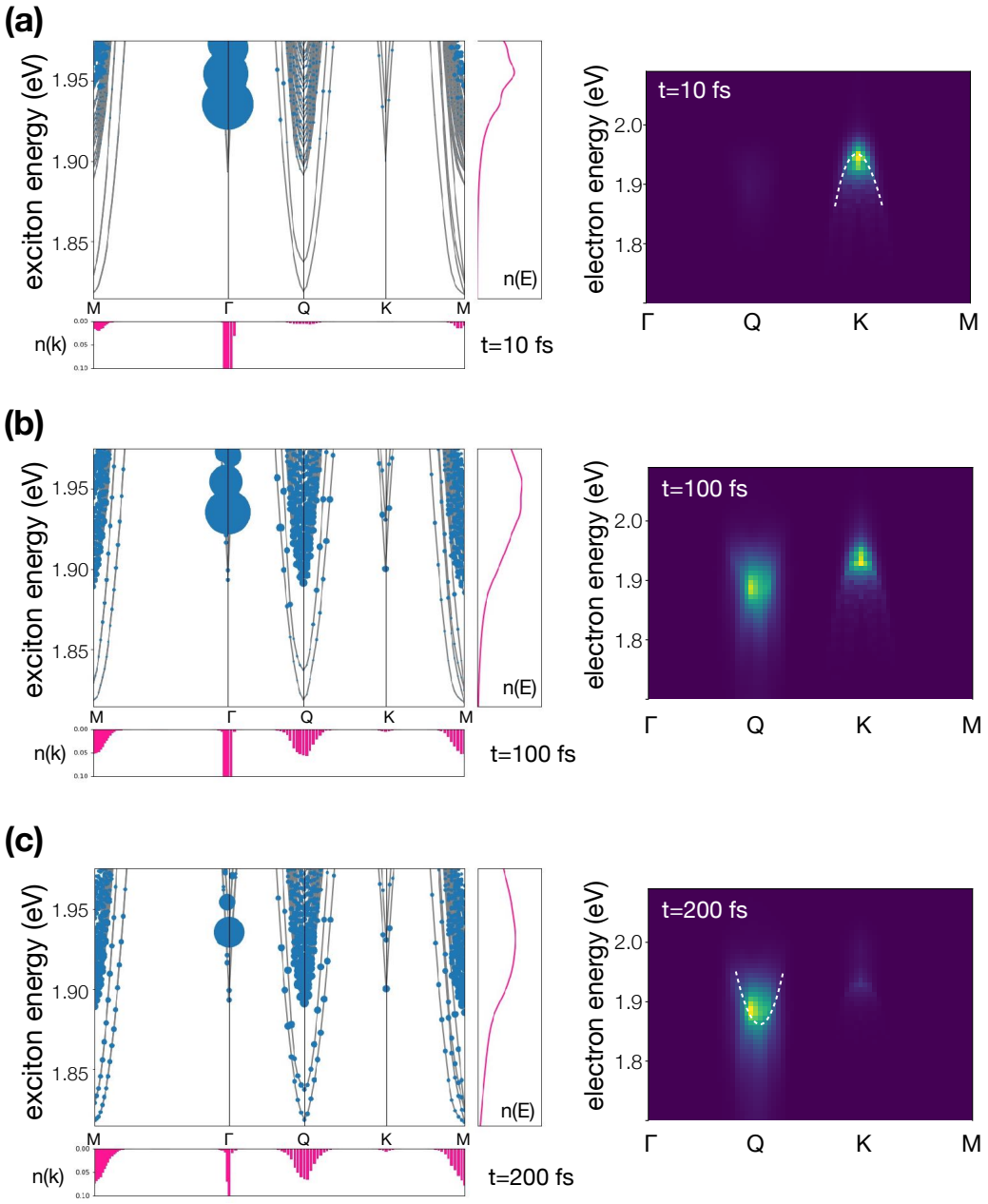

Figure 3.14: **Snap shot of exciton relaxation process and predicted ARPES.** For all panel, left panel is the energy-momentum resolved exciton distribution, and the right panel the the corresponding APRES signal. (a) At the peak time of the pumping pulse, t=10 fs, excitons mainly locating in the Γ-valley. In ARPES, the hot spot locating at the K point reflects the K-K electron-hole transition of the bright exciton. (b) At t=100 fs, excitons occupy in all Γ-, Q-, and M-valleys, but merely in K-valley. Signal at Q-valley is appearing in ARPES. (c) At t=200 fs, most of excitons have left Γ-valley with only few in the buttom of bright state. ARPES spot in K-point disappears, and signal in Q-point dominates the spectrum.

shown in the right and bottom panel respectively. In the right side of Fig. 3.14, the ARPES spectrum along the high symmetry line Γ-Q-K-M is presented. Fig. 3.14(a) shows the exciton distribution during the pumping stage within which t=10 fs is the time when the Gaussian pulse meets its maximum. In this early stage, as our design, most exciton are residing in the Γ-valley above the optical gap of E=1.935 eV. Besides, a minor portion of excited excitons have already been scattered. Among them, the dominant scattered final states are those in M-valley above 1.95 eV which results from the M-phonon absorption of the exicted Γ-excitons. In contrast to M-phonon, the emission/absorption ratio is more balanced for Γ-exciton-Q-phonon interaction which is generally weak. By applying Eq. (3.53), we can convert the exciton occupation into the electronic spectrum. The result shows a single hot spot located at the K-point which corresponds to the direct gap excitation of K-K electron-hole pairs. Compared to previous study of excitonic ARPES [220], we can obtained the downward parabolic shape as the shadow imagine of valance band even with only incoherent excitons due to the superposition of electron-hole vertical transition of **k**-points near the K-valley extreme in the bright exciton wave function. After the pumping stops and excitons relax for $\sim$ 100 fs (see Fig. 3.14(b)), excitons occupy all Γ-, Q-, and M-valleys, while, provided with narrow density of states, the excitonic K-valley merely plays a role in the exciton relaxation process. The growing exciton occupation in Q- and M-valley result in the appearance of signal at Q-point in the ARPES; since the hole is robustly concentrating in the K-valley, electron in Q-exciton and M-exciton mainly sit in the electronic Q-valley as shown in Fig. 3.13(b). When time reaches t=200 fs (see Fig. 3.14(c)), only a small number of excitons remains in Γ-valley occupying the bottom of bright exciton state which are the relic of the pumped excitons. Therefore, in the ARPES spectrum, no significant signal shows at the K-point any more, and Q-point spot dominates. The Q-point spot comes from the high exciton occupation number in the bottom of continuous band in Q- and M-valley with energy $\sim$1.90 eV. With a detailed analysis of the shape of the spot[6], a upward parabola can be obtained which corresponds to the exciton band dispersion.

So far, we have provided an elaborate discussion on the energy-momentum resolved ARPES spectrum. However, it's challenging in experiment setup to access the fine structure due to the limited energy resolution. Thus, in this collaboration, we focus on the relaxation in the momentum space by studying the momentum-resolved

[6] We present the same data in log-scale in Appendix J

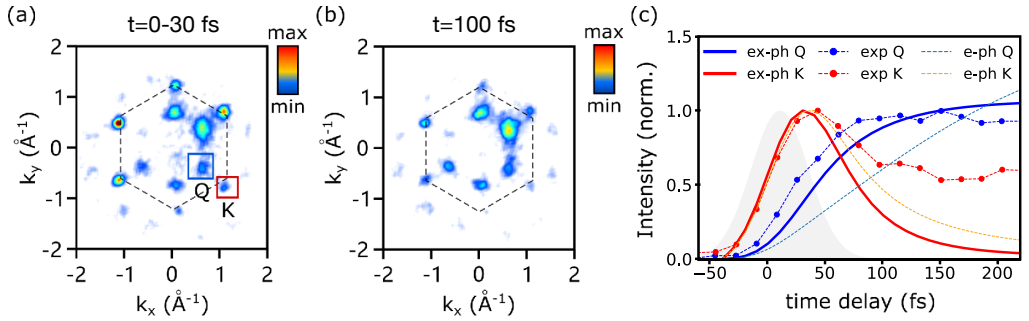

Figure 3.15: **Momentum-resolved intervalley carrier dynamics.** (a) By integrating the first 30 fs, the transient momentum map $I(k_x, k_y)$ shows the excited-state carriers distribution in the first Brillouin zone (dash hexagonal labelled) , including the K and Q valleys. (b) The hot carrier distribution at t=100 fs. (c) The electron population time traces at K (red) and Q valley (blue) from experimental data (dotted lines) and the ab initio calculated within ex-ph scheme (solid lines), within independent e-ph scheme (dashed line). The gray region represents the 55 FWHM Gaussian pulse.

intensity:

$$I(\mathbf{k};t) \propto \sum_{m\mathbf{Q}} F_{m\mathbf{Q}}(t) \sum_{cv} |A^{n\mathbf{Q}}_{cv\mathbf{k}}|^2. \tag{3.54}$$

We show the result from both experiment and numerical simulation in Fig. 3.15. Fig. 3.15(ab) presents the integrated intensity observed in the first 30 fs and the snapshot at 100 fs in momentum space. In the early stage, hot spots located at the corner of the hexagonal BZ are the optical pumped bright exciton. Strength in K- and K′-valley are approximately the same, but 3-fold symmetry is lacking since the pumping pulse is not vertical to the WSe_2 crystal. After ~70 fs, the excited electrons relax from K-valley to Q-valley due to the phonon scattering which corresponds to the Γ-M and Γ-Q relaxation in the exciton picture. We contrast the experimental data and the computed result in Fig. 3.15(c) and obtain great agreement on the delay time of the Q-valley occupation saturation within 10 fs. However, the discrepancy is significant in the K-valley occupation after they reach a stationary state (200 fs after the pulse). Rather, by fitting the decay trend from 50 fs to 200 fs with simple exponent up to a rigid shift, we can obtain:

$$n^K_{\text{exp}}(t) = e^{-(t-15)/43.0} + 0.54 \tag{3.55}$$

$$n^K_{\text{theo.}}(t) = e^{-(t-50)/43.0} + 0.00 \tag{3.56}$$

with the same characteristic decay time scale of 43 fs. Thus, we attribute the inaccuracy to the uncertainty in the band edge offset which is critical to the electron

distribution in thermal equilibrium but not from the dynamics. In addition, we also carry out the relaxation with only e-ph interaction but no excitonic effect, as shown together in Fig. 3.15(c). The comparison between the two approaches, ex-ph and e-ph, shows how electron-hole attraction corrects the relaxation process; although the decay in K-valley is fastened a little under the modulation from holes, the Q-valley occupation can't reach saturation even after 200 fs without them.

For detailed ex-ph dynamics, we demonstrate the exciton relaxation channel for excitons in each valley in Fig. 3.16 which presents the scattering processes in cartoon plots from both excitonic picture and electronic picture, accompanied with a color map showing the coupling strength. Fig. 3.16(a) shows that the singlet (bright) Γ-exciton couples mainly to the M-phonon and Q-phonon which scatters the exciton into the corresponding M- and Q- valley. In terms of electronic picture, this scattering channel corresponds to the scattering of K-electron into different Q- and Q′-valley. Compared with the scattering mapping in Fig. 3.10, we retain a six-fold symmetry for Q-phonon interaction, since the bright exciton is excited with linearly polarized incident light and occupying in K/K′-valley equally here. In Fig. 3.16(b), the M-exciton couples mainly with Γ-phonon such that the intra-valley scattering domains the M-exciton relaxation. Besides, the M-exciton also couples to M-phonon and is scattered into the other two inequivalent M-valleys, which corresponds to the electron scattering among Q′-valley in electronic picture. Last, for Q-exciton in Fig. 3.16(c), intra-valley is also the strongest scattering path, and its interaction with M-phonon will create inter-Q-valley scattering in both excitonic picture and electronic picture.

3.5 Conclusion

Ab initio method combining GW-BSE and perturbation theory to compute the interaction between excitons and phonons is carried out in this study which shows the ex-ph coupling can be viewed as a superposition of independent electron-phonon scattering processes and hole-phonon scattering processes. Based on the theory, we for the first time implement a fully parameter-free algorithm to investigate exciton dynamics. The numerical approach merges state-of-the-art algorithms from the exciton community (YAMBO) and the transport community (PERTURBO).

Equipped with the methodology, we shed lights on ex-ph phenomena in bulk h-BN and monolayer WSe_2, including ex-ph relaxation time, phonon-assisted PL, photon-emission line width broadening, and exciton depolarization effect. Our

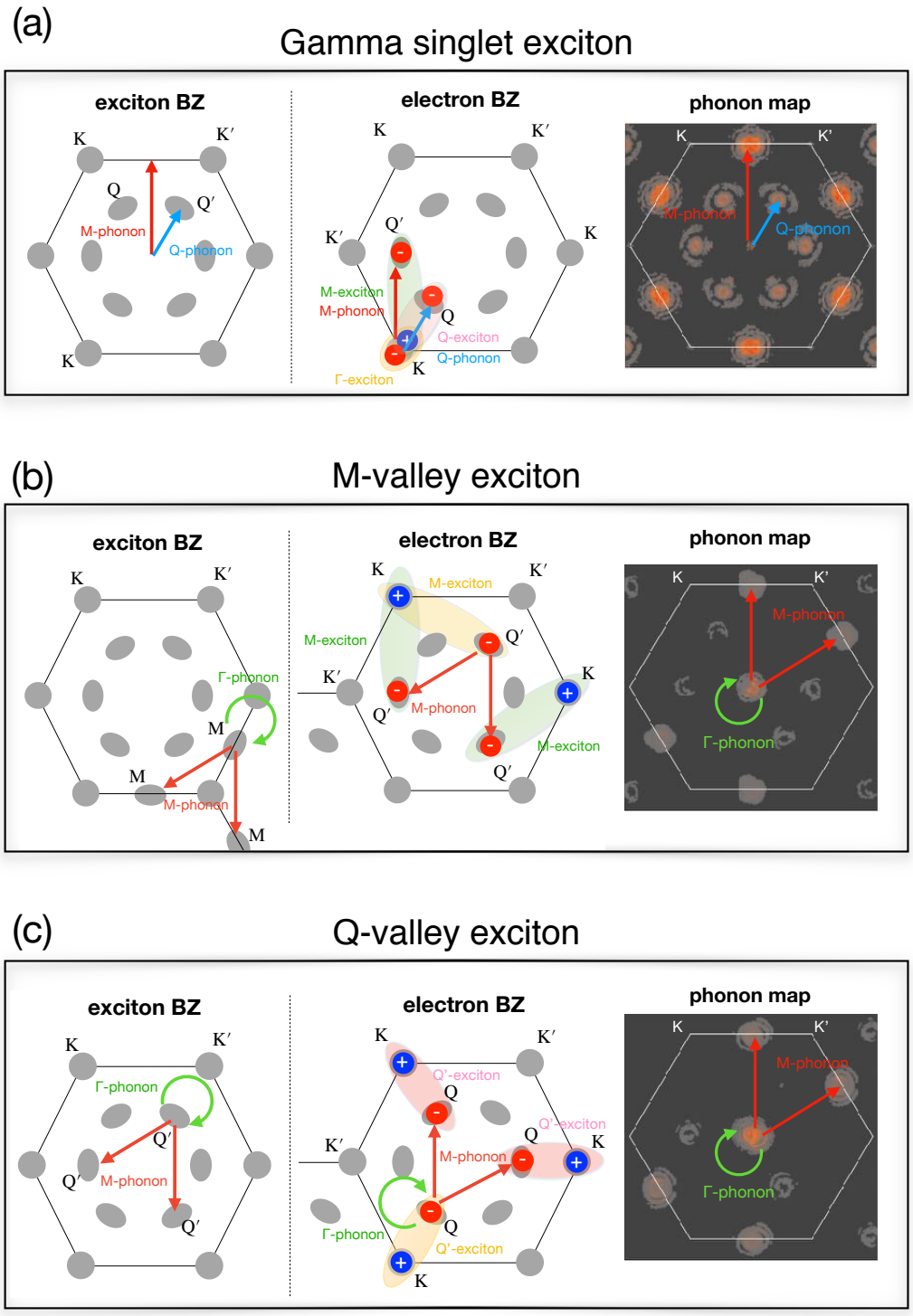

Figure 3.16: **Exciton scattering map in WSe_2**

calculations in h-BN reveal the dominant ex-ph coupling with the LO mode, identify the threshold for LO phonon emission and the associated LO emission time, and unravel the momentum, energy and temperature dependence of ex-ph scattering processes. Our studies on ex-ph effect in monolayer WSe_2 accurately reproduce the temperature dependence of bright exciton linewidth, phonon-assisted PL signal and provide a prediction on exciton valley depolarization time scale. The analysis of the linewidth shows a chiral dependence in K-valley exciton scattering channel and reveals the dominant role of LA-phonon. Our calculation of PL identifies the source of the light signal in both phonon and exciton sectors; the main peak comes from the light emission of Q′-exciton with the assistance of LA-phonon while electron-hole radiative recombination during the optical phonon emission creates a weaker but broader side band. For the exciton depolarization, our BTE simulation predicts a femtosecond characteristic time at room-temperature which was ignored in previous treatments.

In the joint study with experiment group, we investigate the exciton real-time relaxation in monolayer WSe_2. The result from RT-BTE calculation traces the exciton redistribution in the energy-momentum space which highlights the strong M-phonon absorption in the early pumping stage and the following dissipation from Γ-valley into Q- and M-valley. Based on the numerical data, we convert the time-resolved exciton occupation into electronic spectrum that can be obtained by trARPES technique. Reducing the multidimensional information down to momentum domain, our prediction of the electron relaxation from K-valley to Q-valley under the modulation of excitonic effect perfectly matches the observation conducted by our collaborators. In addition, we provide a detailed analysis on the ex-ph scattering channel for excitons in Γ−, Q-, and M-valley. The key finding is the dominant intra-valley scattering of Q- and M-exciton over the inter-valley scattering which quantifies the stability of Q-, M-valley degree of freedom under the ex-ph interaction.

Overall, our approach presented in this chapter paves the way to quantitative studies of exciton transport and ultrafast dynamics in materials with strongly bound excitons and provides novel insight into exciton evolution and light emission under the influence of phonon effect. It benefits future investigations on exciton non-radiative behaviors and studies in the strong correlated system where electron-hole-lattice are coupled under equal footing. On the other hand, the special discussion on TMDs deepens our understanding of the robustness of valley degree of freedom and provides a guideline in future valleytronic design.

Chapter 4

CONCLUSION AND FUTURE DIRECTIONS

Over the past decades after proposal by Frenkel in 1931, exciton has now been a central research subject in the field of condensed matter system and semiconductor physics, with the importance growing even faster along with the advance in modern material design and synthesis technique. Each step of the development replies on the support and guidance from corresponding theoretical studies. Currently, the progress is slowed down by the lack of knowledge on the interaction between exciton and uncontrolled environment. Thus, this thesis provides numerical approaches, shedding lights on the underlying mechanism in exciton intrinsic radiative recombination and non-radiative ex-ph scattering.

For exciton radiative behavior, our work establishes a general framework to study the exciton radiative lifetimes from first-principle. We review existing and derive new formalism for excitons in 0D, 1D, 2D, and 3D nanostructures. The use of GW-BSE approach correctly includes the electron-hole attraction on the top of independent particle picture based on DFT. The analytic result shows a strong correlation between the temperature trend of effective lifetimes and the system dimension by a power-law due to the different phase space occupied in thermal equilibrium. The study of different dimensionalities further points out the usage of incorrect prefactors in the formula adopted by early literature when discussing low-dimensional materials. These discussions are then supported by our numerical benchmark calculations in gas molecules and bulk GaAs. The methodology developed enables quantitative research based on the exciton radiative decay, and here we carry out several pioneer works. First, we analyze the excitonic transition dipole in monolayer TMDs and reformulate the radiative lifetime equation in 2D system into light emission rate as a function of emission angle. The numerical calculation predicts an anisotropic PL pattern from exciton recombination in TMD as a result of superposition of bright exciton state in inequivalent K/K′ valley in BZ. Second, we use the exciton energy and radiative lifetimes to identify the potential atomic structure of defects in monolayer h-BN and conclude the most probable one to be the nitrogen vacancy plus a carbon replacement at boron site. For the third application, we study the exciton radiative lifetimes in bulk GaN. The inconsistency between our calculation and experiment data raises the importance of considering the exciton dissociation

effect which corrects the deviation after it is included. Taken together, the GW-BSE scheme for exciton radiative lifetime presented in this thesis constitutes the cornerstone of study regarding the light-matter interaction in novel materials and advance the optical nanotechnology. Applications beyond the cases we work out in Chapter 2 are vast. Examples like organic crystal and Perovskites are also emerging material for optoelectronic devices with strong excitonic effect to be explored. On the other hand, exciton in heterostructures, such as the indirect exciton in bilayer-TMD, with their electron-hole spatially separated, can possess much longer lifetime than monolayer. These excitons are of more interests from the perspective of quantum engineering and urge for individual investigation. In summary, the access to the exciton radiative lifetime helps us to isolate the intrinsic quantities from external effects and provides the guideline for future design in optoelectronic and photovoltaic technology.

For ex-ph interaction, our methodology combines the GW-BSE method and the first order perturbation theory to compute the ex-ph matrix element. Our derivation shows that the ex-ph scattering process can be viewed as a quantum superposition of independent electron-phonon scattering and hole-phonon scattering weighted by exciton coefficients. This idea was adopted as a makeshift in literature but a rigorous proof was merely found. The key achievement demonstrated in this thesis is that we for the first time implement the computation routine by interfacing the mainstream DFT and BSE algorithms. This breakthrough enables the *ab initio* simulation for all phenomenon from ex-ph dynamics. In this work, the scheme is mainly applied on two excitonic systems, bulk h-BN and monolayer WSe_2, with stable exciton state in room-temperature of $\gtrsim 200$ meV binding energy. Our study in bulk h-BN reveals the strong exction coupling with the optical phonon which was a general feature for charged carriers in polar materials but never shown for neutral excitation. This fact results in the relaxation rate drop for exciton with energy below the LO-phonon emission threshold and the two dominant peaks in the phonon-assisted PL spectrum from optical phonon emission. The study on the WSe_2 discusses the homogeneous linewidth broadening of the bright exciton, phonon-assisted PL. The success of reproducing the experiment data is the first achievement of using fully first-principle method to study ex-ph phenomenon in material with strong SOC. We further investigate the exciton depolarization effect in WSe_2. Our result points out that ex-ph coupling can't cause the inter-K/K′ valley scattering in pure quantum process, but semi-classically. We apply the BTE and implement corresponding algorithm to time step the occupation ratio in K/K′ valley

and determine a depolarization time scale of $\lesssim 100$ fs which was ignored in previous treatment. This thesis closes with a joint collaboration with experiment group on exciton relaxation in monolayer WSe_2. The result highlights the fast electron scattering between K- and Q-valley which dominates the electron relaxation process. The comparison between simulations with and without exciton effect emphasizes the important role of hole playing during the electron-phonon scattering which were considered non-interacting in early study. From the simulation, we also provide prediction on the ARPES signal for the first hundreds of femtosecond after the pumping, left for future validation. Further studies are under discussion but not included in this thesis. For instance, provided with the ability to access exciton occupation in ultrafast timescale, our machinery enables us to study the time-depending properties during the exciton formation while a collaboration is on-going on investigating the transient absorption in h-BN. Additionally, the exciton transport in monolayer TMD under thermal gradient is found to exhibit the exciton hall effect for which opposite drift direction is found for exciton in different K/K′ valley. This study requires the involving of the topological features in current framework and is important for studies in topological materials. On the whole, this work constitutes the theoretical basis to study the ex-ph scattering dynamics and grants us a tool to quantify the non-radiative observables, which never exists before. In addition, applications carried out in Chapter 3 provide microscopic insights of exciton relaxation processes in terms of physical quantities including, temperature, momentum, energy and lattice vibration modes.

On top on this thesis, some improvement can make the framework more complete. For example, current GW-BSE method and following ex-ph discussion are implemented on regular grid for which the computation cost increases as n_k^2 on the grid with n_k-points. However, in general, $O(100)$ points for each extended dimension is required for real-time BTE simulation, but During the study, we meet a resource limit when $72 \times 72 \times 1$-gird is applied for monolayer WSe_2 and use unphysical trilinear interpolation to convert to fine grid. Thus, we call for future study on interpolation scheme, like Wannier interpolation, for GW-BSE and ex-ph to reduce the computation cost and enable calculation on materials like organic crystal and perovskites. Other refinements of the work, like program optimization, are undergoing when the algorithm is being merged into the PERTURBO code.

Beyond the scope of this work, some extension are expected and deserved to be explored. In this thesis, we mainly focus on the clean semiconducting crystal with

low exciton density and no free carrier such that fruitful interaction are neglected. When the target material is doped or gated, excitons can further bind with charge carriers and form trions. The study of trion dynamics and radiative decay should be able to explain the full spectrum in the PL signal. On the other hand, when exciton density is high enough over a critical point, exciton condensation will occur accompanied with crystal deformation for which the ex-ph coupling will be a central ingredient to compute the critical temperature of the phase transition.

In conclusion, the new ideas, approaches, and findings provided in this thesis expand human understanding of exciton physics and grant the future nanotechnology a theoretical foothold to advance in optoelectronics and photovoltaics.

Appendix A

SECOND QUANTIZATION OF LIGHT IN ANISOTROPIC MATERIALS

Starting from Maxwell's equations in a material:

$$\begin{aligned} \boldsymbol{\nabla}\cdot\mathbf{D} = 0\,, \qquad & \frac{\partial \mathbf{D}}{\partial t} = \boldsymbol{\nabla}\times\mathbf{H}\ ;\ \mathbf{D} = \epsilon_0\boldsymbol{\epsilon}_r\mathbf{E}\,, \\ \boldsymbol{\nabla}\cdot\mathbf{B} = 0\,, \qquad & -\frac{\partial \mathbf{B}}{\partial t} = \boldsymbol{\nabla}\times\mathbf{E}\ ;\ \mathbf{B} = \mu_0\mathbf{H}\,, \end{aligned} \tag{A.1}$$

where ϵ_0 is the vacuum permittivity and μ_0 the vacuum susceptibility, we define the vector potential $\mathbf{A}$ and the scalar potential Φ:

$$\mathbf{B} = \boldsymbol{\nabla}\times\mathbf{A},\ \ \mathbf{E} = -\boldsymbol{\nabla}\Phi - \frac{\partial \mathbf{A}}{\partial t}. \tag{A.2}$$

We adopt a generalized Coulomb gauge, in which:

$$\Phi = 0, \quad \boldsymbol{\nabla}\cdot(\epsilon_0\boldsymbol{\epsilon}_r\mathbf{E}) = 0\,, \tag{A.3}$$

and write the equation of motion for $\mathbf{A}$ as

$$-\mu_0\epsilon_0\boldsymbol{\epsilon}_r\frac{\partial^2\mathbf{A}}{\partial t^2} = \boldsymbol{\nabla}\times(\boldsymbol{\nabla}\times\mathbf{A}) = \boldsymbol{\nabla}(\boldsymbol{\nabla}\cdot\mathbf{A}) - \boldsymbol{\nabla}^2\mathbf{A}. \tag{A.4}$$

From Eq. (A.4), we construct the Lagrangian

$$\begin{aligned} \mathcal{L} &= \frac{1}{2}\int d\mathbf{r}\left[\epsilon_0\mathbf{E}^T(\mathbf{r})\boldsymbol{\epsilon}_r\mathbf{E}(\mathbf{r}) - \frac{\mathbf{B}(\mathbf{r})^2}{\mu_0}\right] \\ &= \frac{1}{2}\int d\mathbf{r}\left[\epsilon_0\dot{\mathbf{A}}^T(\mathbf{r})\boldsymbol{\epsilon}_r\dot{\mathbf{A}}(\mathbf{r}) - \frac{(\boldsymbol{\nabla}\times\mathbf{A})^2}{\mu_0}\right]. \end{aligned} \tag{A.5}$$

The conjugate momentum of the vector potential is

$$\boldsymbol{\Pi}(\mathbf{r}) = \frac{\delta\mathcal{L}}{\delta\dot{\mathbf{A}}(\mathbf{r})} = \epsilon_0\boldsymbol{\epsilon}_r\dot{\mathbf{A}}(\mathbf{r}), \tag{A.6}$$

and by performing a Legendre transformation, we write the Hamiltonian as

$$\mathcal{H} = \int d\mathbf{r}\,\boldsymbol{\Pi}\,\dot{\mathbf{A}} - \mathcal{L} = \frac{1}{2}\int d\mathbf{r}\left[\frac{\boldsymbol{\Pi}^T\boldsymbol{\epsilon}_r^{-1}\boldsymbol{\Pi}}{\epsilon_0} + \frac{(\boldsymbol{\nabla}\times\mathbf{A})^2}{\mu_0}\right]. \tag{A.7}$$

Note that the Hamiltonian for classical electromagnetic field in vacuum can be recovered by setting $\boldsymbol{\epsilon}_r = \mathbf{I}$.

To define the creation and annihilation operators for second quantization, we follow the standard procedure and expand the vector potential in terms of its eigenmodes, which are labeled by the index λ:

$$\mathbf{A}(\mathbf{r},t) = \sum_{\lambda} q_\lambda \mathbf{f}_\lambda(\mathbf{r}) e^{i\omega_\lambda t}, \tag{A.8}$$

where q_λ are constants representing the amplitudes and $\mathbf{f}_\lambda(\mathbf{r})$ satisfy

$$\omega_\lambda^2 \mu_0 \epsilon_0 \boldsymbol{\epsilon}_r \mathbf{f}_\lambda - \boldsymbol{\nabla} \times (\boldsymbol{\nabla} \times \mathbf{f}_\lambda) = 0. \tag{A.9}$$

Since ω_λ enters the equation as a square, both $+\omega_\lambda$ and $-\omega_\lambda$ can have the same $\mathbf{f}_\lambda$ solution. However, since the vector potential is always real, we need $\mathbf{A}^\dagger = \mathbf{A}$, so that for each $q_\lambda \mathbf{f}_\lambda(\mathbf{r}) e^{i\omega_\lambda t}$ in Eq. (A.8), there must exists a corresponding term $q'_\lambda \mathbf{f}'_\lambda(\mathbf{r}) e^{-i\omega_\lambda t}$ such that

$$q'_\lambda \mathbf{f}'_\lambda(\mathbf{r}) = q^*_\lambda \mathbf{f}^*_\lambda(\mathbf{r}). \tag{A.10}$$

For convenience, we label this part of the solution as $-\lambda$:

$$q'_\lambda \mathbf{f}'_\lambda(\mathbf{r}) e^{-i\omega_\lambda t} = q_{-\lambda} \mathbf{f}_{-\lambda}(\mathbf{r}) e^{i\omega_{-\lambda} t}. \tag{A.11}$$

To obtain an orthogonality condition for the solutions, we substitute $\mathbf{f}_\lambda(\mathbf{r}) = \frac{\sqrt{\boldsymbol{\epsilon}_r}^{-1}}{\sqrt{\mu_0\epsilon_0}} \mathbf{g}_\lambda(\mathbf{r})$ and get:

$$\omega_\lambda^2 \mathbf{g}_\lambda - \frac{\sqrt{\boldsymbol{\epsilon}_r}^{-1}}{\sqrt{\mu_0\epsilon_0}} \boldsymbol{\nabla} \times \left(\boldsymbol{\nabla} \times \frac{\sqrt{\boldsymbol{\epsilon}_r}^{-1}}{\sqrt{\mu_0\epsilon_0}} \mathbf{g}_\lambda \right) = 0. \tag{A.12}$$

Now with ω_λ^2 as the eigenvalue, $\mathbf{g}_\lambda$ are eigenfunctions of a Hermitian operator and form an orthogonal solution set:

$$\int d\mathbf{r}\ \mathbf{g}^\dagger_\lambda(\mathbf{r}) \cdot \mathbf{g}_{\lambda'}(\mathbf{r}) = \int d\mathbf{r}\ \mu_0\epsilon_0 \mathbf{f}^\dagger_\lambda(\mathbf{r}) \boldsymbol{\epsilon}_r \mathbf{f}_{\lambda'}(\mathbf{r}) = \delta_{\lambda,\lambda'}. \tag{A.13}$$

In the following, we take plane waves as our eigenmodes, and label them by their polarization and momentum by substituting $\lambda \to (\lambda, \mathbf{q})$, $-\lambda \to (-\lambda, -\mathbf{q})$. We also put

$$\mathbf{f}_{\lambda\mathbf{q}}(\mathbf{r}) = \frac{\mathbf{e}_{\lambda\mathbf{q}}}{\sqrt{\mu_0\epsilon_0}} e^{i\mathbf{q}\cdot\mathbf{r}}. \tag{A.14}$$

The equation of motion becomes:

$$\omega^2_{\lambda\mathbf{q}} \mu_0\epsilon_0 \boldsymbol{\epsilon}_r \mathbf{e}_{\lambda\mathbf{q}} + \mathbf{q}\left(\mathbf{q}\cdot\mathbf{e}_{\lambda\mathbf{q}}\right) - q^2 \mathbf{e}_{\lambda\mathbf{q}} = 0, \tag{A.15}$$

the orthogonality condition

$$\mathbf{e}^\dagger_{\lambda\mathbf{q}} \boldsymbol{\epsilon}_r \mathbf{e}_{\lambda'\mathbf{q}} = \delta_{\lambda,\lambda'}\ , \tag{A.16}$$

and the relation connecting λ and $-\lambda$:

$$q^*_{\lambda\mathbf{q}}\mathbf{e}^*_{\lambda\mathbf{q}} = q_{-\lambda,-\mathbf{q}}\mathbf{e}_{-\lambda,-\mathbf{q}}. \tag{A.17}$$

Then the vector potential can be written as

$$\begin{aligned}\mathbf{A}(\mathbf{r},t) &= \sum_{\lambda\mathbf{q}} q_{\lambda\mathbf{q}}\frac{\mathbf{e}_{\lambda\mathbf{q}}}{\sqrt{\mu_0\epsilon_0}}e^{i(\mathbf{q}\cdot\mathbf{r}+\omega_{\lambda\mathbf{q}}t)} \\ &= c\sum_{\lambda>0,\mathbf{q}} q_{\lambda\mathbf{q}}\mathbf{e}_{\lambda\mathbf{q}}e^{i(\mathbf{q}\cdot\mathbf{r}+\omega_{\lambda\mathbf{q}}t)} + q^*_{\lambda\mathbf{q}}\mathbf{e}^*_{\lambda\mathbf{q}}e^{-i(\mathbf{q}\cdot\mathbf{r}+\omega_{\lambda\mathbf{q}}t)}\end{aligned} \tag{A.18}$$

and the conjugate momentum becomes:

$$\mathbf{\Pi}(\mathbf{r},t) = c\sum_{\lambda\mathbf{q}} iq_{\lambda\mathbf{q}}\omega_{\lambda\mathbf{q}}\epsilon_0\epsilon_r\mathbf{e}_{\lambda\mathbf{q}}e^{i(\mathbf{q}\cdot\mathbf{r}+\omega_{\lambda\mathbf{q}}t)}. \tag{A.19}$$

The Hamiltonian can be written as:

$$\begin{aligned}\mathcal{H} &= \epsilon_0c^2V\sum_{\lambda\mathbf{q}}\omega^2_{\lambda\mathbf{q}}q^*_{\lambda\mathbf{q}}q_{\lambda\mathbf{q}} \\ &= \epsilon_0c^2V\sum_{\lambda>0,\mathbf{q}}\omega^2_{\lambda\mathbf{q}}(q^*_{\lambda\mathbf{q}}q_{\lambda\mathbf{q}} + q_{\lambda\mathbf{q}}q^*_{\lambda\mathbf{q}}),\end{aligned} \tag{A.20}$$

where V is the volume of the system. Finally, we can define creation and annihilation operators for $\lambda > 0$:

$$\hat{a}_{\lambda\mathbf{q}} = c\sqrt{\frac{2V\omega_{\lambda\mathbf{q}}\epsilon_0}{\hbar}}q_{\lambda\mathbf{q}}, \quad \left[\hat{a}_{\lambda\mathbf{q}}, \hat{a}^\dagger_{\lambda'\mathbf{q}'}\right] = \delta_{\mathbf{q},\mathbf{q}'}\delta_{\lambda,\lambda'} \tag{A.21}$$

using which the vector potential operator becomes:

$$\mathbf{A}(\mathbf{r},t) = \sum_{\lambda\mathbf{q}}\sqrt{\frac{\hbar}{2V\omega_{\lambda\mathbf{q}}\epsilon_0}}\left(\hat{a}_{\lambda\mathbf{q}}\mathbf{e}_{\lambda\mathbf{q}}e^{i(\mathbf{q}\cdot\mathbf{r}+\omega_{\lambda\mathbf{q}}t)} + h.c.\right) \tag{A.22}$$

and the Hamiltonian:

$$\mathcal{H} = \sum_{\lambda\mathbf{q}}\hbar\omega_{\lambda\mathbf{q}}\left(\hat{a}^\dagger_{\lambda\mathbf{q}}\hat{a}_{\lambda\mathbf{q}} + \frac{1}{2}\right). \tag{A.23}$$

Appendix B

DERIVATION OF THE RADIATIVE RECOMBINATION RATE IN ISOTROPIC 3D MATERIALS

We provide additional details for the derivation of the radiative recombination rate in isotropic 3D materials, Eq. (2.13). In an isotropic bulk material with dielectric constant ϵ, the photon vector potential is given by Eq. (A.22) with frequency $\omega_{\mathbf{q}} = c\,|\mathbf{q}|/\sqrt{\epsilon}$, and the IP and OOP polarization vectors are those in Eq. (2.11). Due to momentum conservation, the summation over all possible final photon wavevectors in Eq. (2.1) is restricted to $\mathbf{q} = \mathbf{Q}$. As a result, we can write the radiative rate as

$$\gamma_S^{3D,iso}(\mathbf{Q}) = \frac{\pi e^2}{\epsilon_0 m^2 V c Q \sqrt{\epsilon}} \left\{ \left| -p_{Sx} \sin\varphi + p_{Sy} \cos\varphi \right|^2_{\mathrm{IP}} + \left| p_{Sx} \cos\theta \cos\varphi + p_{Sy} \cos\theta \sin\varphi - p_{Sz} \sin\theta \right|^2_{\mathrm{OOP}} \right\} \times \delta\left(E_S(\mathbf{Q}) - \frac{\hbar c Q}{\sqrt{\epsilon}} \right). \tag{B.1}$$

By setting $\cos\varphi = Q_x/Q_{xy}$, where $\mathbf{Q}_{xy}$ is the projection of $\mathbf{Q}$ onto the xy plane, and $\cos\theta = Q_z/Q$, we obtain Eq. (2.12). To obtain the radiative rate at finite temperature T, we plug Eq. (2.12) into Eq. (2.2) along with the parabolic dispersion in Eq. (2.3). The denominator, due to lack of angular dependence, reduces to a Gaussian integral of the kind $\int_0^\infty dx\, x^2 \exp(-x^2) = \sqrt{\pi}/4$, and gives

$$\int dQ_x dQ_y dQ_z e^{-E_S(Q)/k_B T} = \int d\Omega \int_0^\infty dQ\, Q^2\, e^{\frac{-\hbar^2 Q^2}{2M_S k_B T}} = \left(\frac{2\pi M_S k_B T}{\hbar^2} \right)^{3/2} \tag{B.2}$$

where $d\Omega = \sin\theta d\theta d\varphi$ is the differential solid angle, and we leave out the factor $e^{-E_S(0)/k_B T}$, which is present both in the numerator and denominator and cancels out in the final result. For the numerator, we note that the exciton parabolic dispersion can be approximated as flat within the light cone, so that we can put $E_S(\mathbf{Q}) \approx E_S(0)$. As a result, we get

$$\int dQ_x dQ_y dQ_z\, e^{-E_S(Q)/k_B T}\, \gamma_S^{3D,iso}(\mathbf{Q}) = \approx \frac{\pi e^2}{\epsilon_0 m^2 V c \sqrt{\epsilon}} \int d\Omega \int dQ\; Q \left\{ \left| -p_{Sx} \sin\varphi + p_{Sy} \cos\varphi \right|^2 \right.$$

$$+\left|p_{Sx}\cos\theta\cos\varphi+p_{Sy}\cos\theta\sin\varphi-p_{Sz}\sin\theta\right|^2\Big\}\,\delta\!\left(E_S(0)-\frac{\hbar cQ}{\sqrt{\epsilon}}\right)$$

$$=\frac{\pi e^2}{\epsilon_0 m^2 V c\sqrt{\epsilon}}\int d\varphi\,d\theta\,\sin\theta\int dQ\;Q\left\{|p_{Sx}|^2\sin^2\varphi+|p_{Sy}|^2\cos^2\varphi\right.$$

$$\left.+|p_{Sx}|^2\cos^2\theta\cos^2\varphi+|p_{Sy}|^2\cos^2\theta\sin^2\varphi+|p_{Sz}|^2\sin^2\theta\right\}\delta\!\left(E_S(0)-\frac{\hbar cQ}{\sqrt{\epsilon}}\right)$$

$$=\frac{8\pi^2e^2p_S^2}{3\epsilon_0 m^2 V c\sqrt{\epsilon}}\int dQ\;Q\cdot\delta\!\left(E_S(0)-\frac{\hbar cQ}{\sqrt{\epsilon}}\right)=\frac{8\pi^2\sqrt{\epsilon}e^2p_S^2E_S(0)}{3\epsilon_0\hbar^2c^3m^2V}. \tag{B.3}$$

After dividing the numerator by the denominator, we obtain

$$\langle\gamma_S^{3D,iso}\rangle(T)=\frac{8\sqrt{\pi\epsilon}\,e^2\,\hbar\,p_S^2}{3\,\epsilon_0 m^2 V E_S(0)^2}\left(\frac{E_S(0)^2}{2M_Sc^2k_BT}\right)^{3/2}, \tag{B.4}$$

namely the finite temperature radiative lifetime in Eq. (2.13).

Appendix C

DERIVATION OF THE RADIATIVE RECOMBINATION RATE IN 2D MATERIALS

We provide additional details for the derivation of the radiative recombination rate in 2D systems, Eq. (2.15) and Eq. (2.16). Without loss of generality, we apply Eq. (2.1) with exciton momentum $\mathbf{Q} = Q\cos\varphi\hat{\mathbf{x}} + Q\sin\varphi\hat{\mathbf{y}}$ lying in the xy-plane containing the material. As emphasized in the main text, translation symmetry applies only in the xy-plane while leaving the momentum along z-aixs unrestricted. Thus, Eq. (2.1) is refined into:

$$\begin{aligned}\gamma_S(\mathbf{Q}) &= \frac{2\pi}{\hbar}\sum_{\lambda\mathbf{q}}^{\{(\mathbf{q}\cdot\hat{Q})\hat{Q}=\mathbf{Q}\}} \left|\langle G, 1_{\lambda\mathbf{q}}|H^{int}|S\mathbf{Q},0\rangle\right|^2 \delta(E_S(\mathbf{Q})-\hbar cq) \\ &= \frac{\pi e^2}{\epsilon_0 m^2 cV}\sum_{\lambda\mathbf{q}}^{\{(\mathbf{q}\cdot\hat{Q})\hat{Q}=\mathbf{Q}\}} \frac{1}{q}\left|\mathbf{e}_{\lambda\mathbf{q}}\cdot\langle G|\mathbf{p}|S\mathbf{Q}\rangle\right|^2 \delta(E_S(\mathbf{Q})-\hbar cq). \quad \text{(C.1)}\end{aligned}$$

To evaluate Eq. (C.1), we take the continuous limit of the summation over the photon wavevector, using A for the area of the system and L_z for its length along z (so that $V = A\cdot L_z$), and imposing the constraint $q^2 = Q^2 + q_z^2$ inside the delta function, with the 2D dipole moment $\mathbf{p}_S = \langle G|\mathbf{p}|S\mathbf{Q}\rangle = p_{Sx}\hat{\mathbf{x}} + p_{Sy}\hat{\mathbf{y}}$, we obtain Eq. (2.15) of the main text:

$$\begin{aligned}\gamma_S(\mathbf{Q}) &= \frac{\pi e^2}{\epsilon_0 m^2 cV}\frac{L_z}{2\pi}\int_{-\infty}^{\infty} dq_z \frac{1}{q}\Big(|-p_{Sx}\sin\varphi + p_{Sy}\cos\varphi|^2_{\mathrm{IP}} \\ &\qquad + \cos^2\theta|-p_{Sx}\cos\varphi - p_{Sy}\sin\varphi|^2_{\mathrm{OOP}}\Big)\,\delta\left(E_S(\mathbf{Q})-\hbar cq\right) \\ &= \frac{e^2 p_S^2}{2\epsilon_0 m^2 cA}\,2\int_0^{\infty}\frac{dq_z}{q}\left(\left|-\frac{p_{Sx}}{p_S}\sin\varphi + \frac{p_{Sy}}{p_S}\cos\varphi\right|^2_{\mathrm{IP}}\right. \\ &\qquad \left. + \frac{q_z^2}{q^2}\left|\frac{p_{Sx}}{p_S}\cos\varphi + \frac{p_{Sy}}{p_S}\sin\varphi\right|^2_{\mathrm{OOP}}\right)\delta\left(\frac{E_S(\mathbf{Q})}{\hbar c} - \sqrt{q_z^2+Q^2}\right) \\ &= \frac{e^2 p_S^2}{\epsilon_0 m^2 cA}\cdot\int_Q^{\infty}\frac{dq}{\sqrt{q^2-Q^2}}\left(\left|-\frac{p_{Sx}}{p_S}\sin\varphi + \frac{p_{Sy}}{p_S}\cos\varphi\right|^2_{\mathrm{IP}}\right. \\ &\qquad \left. + \frac{q^2-Q^2}{q^2}\left|\frac{p_{Sx}}{p_S}\cos\varphi + \frac{p_{Sy}}{p_S}\sin\varphi\right|^2_{\mathrm{OOP}}\right)\delta\left(\frac{E_S(\mathbf{Q})}{\hbar c} - q\right)\end{aligned}$$

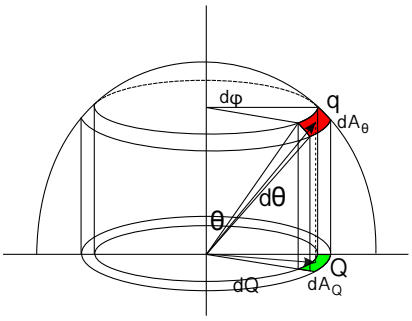

Figure C.1: **Exciton ratiation phase space.** An exciton associated with the phase space area $dA_{\mathbf{Q}}$ (shown in green) decays radiatively by emitting a photon through the area dA_θ (shown in red).

$$= \gamma_S(0) \cdot \left(\frac{E_S(0)}{\sqrt{E_S^2(Q) - \hbar^2 c^2 Q^2}} \right) \left\{ \left| -\frac{p_{Sx}}{p_S} \sin\varphi + \frac{p_{Sy}}{p_S} \cos\varphi \right|^2_{\text{IP}} + \frac{E_S(Q)^2 - \hbar^2 c^2 Q^2}{E_S(Q)^2} \left| \frac{p_{Sx}}{p_S} \cos\varphi + \frac{p_{Sy}}{p_S} \sin\varphi \right|^2_{\text{OOP}} \right\}. \tag{C.2}$$

Angular Dependence of the Radiative Rate

To compute the PL intensity emitted as a function of angle by an exciton S upon recombination, we first substitute

$$\frac{\sqrt{E_S^2(Q) - \hbar^2 c^2 Q^2}}{E_S(0)} \approx \frac{\sqrt{E_S^2(Q) - \hbar^2 c^2 Q^2}}{E_S(Q)} = \cos\theta$$

in Eq. (4) of the main text, and obtain:

$$\gamma_S(\mathbf{Q}) = \frac{\gamma_S(0)}{\cos\theta} \cdot \left\{ \left| -\frac{p_{Sx}}{p_S} \sin\varphi + \frac{p_{Sy}}{p_S} \cos\varphi \right|^2_{\text{IP}} + \cos^2\theta \left| \frac{p_{Sx}}{p_S} \cos\varphi + \frac{p_{Sy}}{p_S} \sin\varphi \right|^2_{\text{OOP}} \right\}. \tag{C.3}$$

Guided by Fig. S1 below, we then convert $\gamma_S(\mathbf{Q})$ to $\gamma_S(\theta, \varphi)$, as follows. For an exciton in state S and with center-of-mass momentum $\mathbf{Q}$ located around a small area $dA_{\mathbf{Q}}$ in phase space, the emission occurs over a small solid angle spanned by the area dA_θ. One can thus write:

$$\gamma_S(\theta, \varphi)\, dA_\theta = \gamma_S(\mathbf{Q})\, dA_{\mathbf{Q}}. \tag{C.4}$$

Using $dA_{\mathbf{Q}} = Q\, dQ\, d\varphi$ as well as $dA_\theta = q^2 \sin\theta\, d\theta\, d\varphi$, as seen in Fig. S1, together with $Q = q \sin\theta$, we obtain:

$$\gamma_S(\theta, \varphi) = \gamma_S(\mathbf{Q}) \cos\theta. \tag{C.5}$$

Using Eq. C.3, we finally obtain:

$$\gamma_S(\theta, \varphi) = \gamma_S(0) \left\{ \left| -\frac{p_{Sx}}{p_S} \sin\varphi + \frac{p_{Sy}}{p_S} \cos\varphi \right|^2_{\text{IP}} + \cos^2\theta \left| \frac{p_{Sx}}{p_S} \cos\varphi + \frac{p_{Sy}}{p_S} \sin\varphi \right|^2_{\text{OOP}} \right\}. \tag{C.6}$$

This result is given in Eqs. (2.23) and Eqs. (2.24) of the main text, where the IP and OOP rates are given separately.

Appendix D

DERIVATION OF THE RADIATIVE RECOMBINATION RATE IN 0D SYSTEMS

We provide additional details for the derivation of the radiative recombination rate in 0D systems, Eq. (2.20). As discussed above, in the 0D case there is no constraint from momentum conservation on the emitted photon wavevector. Therefore, we replace the summation in Eq. (2.1) by an integration over the full momentum space and write

$$\gamma_S^{0D} = \frac{\pi e^2}{\epsilon_0 m^2} \sum_\lambda \int \frac{d\Omega\, dq\, q^2}{(2\pi)^3} \frac{\left|\mathbf{e}_{\lambda\mathbf{q}} \cdot \mathbf{p}_S(\mathbf{Q})\right|^2}{\omega_{\lambda\mathbf{q}}} \delta\left(E_S - \hbar\omega_{\lambda\mathbf{q}}\right) \tag{D.1}$$

which comes from rewriting the summation along each cartesian component α as $\sum_{q_\alpha} = \int L_\alpha dq_\alpha/2\pi$, and $L_x L_y L_z = V$. In the 0D case, we can apply the photon quantization solutions used in the 3D case, so that λ = IP or OOP, and $\mathbf{e}_{\lambda\mathbf{q}}$ are in the form of Eq. (2.11) with $\omega_{\lambda\mathbf{q}} = c|\mathbf{q}|/\sqrt{\epsilon}$. Note that this approach applies both to isolated emitters, such as quantum dots and molecules, as well as to atoms, ions or other single quantum emitters embedded in an isotropic material. Combining these results, we can write

$$\begin{aligned}\gamma_S^{0D} = \frac{\pi e^2}{8\epsilon_0 m^2 \pi^3 c\sqrt{\epsilon}} \int d\varphi\, d\theta \sin\theta \int dq\, q \left\{\left|-p_{Sx}\sin\varphi + p_{Sy}\cos\varphi\right|^2 \right. \\ \left. + \left|p_{Sx}\cos\theta\cos\varphi + p_{Sy}\cos\theta\sin\varphi - p_{Sz}\sin\theta\right|^2\right\} \delta\left(E_S - \frac{\hbar c q}{\sqrt{\epsilon}}\right)\end{aligned} \tag{D.2}$$

and finally obtain Eq. (2.20),

$$\gamma_S^{0D} = \frac{\sqrt{\epsilon} e^2 p_S^2 E_S}{3\pi\epsilon_0 m^2 c^3 \hbar^2}. \tag{D.3}$$

Appendix E

RADIATIVE LIFETIME OF EXCITONS WITH LINEAR DISPERSION

We provide an additional discussion for excitons with linear dispersion:

$$E_S(\mathbf{Q}) = E_S(0) + B|\mathbf{Q}|. \tag{E.1}$$

The radiative lifetime at finite temperature can still be derived using Eq. (2.2). The linear exciton dispersion merely changes the phase-space integral in the denominator of Eq. (2.2), leading to a simple extension of the treatment for parabolic exciton dispersion. The phase-space integral in d dimensions can be written as:

$$I(d) = \int d\Omega_d \int dQ Q^{d-1} \exp\left[\frac{-BQ}{k_B T}\right], \tag{E.2}$$

where d is the dimensionality of the material and Ω_d is the $d-$dimensional differential solid angle. We obtain:

$$I(d) = \begin{cases} 8\pi(k_B T/B)^3 & d = 3 \\ 2\pi(k_B T/B)^2 & d = 2 \\ 2(k_B T/B) & d = 1 \end{cases}. \tag{E.3}$$

Using this result together with Eq. (2.2), we obtain the radiative lifetimes in isotropic 3-, 2- and 1-dimensional materials with linear exciton dispersion:

$$\langle \gamma_S^{\mathrm{d},iso} \rangle_{linear}(T) = \begin{cases} \frac{\pi\sqrt{\epsilon} e^2 \hbar p_S^2}{3\epsilon_0 m^2 V E_S(0)^2} \left(\frac{BE_S(0)}{ck_B\hbar T}\right)^3 & d = 3 \\ \gamma_S^{2D}(0) \times \frac{2}{3}\left(\frac{BE_S(0)}{ck_B\hbar T}\right)^2 & d = 2 \\ \gamma_S^{1D}(0) \times \frac{2}{3}\frac{BE_S(0)}{ck_B\hbar T} & d = 1, \end{cases} \tag{E.4}$$

where $\gamma_S^{2D}(0)$ and $\gamma_S^{1D}(0)$ are the intrinsic radiative rates in 2D and 1D systems, respectively, which are defined in the main text and are independent of the exciton dispersion. The radiative lifetimes, $\langle \tau_S \rangle = \langle \gamma_S \rangle^{-1}$, for excitons with linear dispersion exhibit a stronger temperature dependence, $\langle \tau_S^{\mathrm{d},iso} \rangle_{linear}(T) \propto T^d$, versus $\langle \tau_S^{\mathrm{d},iso} \rangle_{parabolic}(T) \propto T^{d/2}$ for the parabolic exciton dispersion case. For 2D materials with linear exciton dispersions, which have been recently predicted, the radiative lifetimes are thus expected to follow a T^2 trend with temperature.

Appendix F

NUMERICAL INFORMATION FOR THE COMPUTATION OF EXCITONS IN 2D HEXAGONAL BORON NITRIDE DEFECTS

We carry out DFT calculations in the generalized gradient approximation using the Perdew-Burke-Ernzerhof (PBE) exchange-correlation functional [74]. Our spin-polarized DFT calculations employ the plane-wave pseudopotential method implemented in Quantum Espresso [80]. The defects are placed in a $5 \times 5 \times 1$ supercell of hBN with the lattice constant kept fixed at 5×2.504 Å while the atoms are fully relaxed without symmetry constraints. For calculations on monolayer h-BN, a vacuum of 15 Å is used to avoid spurious inter-layer interactions with the periodic replicas. We use ONCV pseudopotentials [192, 247] for all atoms along with a plane-wave kinetic energy cutoff of 80 Ry and a $3 \times 3 \times 1$ **k**-point Brillouin zone grid. The GW-BSE calculations are carried out with the Yambo code [86] using a 2D slab cutoff of the Coulomb interaction. For calculations of defects in monolayer h-BN, a $3 \times 3 \times 1$ **k**-point grid is employed together with an energy cutoff of 10 Ry for the dielectric matrix. The number of empty bands included in the GW calculation (for the polarizability and self-energy summations) is 7 times the number of occupied bands.

Appendix G

ELECTRON-PHONON INTERACTION IN FIRST-ORDER PERTURBATION THEORY

In this appendix, we derive the e-ph coupling using the method introduced in Sect. 3.1 to validate our approach. After the introducing of deformation potential following Eq. (3.2), we second quantize the perturbed Hamiltonian, introducing unperturbed electron creation and annihilation operators, $\hat{c}^\dagger$ and $\hat{c}$, and rewrite the perturbed Hamiltonian as

$$\tilde{H} = H_0 + \Delta V, \quad \text{where } H_0 = \sum_i \epsilon_i \hat{c}_i^\dagger \hat{c}_i \quad \text{and} \quad \hat{c}_i^\dagger |0\rangle = |\phi_i\rangle. \tag{G.1}$$

In addition, we project the perturbed Hamiltonian onto the unperturbed basis states $|\phi_i\rangle$:

$$\begin{aligned} \tilde{H} &= \sum_{ij} \langle \phi_i | \tilde{H} | \phi_j \rangle \hat{c}_i^\dagger \hat{c}_j = \sum_{ij,kl} \langle \phi_i | \tilde{\phi}_k \rangle \langle \tilde{\phi}_k | \tilde{H} | \tilde{\phi}_l \rangle \langle \tilde{\phi}_l | \phi_j \rangle \hat{c}_i^\dagger \hat{c}_j \\ &= \sum_{ij,k} \tilde{\epsilon}_k \langle \phi_i | \tilde{\phi}_k \rangle \langle \tilde{\phi}_k | \phi_j \rangle \hat{c}_i^\dagger \hat{c}_j \approx \sum_{ij,k} \epsilon_k \langle \phi_i | \tilde{\phi}_k \rangle \langle \tilde{\phi}_k | \phi_j \rangle \hat{c}_i^\dagger \hat{c}_j, \end{aligned} \tag{G.2}$$

where in the first line we insert the complete perturbed basis set, $\sum_k |\tilde{\phi}_k\rangle\langle\tilde{\phi}_k| = 1$, with basis elements satisfying $\tilde{H}|\tilde{\phi}_k\rangle = \tilde{\epsilon}_k|\tilde{\phi}_k\rangle$, and in the second line we neglect the electronic eigenvalue correction due to the real part of the e-ph self-energy and approximate the perturbed eigenvalues as $\tilde{\epsilon}_k \approx \epsilon_k$ to first order.

Next, we use Eq. (3.5) to expand the inner product of the unperturbed and perturbed wave functions to first order, $\langle \phi_i | \tilde{\phi}_k \rangle \approx \delta_{ik} + \sum_{\alpha \neq k} \Delta_{k\alpha} \delta_{i\alpha}$, and dropping terms of order $O(\Delta^2)$ we obtain:

$$\begin{aligned} \tilde{H} &\approx \sum_{ij,k} \epsilon_k \left(\delta_{ik} + \sum_{\alpha \neq k} \Delta_{k\alpha} \delta_{i\alpha} \right) \left(\delta_{jk} + \sum_{\beta \neq k} \Delta^*_{k\beta} \delta_{j\beta} \right) \hat{c}_i^\dagger \hat{c}_j \\ &= \sum_k \epsilon_k \hat{c}_k^\dagger \hat{c}_k + {\sum_{ij}}' \left(\epsilon_i \Delta^*_{ij} + \epsilon_j \Delta_{ji} \right) \hat{c}_i^\dagger \hat{c}_j, \end{aligned} \tag{G.3}$$

where the prime in the summation $\sum'_{ij}$ indicates $i \neq j$. Using Eq. (3.6), we obtain the perturbed Hamiltonian in a form that will be useful below:

$$\tilde{H} = \sum_k \epsilon_k \hat{c}_k^\dagger \hat{c}_k + {\sum_{ij}}' \left(\epsilon_i \frac{\langle \phi_i | \Delta V | \phi_j \rangle}{\epsilon_i - \epsilon_j} + \epsilon_j \frac{\langle \phi_i | \Delta V | \phi_j \rangle}{\epsilon_j - \epsilon_i} \right) \hat{c}_i^\dagger \hat{c}_j$$

$$= \sum_k \epsilon_k \hat{c}_k^\dagger \hat{c}_k + \sum_{ij}{}' \langle \phi_i | \Delta V | \phi_j \rangle \hat{c}_i^\dagger \hat{c}_j. \tag{G.4}$$

By expanding ΔV as a sum of phonon modes, one can also derive the usual e-ph interaction Hamiltonian.

This result holds true also in the presence of degenerate electronic states. Taking the possibility of degenerate states into account, the perturbation expansion in Eq. (3.5) is modified as:

$$|\tilde{\phi}_i\rangle = \sum_{j\in\mathcal{D}} \alpha_{ij} \left(|\phi_j\rangle + \sum_{k\notin\mathcal{D}} \Delta_{jk} |\phi_k\rangle \right) \quad \text{with} \quad \sum_{k\in\mathcal{D}} \alpha_{ik} \langle \phi_j | \Delta V | \phi_k \rangle = \epsilon_i^{(1)} \alpha_{ij}, \tag{G.5}$$

where $\mathcal{D}$ is the degenerate subspace containing the unperturbed state ϕ_i, α_{ij} is the unitary transformation mixing states within the subspace, and $\epsilon_i^{(1)}$ is the first-order correction to the energy eigenvalue, which is proportional to the intra-subspace coupling $\langle \phi_j | \Delta V | \phi_k \rangle$ and can no longer be neglected. Substituting Eq. (G.5) into Eq. (G.2) and using the unitarity condition $\sum_k \alpha_{ik} \alpha_{jk}^* = \delta_{ij}$, we obtain the same formula as in Eq. (G.3) for inter-subspace scattering:

$$H_{\text{inter- subspace}} = \sum_{\mathcal{D}\mathcal{D}'}{}' \sum_{i\in\mathcal{D}} \sum_{j\in\mathcal{D}'} \left(\epsilon_i \Delta_{ij}^* + \epsilon_j \Delta_{ji} \right) \hat{c}_i^\dagger \hat{c}_j = \sum_{\mathcal{D}\mathcal{D}'}{}' \sum_{i\in\mathcal{D}} \sum_{j\in\mathcal{D}'} \langle \phi_i | \Delta V | \phi_j \rangle \hat{c}_i^\dagger \hat{c}_j, \tag{G.6}$$

where the prime in the summation $\sum'_{\mathcal{D}\mathcal{D}'}$ indicates $\mathcal{D} \neq \mathcal{D}'$, while intra-subspace scattering adds new terms:

$$\begin{aligned} H_{\text{intra- subspace}} &= \sum_{\mathcal{D}} \sum_{ijk\in\mathcal{D}} \epsilon_k^{(1)} \alpha_{ki} \alpha_{kj}^* \hat{c}_i^\dagger \hat{c}_j = \sum_{\mathcal{D}} \sum_{ijkk'\in\mathcal{D}} \alpha_{kk'} \alpha_{kj}^* \langle \phi_i | \Delta V | \phi_{k'} \rangle \hat{c}_i^\dagger \hat{c}_j \\ &= \sum_{\mathcal{D}} \sum_{ijk'\in\mathcal{D}} \delta_{jk'} \langle \phi_i | \Delta V | \phi_{k'} \rangle \hat{c}_i^\dagger \hat{c}_j = \sum_{\mathcal{D}} \sum_{ij\in\mathcal{D}} \langle \phi_i | \Delta V | \phi_j \rangle \hat{c}_i^\dagger \hat{c}_j, \end{aligned} \tag{G.7}$$

where the $i = j$ term contributes only to second order. After combining Eq. (G.7), Eq. (G.6) and the diagonal term $\sum_k \epsilon_k \hat{c}_k^\dagger \hat{c}_k$, we obtain the e-ph interaction Hamiltonian in the same form as Eq. (G.4), which therefore is valid also in the presence of degenerate electronic states.

Appendix H

NUMERICAL INFORMATION FOR EX-PH DYNAMICS CALCULATION IN HEXAGONAL BORON NITRIDE

The numerical calculations on h-BN are carried out within the local density approximation of DFT using the QUANTUM ESPRESSO code [80]. We use norm-conserving pseudopotentials [248, 249] and a 60 Ry kinetic energy cutoff to compute the electronic structure (with DFT) and lattice vibrations (with DFPT, which correctly includes the Frohlich interaction). The e-ph calculations are carried out with the PERTURBO code [90], while GW and finite-momentum BSE calculations are carried out with the YAMBO code [86]. The same $24 \times 24 \times 4$ Brillouin zone grid is used for $\mathbf{k}$-points (for electrons), $\mathbf{q}$-points (for phonons) and $\mathbf{Q}$-points (for excitons). The ex-ph matrix elements are computed without interpolation or symmetry. For the ex-ph scattering rates, we use linear interpolation to obtain the matrix elements and exciton energies on a $120 \times 120 \times 20$ Brillouin zone grid.

In our calculations, the same set of electronic wave functions are employed in the e-ph and BSE calculations, so that the ex-ph matrix elements in Eq. (3.21) of the main text are not affected by the random phase of the electronic wave functions. The quasiparticle energies are corrected using a one-shot plasmon-pole GW calculation (with a 10 Ry cutoff and 100 bands) before solving the BSE at finite center-of-mass exciton momenta. For the BSE, we use a 10 Ry cutoff for the statically screened Coulomb interaction and the two highest valence and two lowest conduction bands to obtain the lowest 8 excitonic states, of which 2 are bright and 6 are dark excitons at $\mathbf{Q} = 0$. The ex-ph matrix elements are computed without interpolation or symmetry, using full Brillouin zone grids to converge the sum over $\mathbf{k}$-points in Eq. (3.21) of the main text. The delta function in the scattering rate equation is approximated by a Gaussian with a small broadening of 4 meV.

Further, one point to be noted for the construction of the BSE kernel. When computing optical processes, one usually focuses on transverse excitons and removes the long-range part ($\mathbf{G} = 0$ component, where $\mathbf{G}$ is a reciprocal lattice vector) of the Hartree potential from the kernel [250, 251]. However, for ex-ph interactions, both transverse and longitudinal excitons need to be considered, so we use the full

Coulomb interaction (including the $\mathbf{G} = 0$ Hartree term) in the BSE kernel [1].

Here we show the convergence of the ex-ph scattering rate for the lowest-energy exciton band (the one with slowest convergence) by comparing results obtained with Brillouin zone grids of $24 \times 24 \times 4$ and $18 \times 18 \times 4$. It is seen that the scattering rates obtained with the two grids are in good agreement, so the values shown in the main text (for a $24 \times 24 \times 4$ grid) are expected to be reasonably well converged (say, within $\sim 10 - 20\%$ of the infinite-grid limit). Note that the same grid is used for **k**-points (for electrons), **q**-points (for phonons), and **Q**-points (for excitons).

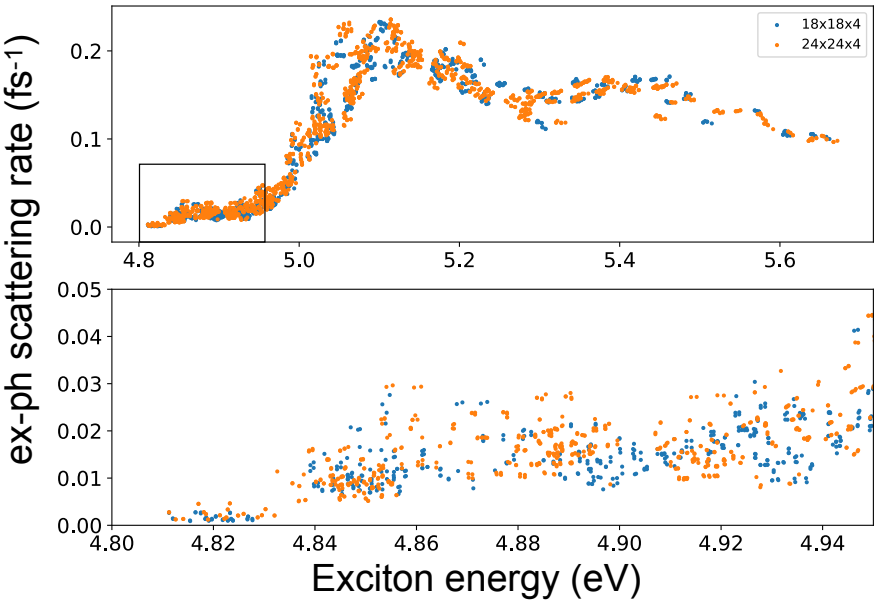

Figure H.1: **Convergence of ex-ph scattering rate calculation.** The ex-ph scattering rate for the lowest exciton band, computed with two Brillouin zone grids of $24 \times 24 \times 4$ (orange) and $18 \times 18 \times 4$ (blue). The lower panel zooms in the low-energy region (below the LO emission threshold) marked by a rectangle in the upper panel.

[1] private communication with Fulvio Paleari and Andrea Marini

Appendix I

NUMERICAL INFORMATION FOR EX-PH DYNAMICS CALCULATION IN MONOLAYER TUNGSTEN DISELENIDE

The DFT calculations on WSe_2 are carried out within the generalized gradient approximation (GGA) [74] using the QUANTUM ESPRESSO code with spin-orbital coupling included [80]. The fully relativistic norm-conserving pseudopotentials generated with Pseudo Dojo [75, 248, 249] and a 60 Ry kinetic energy cutoff are used to compute the electronic structure (with DFT) and lattice vibrations (with DFPT) [61]. The resultant electronic band structure is then fine-tuned according to the experimental measurement. The e-ph calculations are carried out with the PERTURBO code [90], while finite-momentum BSE calculations are conducted with the YAMBO code [86]. 7 Ry cutoff is applied with 300 bands for the Coulomb screening while highest 2 valence bands and lowest 2 conduction bands are used to converge the exciton energy in BSE calcuation. The $72 \times 72 \times 1$ Brillouin zone grid is used for $\mathbf{k}$-points (for electrons), while a $36 \times 36 \times 1$ grid (must be commensurate with $\mathbf{k}$-point grid) is applied for $\mathbf{q}$-points (for phonons) and $\mathbf{Q}$-points (for excitons). For the bright exciton emission linewidth and PL calculation, trilinear interpolation is employed to obtain the matrix elements and exciton energies on a $504 \times 504 \times 1$ Brillouin zone grid while the real-time simulation is performed on $144 \times 144 \times 1$ grid with 45 exciton bands.

Substrate dielectric effect on exciton binding energy

Here we present a side study on the substrate dielectric effect on exciton binding energy. We adopt the empirical effective correction on the dielectric constant of layered system [252]:

$$\epsilon(\mathbf{q}) = \epsilon_2 \frac{1 - \frac{(1-\epsilon_2/\epsilon_1)(1-\epsilon_2/\epsilon_3)}{(1+\epsilon_2/\epsilon_1)(1+\epsilon_2/\epsilon_3)} e^{-2qd}}{\left[1 - \frac{(1-\epsilon_2/\epsilon_1)}{1+\epsilon_2/\epsilon_1} e^{-qd}\right]\left[1 - \frac{(1-\epsilon_2/\epsilon_3)}{1+\epsilon_2/\epsilon_3} e^{-qd}\right]}, \tag{I.1}$$

where ϵ_1 and ϵ_3 are the dielectric function of upper substrate and lower substrate, and ϵ_2 is the dielectric function of sandwiched target material. Here we study a simple case with only bottom substrate $\epsilon_3 = 4$ without cap, i.e. $\epsilon_1 = 1$ while using the *ab initio* ϵ_2. We apply it on WSe_2 on $24 \times 24 \times 1$ k-grid and solve BSE for $\mathbf{Q} = \Gamma$, Q, and M respectively. We present the result in Fig. I.1 with all energy renormalized

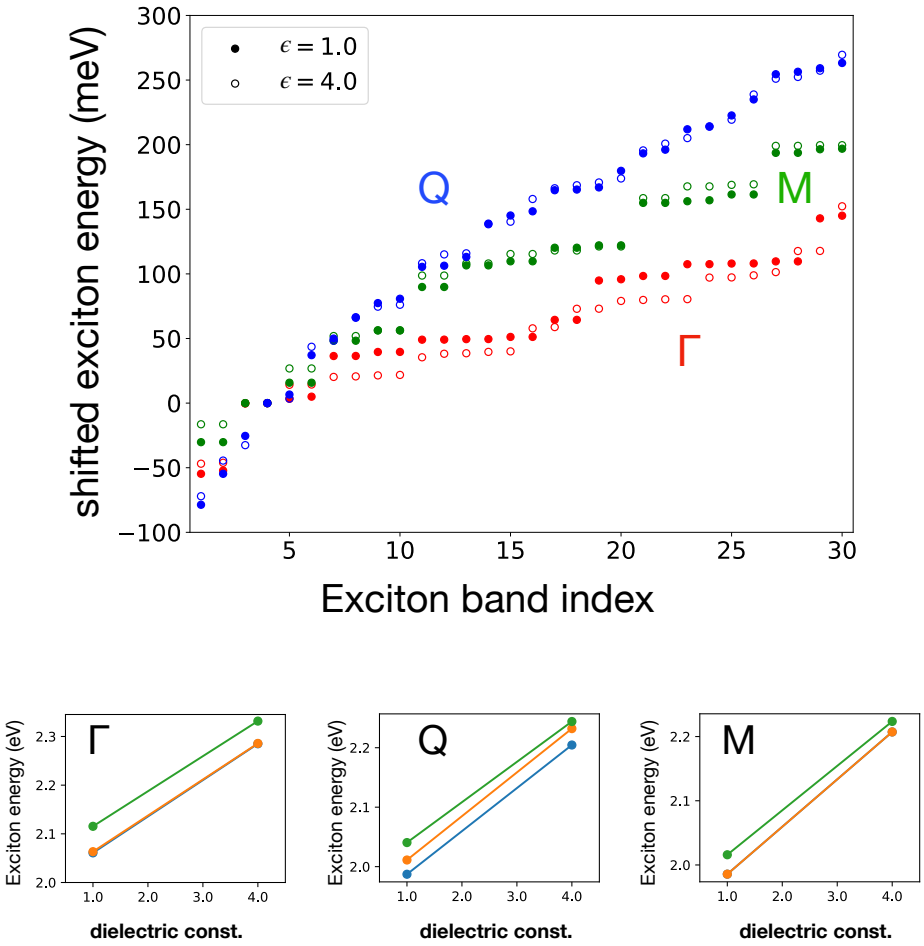

Figure I.1: **Substrate effect on exciton energy in WSe_2**

by the value of their 4-th states in the upper panel. We found a universal decrease of energy by ∼20 meV for the Γ exciton. On the other hand, the change in Q- and M-excitons is in general $\lesssim$10 meV. In the lower panel of Fig. I.1, we present their absolute value for lowest four states which shows a overall rigid blue shift by ∼220 meV in agreement with the experiment measurement [253]. As a result, since only Q- and M-excitonic states are relevant in exciton relaxation processes as studied in Sect. 3.4, provided with $\mathcal{O}$(1 meV) relative correction on the exciton energy presented above, we validate our method adopted to study ex-ph dynamics in WSe_2 which neglects the effects from substrate.

Appendix J

EXCITONIC TR-ARPES SPECTRUM IN LOG-SCALE IN MONOLAYER TUNGSTEN DISELENIDE

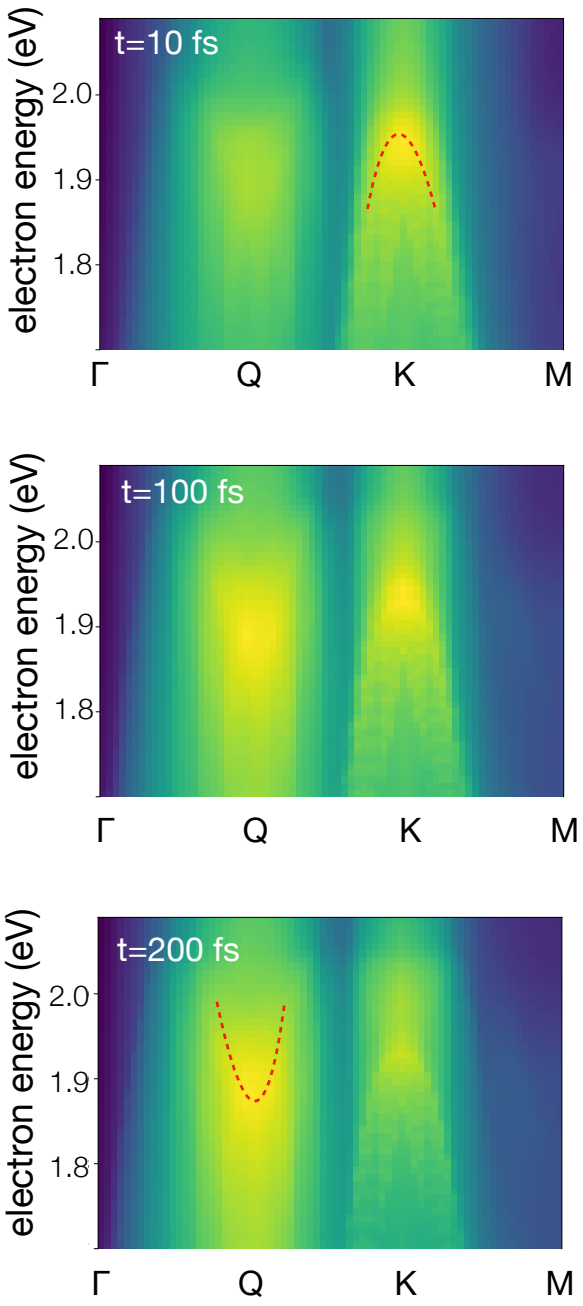

Figure J.1: Snap shot of predicted ARPES in log-scale.

BIBLIOGRAPHY

[1] J. Frenkel, "On the transformation of light into heat in solids. i", Phys. Rev. **37**, 17–44 (1931). DOI: 10.1103/PhysRev.37.17.

[2] J. Frenkel, "On the transformation of light into heat in solids. ii", Phys. Rev. **37**, 1276–1294 (1931). DOI: 10.1103/PhysRev.37.1276.

[3] G. H. Wannier, "The Structure of Electronic Excitation Levels in Insulating Crystals", Phys. Rev. **52**, 191–197 (1937). DOI: 10.1103/PhysRev.52.191.

[4] N. Mott, "Conduction in polar crystals. ii. the conduction band and ultra-violet absorption of alkali-halide crystals", Transactions of the Faraday Society **34**, 500–506 (1938).

[5] R. S. Knox, *Theory of excitons (solid state phys. suppl. 5)*, Vol. 5 (Academic, 1963).

[6] R. Elliott, "Introduction to the theory of excitons", in *Polarons and excitons in polar semiconductors and ionic crystals* (Springer, 1984), pp. 271–292.

[7] M. R. Molas, C. Faugeras, A. Slobodeniuk, K. Nogajewski, M. Bartos, D. Basko, and M. Potemski, "Brightening of dark excitons in monolayers of semiconducting transition metal dichalcogenides", 2D Materials **4**, 021003 (2017).

[8] X.-X. Zhang, T. Cao, Z. Lu, Y.-C. Lin, F. Zhang, Y. Wang, Z. Li, J. C. Hone, J. A. Robinson, D. Smirnov, et al., "Magnetic brightening and control of dark excitons in monolayer wse 2", Nat. Nanotechnol. **12**, 883–888 (2017).

[9] Y. Toyozawa, "Interband effect of lattice vibrations in the exciton absorption spectra", Journal of Physics and Chemistry of Solids **25**, 59–71 (1964). DOI: https://doi.org/10.1016/0022-3697(64)90162-3.

[10] S. Tutihasi, "Optical absorption by silver halides", Phys. Rev. **105**, 882–884 (1957). DOI: 10.1103/PhysRev.105.882.

[11] A. B. Kunz, "Electronic structure of AgF, AgCl, and AgBr", Phys. Rev. B **26**, 2070–2075 (1982). DOI: 10.1103/PhysRevB.26.2070.

[12] G. A. Thomas, A. Frova, J. C. Hensel, R. E. Miller, and P. A. Lee, "Collision broadening in the exciton gas outside the electron-hole droplets in Ge", Phys. Rev. B **13**, 1692–1702 (1976). DOI: 10.1103/PhysRevB.13.1692.

[13] L. Schue, L. Sponza, A. Plaud, H. Bensalah, K. Watanabe, T. Taniguchi, F. ç. Ducastelle, A. Loiseau, and J. Barjon, "Bright luminescence from indirect and strongly bound excitons in h-BN", Phys. Rev. Lett. **122**, 067401 (2019). DOI: 10.1103/PhysRevLett.122.067401.

[14] Z. Li, T. Wang, C. Jin, Z. Lu, Z. Lian, Y. Meng, M. Blei, S. Gao, T. Taniguchi, K. Watanabe, et al., "Emerging photoluminescence from the dark-exciton phonon replica in monolayer WSe_2", Nat. Commun. **10**, 1–7 (2019).

[15] S. Brem, A. Ekman, D. Christiansen, F. Katsch, M. Selig, C. Robert, X. Marie, B. Urbaszek, A. Knorr, and E. Malic, "Phonon-assisted photoluminescence from indirect excitons in monolayers of transition-metal dichalcogenides", Nano Lett. **20**, 2849–2856 (2020).

[16] T. G. Pedersen, "Exciton effects in carbon nanotubes", Carbon **42**, 1007–1010 (2004).

[17] G. Wang, A. Chernikov, M. M. Glazov, T. F. Heinz, X. Marie, T. Amand, and B. Urbaszek, "Colloquium: excitons in atomically thin transition metal dichalcogenides", Rev. Mod. Phys. **90**, 021001 (2018).

[18] T. Mueller and E. Malic, "Exciton physics and device application of two-dimensional transition metal dichalcogenide semiconductors", NPJ 2D Mater. Appl. **2**, 29 (2018).

[19] D. Van Tuan, M. Yang, and H. Dery, "Coulomb interaction in monolayer transition-metal dichalcogenides", Phys. Rev. B **98**, 125308 (2018). DOI: 10.1103/PhysRevB.98.125308.

[20] A. Chernikov, T. C. Berkelbach, H. M. Hill, A. Rigosi, Y. Li, O. B. Aslan, D. R. Reichman, M. S. Hybertsen, and T. F. Heinz, "Exciton binding energy and nonhydrogenic rydberg series in monolayer WS_2", Phys. Rev. Lett. **113**, 076802 (2014). DOI: 10.1103/PhysRevLett.113.076802.

[21] K. F. Mak, C. Lee, J. Hone, J. Shan, and T. F. Heinz, "Atomically thin MoS_2: a new direct-gap semiconductor", Phys. Rev. Lett. **105**, 136805 (2010). DOI: 10.1103/PhysRevLett.105.136805.

[22] A. Splendiani, L. Sun, Y. Zhang, T. Li, J. Kim, C.-Y. Chim, G. Galli, and F. Wang, "Emerging photoluminescence in monolayer MoS_2", Nano Lett. **10**, 1271–1275 (2010). DOI: 10.1021/nl903868w.

[23] M. Remeika, A. T. Hammack, S. V. Poltavtsev, L. V. Butov, J. Wilkes, A. L. Ivanov, K. L. Campman, M. Hanson, and A. C. Gossard, "Pattern formation in the exciton inner ring", Phys. Rev. B **88**, 125307 (2013). DOI: 10.1103/PhysRevB.88.125307.

[24] M. Onga, Y. Zhang, T. Ideue, and Y. Iwasa, "Exciton Hall effect in monolayer MoS_2", Nat. Mater **16**, 1193–1197 (2017).

[25] O. Wada, "Optoelectronic integration based on gaas material", Optical and quantum electronics **20**, 441–474 (1988).

[26] A. High, A. Hammack, L. Butov, M. Hanson, and A. Gossard, "Exciton optoelectronic transistor", Opt. Lett. **32**, 2466–2468 (2007).

[27] S. Tsintzos, P. Savvidis, G. Deligeorgis, Z. Hatzopoulos, and N. Pelekanos, "Room temperature GaAs exciton-polariton light emitting diode", Appl. Phys. Lett. **94**, 071109 (2009).

[28] J. S. Ross, P. Rivera, J. Schaibley, E. Lee-Wong, H. Yu, T. Taniguchi, K. Watanabe, J. Yan, D. Mandrus, D. Cobden, et al., "Interlayer exciton optoelectronics in a 2d heterostructure p–n junction", Nano Lett. **17**, 638–643 (2017).

[29] R. Sundaram, M. Engel, A. Lombardo, R. Krupke, A. Ferrari, P. Avouris, and M. Steiner, "Electroluminescence in single layer MoS_2", Nano Lett. **13**, 1416–1421 (2013).

[30] C. Palacios-Berraquero, "Atomically-thin quantum light emitting diodes", in *Quantum confined excitons in 2-dimensional materials* (Springer, 2018), pp. 71–89.

[31] B. A. Gregg, "Excitonic solar cells", J. Phys. Chem. B **107**, 4688–4698 (2003).

[32] M. Granström, K. Petritsch, A. Arias, A. Lux, M. Andersson, and R. Friend, "Laminated fabrication of polymeric photovoltaic diodes", Nature **395**, 257–260 (1998).

[33] C. J. Brabec, N. S. Sariciftci, and J. C. Hummelen, "Plastic solar cells", Advanced functional materials **11**, 15–26 (2001).

[34] E. Fortin and W. Sears, "Photovoltaic effect and optical absorption in MoS_2", Journal of Physics and Chemistry of Solids **43**, 881–884 (1982).

[35] D. Jariwala, A. R. Davoyan, J. Wong, and H. A. Atwater, "Van der waals materials for atomically-thin photovoltaics: promise and outlook", Acs Photonics **4**, 2962–2970 (2017).

[36] L. J. Sham, S. J. Allen, A. Kamgar, and D. C. Tsui, "Valley-valley splitting in inversion layers on a high-index surface of silicon", Phys. Rev. Lett. **40**, 472–475 (1978). DOI: 10.1103/PhysRevLett.40.472.

[37] F. J. Ohkawa and Y. Uemura, "Theory of valley splitting in an n-channel (100) inversion layer of si i. formulation by extended zone effective mass theory", Journal of the Physical Society of Japan **43**, 907–916 (1977).

[38] Y. P. Shkolnikov, E. P. De Poortere, E. Tutuc, and M. Shayegan, "Valley splitting of alas two-dimensional electrons in a perpendicular magnetic field", Phys. Rev. Lett. **89**, 226805 (2002). DOI: 10.1103/PhysRevLett.89.226805.

[39] O. Gunawan, Y. P. Shkolnikov, K. Vakili, T. Gokmen, E. P. De Poortere, and M. Shayegan, "Valley susceptibility of an interacting two-dimensional electron system", Phys. Rev. Lett. **97**, 186404 (2006). DOI: 10.1103/PhysRevLett.97.186404.

[40] S. Goswami, K. Slinker, M. Friesen, L. McGuire, J. Truitt, C. Tahan, L. Klein, J. Chu, P. Mooney, D. W. Van Der Weide, et al., "Controllable valley splitting in silicon quantum devices", Nat. Phys. **3**, 41–45 (2007).

[41] J. R. Schaibley, H. Yu, G. Clark, P. Rivera, J. S. Ross, K. L. Seyler, W. Yao, and X. Xu, "Valleytronics in 2D materials", Nat. Rev. Mater. **1**, 1–15 (2016).

[42] S. A. Vitale, D. Nezich, J. O. Varghese, P. Kim, N. Gedik, P. Jarillo-Herrero, D. Xiao, and M. Rothschild, "Valleytronics: opportunities, challenges, and paths forward", Small **14**, 1801483 (2018).

[43] D. Xiao, G.-B. Liu, W. Feng, X. Xu, and W. Yao, "Coupled spin and valley physics in monolayers of MoS_2 and other group-VI dichalcogenides", Phys. Rev. Lett. **108**, 196802 (2012).

[44] K. F. Mak, K. He, J. Shan, and T. F. Heinz, "Control of valley polarization in monolayer MoS_2 by optical helicity", Nat. Nanotech. **7**, 494–498 (2012). DOI: 10.1038/nnano.2012.96.

[45] K. Wang, K. De Greve, L. A. Jauregui, A. Sushko, A. High, Y. Zhou, G. Scuri, T. Taniguchi, K. Watanabe, M. D. Lukin, et al., "Electrical control of charged carriers and excitons in atomically thin materials", Nat. Nanotechnol. **13**, 128–132 (2018).

[46] M. Brooks and G. Burkard, "Electric dipole spin resonance of two-dimensional semiconductor spin qubits", Phys. Rev. B **101**, 035204 (2020). DOI: 10.1103/PhysRevB.101.035204.

[47] G. Moody, C. K. Dass, K. Hao, C.-H. Chen, L.-J. Li, A. Singh, K. Tran, G. Clark, X. Xu, G. Berghäuser, et al., "Intrinsic homogeneous linewidth and broadening mechanisms of excitons in monolayer transition metal dichalcogenides", Nat. Commun. **6**, 1–6 (2015).

[48] M. Palummo, M. Bernardi, and J. C. Grossman, "Exciton radiative lifetimes in two-dimensional transition metal dichalcogenides", Nano Lett. **15**, 2794–2800 (2015).

[49] P. Rivera, K. L. Seyler, H. Yu, J. R. Schaibley, J. Yan, D. G. Mandrus, W. Yao, and X. Xu, "Valley-polarized exciton dynamics in a 2d semiconductor heterostructure", Science **351**, 688–691 (2016).

[50] P. Rivera, J. R. Schaibley, A. M. Jones, J. S. Ross, S. Wu, G. Aivazian, P. Klement, K. Seyler, G. Clark, N. J. Ghimire, et al., "Observation of long-lived interlayer excitons in monolayer mose 2–wse 2 heterostructures", Nat. Commun. **6**, 1–6 (2015).

[51] G.-B. Liu, H. Pang, Y. Yao, and W. Yao, "Intervalley coupling by quantum dot confinement potentials in monolayer transition metal dichalcogenides", New Journal of Physics **16**, 105011 (2014).

[52] A. Srivastava, M. Sidler, A. V. Allain, D. S. Lembke, A. Kis, and A. Imamoğlu, "Optically active quantum dots in monolayer wse 2", Nat. Nanotechnol. **10**, 491 (2015).

[53] M. Amani, D.-H. Lien, D. Kiriya, J. Xiao, A. Azcatl, J. Noh, S. R. Madhvapathy, R. Addou, K. Santosh, M. Dubey, et al., "Near-unity photoluminescence quantum yield in MoS_2", Science **350**, 1065–1068 (2015).

[54] D.-H. Lien, S. Z. Uddin, M. Yeh, M. Amani, H. Kim, J. W. Ager, E. Yablonovitch, and A. Javey, "Electrical suppression of all nonradiative recombination pathways in monolayer semiconductors", Science **364**, 468–471 (2019).

[55] M. Zürch, H.-T. Chang, P. M. Kraus, S. K. Cushing, L. J. Borja, A. Gandman, C. J. Kaplan, M. H. Oh, J. S. Prell, D. Prendergast, et al., "Ultrafast carrier thermalization and trapping in silicon-germanium alloy probed by extreme ultraviolet transient absorption spectroscopy", Structural Dynamics **4**, 044029 (2017).

[56] E. Najafi, V. Ivanov, A. Zewail, and M. Bernardi, "Super-diffusion of excited carriers in semiconductors", Nat. Commun. **8**, 15177 (2017).

[57] M. Buzzi, M. Först, R. Mankowsky, and A. Cavalleri, "Probing dynamics in quantum materials with femtosecond x-rays", Nature Reviews Materials **3**, 299–311 (2018).

[58] C. Pöllmann, P. Steinleitner, U. Leierseder, P. Nagler, G. Plechinger, M. Porer, R. Bratschitsch, C. Schüller, T. Korn, and R. Huber, "Resonant internal quantum transitions and femtosecond radiative decay of excitons in monolayer WSe_2", Nat. Mater **14**, 889–893 (2015).

[59] T. Korn, S. Heydrich, M. Hirmer, J. Schmutzler, and C. Schüller, "Low-temperature photocarrier dynamics in monolayer MoS_2", Appl. Phys. Lett. **99**, 102109 (2011). DOI: 10.1063/1.3636402.

[60] R. Bertoni, C. W. Nicholson, L. Waldecker, H. Hübener, C. Monney, U. De Giovannini, M. Puppin, M. Hoesch, E. Springate, R. T. Chapman, C. Cacho, M. Wolf, A. Rubio, and R. Ernstorfer, "Generation and evolution of spin-, valley-, and layer-polarized excited carriers in inversion-symmetric WSe_2", Phys. Rev. Lett. **117**, 277201 (2016). DOI: 10.1103/PhysRevLett.117.277201.

[61] S. Baroni, S. De Gironcoli, A. Dal Corso, and P. Giannozzi, "Phonons and related crystal properties from density-functional perturbation theory", Rev. Mod. Phys. **73**, 515 (2001).

[62] M. Bernardi, "First-principles dynamics of electrons and phonons", Eur. Phys. J. B **89**, 239 (2016).

[63] E. Gross and W. Kohn, "Time-dependent density-functional theory", in *Advances in quantum chemistry*, Vol. 21 (Elsevier, 1990), pp. 255–291.

[64] K. Yabana and G. F. Bertsch, "Time-dependent local-density approximation in real time", Phys. Rev. B **54**, 4484–4487 (1996). DOI: 10.1103/PhysRevB.54.4484.

[65] A. Castro, M. A. Marques, and A. Rubio, "Propagators for the time-dependent kohn–sham equations", The Journal of chemical physics **121**, 3425–3433 (2004).

[66] M. K. Nazeeruddin, F. De Angelis, S. Fantacci, A. Selloni, G. Viscardi, P. Liska, S. Ito, B. Takeru, and M. Grätzel, "Combined experimental and dft-tddft computational study of photoelectrochemical cell ruthenium sensitizers", Journal of the American Chemical Society **127**, 16835–16847 (2005).

[67] V. A. Jhalani, J.-J. Zhou, and M. Bernardi, "Ultrafast hot carrier dynamics in GaN and its impact on the efficiency droop", Nano Lett. **17**, 5012–5019 (2017).

[68] X. Tong and M. Bernardi, "Toward precise simulations of the coupled ultrafast dynamics of electrons and atomic vibrations in materials", arXiv preprint arXiv:2009.07958 (2020).

[69] W. Kohn and L. J. Sham, "Self-consistent equations including exchange and correlation effects", Phys. Rev. **140**, A1133–A1138 (1965). DOI: 10.1103/PhysRev.140.A1133.

[70] M. S. Hybertsen and S. G. Louie, "Electron correlation in semiconductors and insulators: band gaps and quasiparticle energies", Phys. Rev. B **34**, 5390–5413 (1986). DOI: 10.1103/PhysRevB.34.5390.

[71] G. Onida, L. Reining, and A. Rubio, "Electronic excitations: density-functional versus many-body Green's-function approaches", Reviews of modern physics **74**, 601 (2002).

[72] P. Hohenberg and W. Kohn, "Inhomogeneous electron gas", Phys. Rev. **136**, B864–B871 (1964). DOI: 10.1103/PhysRev.136.B864.

[73] D. M. Ceperley and B. J. Alder, "Ground state of the electron gas by a stochastic method", Phys. Rev. Lett. **45**, 566–569 (1980). DOI: 10.1103/PhysRevLett.45.566.

[74] J. P. Perdew, K. Burke, and M. Ernzerhof, "Generalized gradient approximation made simple", Phys. Rev. Lett. **77**, 3865–3868 (1996).

[75] M. Van Setten, M. Giantomassi, E. Bousquet, M. J. Verstraete, D. R. Hamann, X. Gonze, and G.-M. Rignanese, "The pseudodojo: training and grading a 85 element optimized norm-conserving pseudopotential table", Comput. Phys. Commun. **226**, 39–54 (2018).

[76] T. Kreibich and E. K. U. Gross, "Multicomponent density-functional theory for electrons and nuclei", Phys. Rev. Lett. **86**, 2984–2987 (2001). DOI: 10.1103/PhysRevLett.86.2984.

[77] U. von Barth and L. Hedin, "A local exchange-correlation potential for the spin polarized case. i", Journal of Physics C: Solid State Physics **5**, 1629 (1972).

[78] L. N. Oliveira, E. K. U. Gross, and W. Kohn, "Density-functional theory for superconductors", Phys. Rev. Lett. **60**, 2430–2433 (1988). DOI: 10.1103/PhysRevLett.60.2430.

[79] M. Lüders, M. A. L. Marques, N. N. Lathiotakis, A. Floris, G. Profeta, L. Fast, A. Continenza, S. Massidda, and E. K. U. Gross, "Ab initio theory of superconductivity. i. density functional formalism and approximate functionals", Phys. Rev. B **72**, 024545 (2005). DOI: 10.1103/PhysRevB.72.024545.

[80] P. Giannozzi, S. Baroni, N. Bonini, M. Calandra, R. Car, C. Cavazzoni, D. Ceresoli, G. L. Chiarotti, M. Cococcioni, I. Dabo, A. D. Corso, S. de Gironcoli, S. Fabris, G. Fratesi, R. Gebauer, U. Gerstmann, C. Gougoussis, A. Kokalj, M. Lazzeri, L. Martin-Samos, N. Marzari, F. Mauri, R. Mazzarello, S. Paolini, A. Pasquarello, L. Paulatto, C. Sbraccia, S. Scandolo, G. Sclauzero, A. P. Seitsonen, A. Smogunov, P. Umari, and R. M. Wentzcovitch, "Quantum espresso: a modular and open-source software project for quantum simulations of materials", Journal of physics: Condensed matter **21**, 395502 (2009).

[81] X. Gonze, B. Amadon, P.-M. Anglade, J.-M. Beuken, F. Bottin, P. Boulanger, F. Bruneval, D. Caliste, R. Caracas, M. Côté, et al., "Abinit: first-principles approach to material and nanosystem properties", Comput. Phys. Commun. **180**, 2582–2615 (2009).

[82] G. Kresse and J. Furthmüller, "Efficient iterative schemes for ab initio total-energy calculations using a plane-wave basis set", Phys. Rev. B **54**, 11169–11186 (1996). DOI: 10.1103/PhysRevB.54.11169.

[83] G. Strinati, "Effects of dynamical screening on resonances at inner-shell thresholds in semiconductors", Phys. Rev. B **29**, 5718 (1984).

[84] A. L. Fetter and J. D. Walecka, *Quantum Theory of Many-Particle Systems* (Courier Corporation, 2012).

[85] M. Rohlfing and S. G. Louie, "Electron-hole excitations and optical spectra from first principles", Phys. Rev. B **62**, 4927–4944 (2000). DOI: 10.1103/PhysRevB.62.4927.

[86] D. Sangalli, A. Ferretti, H. Miranda, C. Attaccalite, I. Marri, E. Cannuccia, P. Melo, M. Marsili, F. Paleari, A. Marrazzo, et al., "Many-body perturbation theory calculations using the yambo code", J. Phys. Condens. Matter **31**, 325902 (2019).

[87] X. Gonze, F. Jollet, F. A. Araujo, D. Adams, B. Amadon, T. Applencourt, C. Audouze, J.-M. Beuken, J. Bieder, A. Bokhanchuk, et al., "Recent developments in the abinit software package", Comput. Phys. Commun. **205**, 106–131 (2016).

[88] J. Deslippe, G. Samsonidze, D. A. Strubbe, M. Jain, M. L. Cohen, and S. G. Louie, "BerkeleyGW: A massively parallel computer package for the calculation of the quasiparticle and optical properties of materials and nanostructures", Comput. Phys. Commun. **183**, 1269–1289 (2012).

[89] R. M. Sternheimer, "Electronic polarizabilities of ions from the hartree-fock wave functions", Phys. Rev. **96**, 951–968 (1954). DOI: 10.1103/PhysRev.96.951.

[90] J.-J. Zhou, J. Park, I.-T. Lu, I. Maliyov, X. Tong, and M. Bernardi, "Perturbo: a software package for ab initio electron–phonon interactions, charge transport and ultrafast dynamics", Comput. Phys. Commun. **264**, 107970 (2021). DOI: https://doi.org/10.1016/j.cpc.2021.107970.

[91] B. K. Ridley, *Quantum processes in semiconductors* (Oxford University Press, 2013).

[92] P. T. Landsberg, *Recombination in semiconductors* (Cambridge University Press, Cambridge, 2003).

[93] J. Proot, C. Delerue, and G. Allan, "Electronic structure and optical properties of silicon crystallites: application to porous silicon", Appl. Phys. Lett. **61**, 1948–1950 (1992).

[94] X. Zhang, J.-X. Shen, W. Wang, and C. G. Van de Walle, "First-principles analysis of radiative recombination in lead-halide perovskites", ACS Energy Lett. **3**, 2329–2334 (2018).

[95] C. D. Spataru, S. Ismail-Beigi, R. B. Capaz, and S. G. Louie, "Theory and ab initio calculation of radiative lifetime of excitons in semiconducting carbon nanotubes", Phys. Rev. Lett. **95**, 247402 (2005).

[96] R. Loudon, *The quantum theory of light* (OUP Oxford, 2000).

[97] D. Sangalli, J. Berger, C. Attaccalite, M. Grüning, and P. Romaniello, "Optical properties of periodic systems within the current-current response framework: pitfalls and remedies", Phys. Rev. B **95**, 155203 (2017).

[98] J. P. Wolfe, "Thermodynamics of excitons in semiconductors", Phys. Today **35**, 46–54 (1982).

[99] M. Gatti and F. Sottile, "Exciton dispersion from first principles", Phys. Rev. B **88**, 155113 (2013).

[100] D. Y. Qiu, T. Cao, and S. G. Louie, "Nonanalyticity, valley quantum phases, and lightlike exciton dispersion in monolayer transition metal dichalcogenides: theory and first-principles calculations", Phys. Rev. Lett. **115**, 176801 (2015).

[101] P. Cudazzo, L. Sponza, C. Giorgetti, L. Reining, F. Sottile, and M. Gatti, "Exciton band structure in two-dimensional materials", Phys. Rev. Lett. **116**, 066803 (2016). DOI: 10.1103/PhysRevLett.116.066803.

[102] R. E. Newnham, *Properties of materials: anisotropy, symmetry, structure* (Oxford University Press, 2005), p. 67.

[103] R. J. Glauber and M. Lewenstein, "Quantum optics of dielectric media", Phys. Rev. A **43**, 467 (1991).

[104] G. Lasher and F. Stern, "Spontaneous and stimulated recombination radiation in semiconductors", Phys. Rev. **133**, A553–A563 (1964). DOI: 10.1103/PhysRev.133.A553.

[105] J. Im, A. Moritz, F. Steuber, V. Härle, F. Scholz, and A. Hangleiter, "Radiative carrier lifetime, momentum matrix element, and hole effective mass in GaN", Appl. Phys. Lett. **70**, 631–633 (1997).

[106] M. Bernardi, C. Ataca, M. Palummo, and J. C. Grossman, "Optical and electronic properties of two-dimensional layered materials", Nanophotonics **6**, 479–493 (2017).

[107] S. Gao, L. Yang, and C. D. Spataru, "Interlayer coupling and gate-tunable excitons in transition metal dichalcogenide heterostructures", Nano Lett. **17**, 7809–7813 (2017).

[108] P. Cudazzo, C. Attaccalite, I. V. Tokatly, and A. Rubio, "Strong charge-transfer excitonic effects and the Bose-Einstein exciton condensate in graphane", Phys. Rev. Lett. **104**, 226804 (2010).

[109] P. Avouris, M. Freitag, and V. Perebeinos, "Carbon-nanotube photonics and optoelectronics", Nat. Photon. **2**, 341 (2008).

[110] D. Dexter, "Theory of the optical properties of imperfections in nonmetals", in *Advances in research and applications*, Vol. 6, edited by F. Seitz and D. Turnbull, Solid State Physics (Academic Press, 1958), pp. 353–411, DOI: https://doi.org/10.1016/S0081-1947(08)60730-4.

[111] A. Einstein, "Zur quantentheorie der strahlung", Phys. Z. **18**, 124 (1917).

[112] C. D. Spataru, S. Ismail-Beigi, L. X. Benedict, and S. G. Louie, "Excitonic effects and optical spectra of single-walled carbon nanotubes", Phys. Rev. Lett. **92**, 077402 (2004).

[113] G. Breuer and E. K. Lee, "Fluorescence decay times and non-radiative decay rates of the first excited singlet states of methylated and fluorinated benzenes", Chem. Phys. Lett. **14**, 404–406 (1972).

[114] P. Jørgensen and J. Simons, *Geometrical derivatives of energy surfaces and molecular properties*, Vol. 166 (Springer Science & Business Media, 2012).

[115] S. Ismail-Beigi and S. G. Louie, "Excited-state forces within a first-principles Greens function formalism", Phys. Rev. Lett. **90**, 076401 (2003).

[116] J. Hutter, "Excited state nuclear forces from the Tamm-Dancoff approximation to time-dependent density functional theory within the plane wave basis set framework", J. Chem. Phys. **118**, 3928–3934 (2003).

[117] I. Berlman, *Handbook of florescence spectra of aromatic molecules* (Elsevier, 2012).

[118] K. Nakamura, "Fluorescence of fluorobenzene", J. Chem. Phys. **53**, 998–1004 (1970).

[119] K. Al-Ani and D. Phillips, "Quenching of excited states of fluorobenzene in the gas phase", J. Phys. Chem. **75**, 3662–3667 (1971).

[120] J. P. Perdew, A. Ruzsinszky, G. I. Csonka, O. A. Vydrov, G. E. Scuseria, L. A. Constantin, X. Zhou, and K. Burke, "Restoring the density-gradient expansion for exchange in solids and surfaces", Phys. Rev. Lett. **100**, 136406 (2008). DOI: 10.1103/PhysRevLett.100.136406.

[121] M. Levinshtein and S. Rumyantsev, "Galliumarsenide (GaAs)", in *Handbook Series On Semiconductor Parameters: Volume 1: Si, Ge, C (Diamond), GaAs, GaP, GaSb, InAs, InP, InSb* (World Scientific, 1996), pp. 77–103.

[122] A. Dargys and J. Kundrotas, *Handbook on Physical Properties of Ge, Si, GaAs and InP* (Science and Encyclopedia Publ., 1994).

[123] D. Kammerlander, S. Botti, M. A. L. Marques, A. Marini, and C. Attaccalite, "Speeding up the solution of the Bethe-Salpeter equation by a double-grid method and wannier interpolation", Phys. Rev. B **86**, 125203 (2012). DOI: 10.1103/PhysRevB.86.125203.

[124] G. W. 't Hooft, W. A. J. A. van der Poel, L. W. Molenkamp, and C. T. Foxon, "Giant oscillator strength of free excitons in GaAs", Phys. Rev. B **35**, 8281–8284 (1987).

[125] M. Gurioli, P. Borri, M. Colocci, M. Gulia, F. Rossi, E. Molinari, P. E. Selbmann, and P. Lugli, "Exciton formation and relaxation in gaas epilayers", Phys. Rev. B **58**, R13403–R13406 (1998). DOI: 10.1103/PhysRevB.58.R13403.

[126] M. Beck, J. Hübner, M. Oestreich, S. Bieker, T. Henn, T. Kiessling, W. Ossau, and L. W. Molenkamp, "Thermodynamic origin of the slow free exciton photoluminescence rise in GaAs", Phys. Rev. B **93**, 081204 (2016). DOI: 10.1103/PhysRevB.93.081204.

[127] Y. Liang, S. Huang, R. Soklaski, and L. Yang, "Quasiparticle band-edge energy and band offsets of monolayer of molybdenum and tungsten chalcogenides", Appl. Phys. Lett. **103**, 042106 (2013).

[128] C. Zhang, Y. Chen, A. Johnson, M.-Y. Li, L.-J. Li, P. C. Mende, R. M. Feenstra, and C.-K. Shih, "Probing critical point energies of transition metal dichalcogenides: surprising indirect gap of single layer WSe_2", Nano Lett. **15**, 6494–6500 (2015).

[129] M. Bernardi, M. Palummo, and J. C. Grossman, "Extraordinary sunlight absorption and one nanometer thick photovoltaics using two-dimensional monolayer materials", Nano Lett. **13**, 3664–3670 (2013). DOI: 10.1021/nl401544y.

[130] L. Sortino, P. G. Zotev, S. Mignuzzi, J. Cambiasso, D. Schmidt, A. Genco, M. Aßmann, M. Bayer, S. A. Maier, R. Sapienza, and A. I. Tartakovskii, "Enhanced light-matter interaction in an atomically thin semiconductor coupled with dielectric nano-antennas", Nat. Commun. **10**, 1–8 (2019).

[131] Q. H. Wang, K. Kalantar-Zadeh, A. Kis, J. N. Coleman, and M. S. Strano, "Electronics and optoelectronics of two-dimensional transition metal dichalcogenides", Nat. Nanotechnol. **7**, 699 (2012).

[132] G. Eda and S. A. Maier, "Two-dimensional crystals: managing light for optoelectronics", ACS Nano **7**, 5660–5665 (2013).

[133] J. Wong, D. Jariwala, G. Tagliabue, K. Tat, A. R. Davoyan, M. C. Sherrott, and H. A. Atwater, "High photovoltaic quantum efficiency in ultrathin van der waals heterostructures", ACS Nano **11**, 7230–7240 (2017). DOI: 10.1021/acsnano.7b03148.

[134] L. Britnell, R. Ribeiro, A. Eckmann, R. Jalil, B. Belle, A. Mishchenko, Y.-J. Kim, R. Gorbachev, T. Georgiou, S. Morozov, et al., "Strong light-matter interactions in heterostructures of atomically thin films", Science **340**, 1311–1314 (2013).

[135] H. Shi, R. Yan, S. Bertolazzi, J. Brivio, B. Gao, A. Kis, D. Jena, H. G. Xing, and L. Huang, "Exciton dynamics in suspended monolayer and few-layer MoS_2 2D crystals", ACS Nano **7**, 1072–1080 (2013). DOI: 10.1021/nn303973r.

[136] D. Lagarde, L. Bouet, X. Marie, C. R. Zhu, B. L. Liu, T. Amand, P. H. Tan, and B. Urbaszek, "Carrier and polarization dynamics in monolayer MoS_2", Phys. Rev. Lett. **112**, 047401 (2014). DOI: 10.1103/PhysRevLett.112.047401.

[137] L. Yuan, T. Wang, T. Zhu, M. Zhou, and L. Huang, "Exciton dynamics, transport, and annihilation in atomically thin two-dimensional semiconductors", J. Phys. Chem. Lett. **8**, 3371–3379 (2017).

[138] W. Yao, D. Xiao, and Q. Niu, "Valley-dependent optoelectronics from inversion symmetry breaking", Phys. Rev. B **77**, 235406 (2008). DOI: 10.1103/PhysRevB.77.235406.

[139] T. Cao, G. Wang, W. Han, H. Ye, C. Zhu, J. Shi, Q. Niu, P. Tan, E. Wang, B. Liu, and J. Feng, "Valley-selective circular dichroism of monolayer molybdenum disulphide", Nat Commun. **3**, 887 (2012).

[140] X. Xu, W. Yao, D. Xiao, and T. F. Heinz, "Spin and pseudospins in layered transition metal dichalcogenides", Nat. Phys. **10**, 343–350 (2014). DOI: 10.1038/nphys2942.

[141] H. Zeng, J. Dai, W. Yao, D. Xiao, and X. Cui, "Valley polarization in MoS_2 monolayers by optical pumping", Nat. Nanotechnol. **7**, 490–493 (2012). DOI: 10.1038/nnano.2012.95.

[142] A. M. Jones, H. Yu, N. J. Ghimire, S. Wu, G. Aivazian, J. S. Ross, B. Zhao, J. Yan, D. G. Mandrus, D. Xiao, W. Yao, and X. Xu, "Optical generation of excitonic valley coherence in monolayer WSe_2", Nat. Nanotechnol. **8**, 634–638 (2013).

[143] G. Wang, X. Marie, B. Liu, T. Amand, C. Robert, F. Cadiz, P. Renucci, and B. Urbaszek, "Control of exciton valley coherence in transition metal dichalcogenide monolayers", Phys. Rev. Lett. **117**, 187401 (2016).

[144] Z. Ye, D. Sun, and T. F. Heinz, "Optical manipulation of valley pseudospin", Nature physics **13**, 26 (2017).

[145] T. Yu and M. Wu, "Valley depolarization due to intervalley and intravalley electron-hole exchange interactions in monolayer MoS_2", Phys. Rev. B **89**, 205303 (2014).

[146] T. Yu and M. W. Wu, "Valley depolarization dynamics and valley hall effect of excitons in monolayer and bilayer MoS_2", Phys. Rev. B **93**, 045414 (2016). DOI: 10.1103/PhysRevB.93.045414.

[147] A. Molina-Sánchez, D. Sangalli, L. Wirtz, and A. Marini, "Ab initio calculations of ultrashort carrier dynamics in two-dimensional materials: valley depolarization in single-layer WSe_2", Nano Lett. **17**, 4549–4555 (2017).

[148] C. Mai, A. Barrette, Y. Yu, Y. G. Semenov, K. W. Kim, L. Cao, and K. Gundogdu, "Many-body effects in valleytronics: direct measurement of valley lifetimes in single-layer MoS_2", Nano Lett. **14**, 202–206 (2014).

[149] K. Hao, G. Moody, F. Wu, C. K. Dass, L. Xu, C.-H. Chen, L. Sun, M.-Y. Li, L.-J. Li, A. H. MacDonald, and X. Li, "Direct measurement of exciton valley coherence in monolayer WSe_2", Nat. Phys. **12**, 677–682 (2016).

[150] T. Cheiwchanchamnangij and W. R. L. Lambrecht, "Quasiparticle band structure calculation of monolayer, bilayer, and bulk MoS_2", Phys. Rev. B **85**, 205302 (2012). DOI: 10.1103/PhysRevB.85.205302.

[151] B. Hall, *Lie groups, lie algebras, and representations: an elementary introduction* (Springer, 2015).

[152] R. C. Jones, "A new calculus for the treatment of optical systemsi. description and discussion of the calculus", J. Opt. Soc. Am. **31**, 488–493 (1941). DOI: 10.1364/JOSA.31.000488.

[153] A. J. Goodman, A. P. Willard, and W. A. Tisdale, "Exciton trapping is responsible for the long apparent lifetime in acid-treated MoS_2", Phys. Rev. B **96**, 121404 (2017). DOI: 10.1103/PhysRevB.96.121404.

[154] T. T. Tran, K. Bray, M. J. Ford, M. Toth, and I. Aharonovich, "Quantum emission from hexagonal boron nitride monolayers", Nat. Nanotechnol. **11**, 37–41 (2016).

[155] L. Childress, M. G. Dutt, J. Taylor, A. Zibrov, F. Jelezko, J. Wrachtrup, P. Hemmer, and M. Lukin, "Coherent dynamics of coupled electron and nuclear spin qubits in diamond", Science **314**, 281–285 (2006).

[156] T. D. Ladd, F. Jelezko, R. Laflamme, Y. Nakamura, C. Monroe, and J. L. O'Brien, "Quantum computers", Nature **464**, 45–53 (2010).

[157] B. Hensen, H. Bernien, A. E. Dréau, A. Reiserer, N. Kalb, M. S. Blok, J. Ruitenberg, R. F. Vermeulen, R. N. Schouten, C. Abellán, et al., "Loophole-free bell inequality violation using electron spins separated by 1.3 kilometres", Nature **526**, 682–686 (2015).

[158] I. Aharonovich, D. Englund, and M. Toth, "Solid-state single-photon emitters", Nature Photonics **10**, 631–641 (2016).

[159] X. Liu and M. C. Hersam, "2D materials for quantum information science", Nature Reviews Materials **4**, 669–684 (2019).

[160] J. D. Caldwell, I. Aharonovich, G. Cassabois, J. H. Edgar, B. Gil, and D. Basov, "Photonics with hexagonal boron nitride", Nature Reviews Materials **4**, 552–567 (2019).

[161] N. R. Jungwirth, B. Calderon, Y. Ji, M. G. Spencer, M. E. Flatté, and G. D. Fuchs, "Temperature dependence of wavelength selectable zero-phonon emission from single defects in hexagonal boron nitride", Nano Lett. **16**, 6052–6057 (2016).

[162] T. T. Tran, C. Elbadawi, D. Totonjian, C. J. Lobo, G. Grosso, H. Moon, D. R. Englund, M. J. Ford, I. Aharonovich, and M. Toth, "Robust multicolor single photon emission from point defects in hexagonal boron nitride", ACS Nano **10**, 7331–7338 (2016).

[163] A. Dietrich, M. Bürk, E. S. Steiger, L. Antoniuk, T. T. Tran, M. Nguyen, I. Aharonovich, F. Jelezko, and A. Kubanek, "Observation of fourier transform limited lines in hexagonal boron nitride", Phys. Rev. B **98**, 081414 (2018). DOI: 10.1103/PhysRevB.98.081414.

[164] S. A. Tawfik, S. Ali, M. Fronzi, M. Kianinia, T. T. Tran, C. Stampfl, I. Aharonovich, M. Toth, and M. J. Ford, "First-principles investigation of quantum emission from hBN defects", Nanoscale **9**, 13575–13582 (2017).

[165] L. Weston, D. Wickramaratne, M. Mackoit, A. Alkauskas, and C. G. Van de Walle, "Native point defects and impurities in hexagonal boron nitride", Phys. Rev. B **97**, 214104 (2018). DOI: 10.1103/PhysRevB.97.214104.

[166] A. Sajid, J. R. Reimers, and M. J. Ford, "Defect states in hexagonal boron nitride: assignments of observed properties and prediction of properties relevant to quantum computation", Phys. Rev. B **97**, 064101 (2018). DOI: 10.1103/PhysRevB.97.064101.

[167] G. I. López-Morales, N. V. Proscia, G. E. López, C. A. Meriles, and V. M. Menon, "Toward the identification of atomic defects in hexagonal boron nitride: x-ray photoelectron spectroscopy and first-principles calculations", arXiv preprint arXiv:1811.05924 (2018).

[168] G. Noh, D. Choi, J.-H. Kim, D.-G. Im, Y.-H. Kim, H. Seo, and J. Lee, "Stark tuning of single-photon emitters in hexagonal boron nitride", Nano Lett. **18**, 4710–4715 (2018).

[169] M. Abdi, J.-P. Chou, A. Gali, and M. B. Plenio, "Color centers in hexagonal boron nitride monolayers: a group theory and ab initio analysis", ACS Photonics **5**, 1967–1976 (2018).

[170] M. E. Turiansky, A. Alkauskas, L. C. Bassett, and C. G. Van de Walle, "Dangling bonds in hexagonal boron nitride as single-photon emitters", Phys. Rev. Lett. **123**, 127401 (2019). DOI: 10.1103/PhysRevLett.123.127401.

[171] D. Y. Qiu, F. H. da Jornada, and S. G. Louie, "Optical spectrum of MoS_2: many-body effects and diversity of exciton states", Phys. Rev. Lett. **111**, 216805 (2013). DOI: 10.1103/PhysRevLett.111.216805.

[172] S. Refaely-Abramson, D. Y. Qiu, S. G. Louie, and J. B. Neaton, "Defect-induced modification of low-lying excitons and valley selectivity in monolayer transition metal dichalcogenides", Phys. Rev. Lett. **121**, 167402 (2018). DOI: 10.1103/PhysRevLett.121.167402.

[173] C. Attaccalite, M. Bockstedte, A. Marini, A. Rubio, and L. Wirtz, "Coupling of excitons and defect states in boron-nitride nanostructures", Phys. Rev. B **83**, 144115 (2011). DOI: 10.1103/PhysRevB.83.144115.

[174] H. J. Kimble, M. Dagenais, and L. Mandel, "Photon antibunching in resonance fluorescence", Phys. Rev. Lett. **39**, 691–695 (1977). DOI: 10.1103/PhysRevLett.39.691.

[175] A. L. Exarhos, D. A. Hopper, R. R. Grote, A. Alkauskas, and L. C. Bassett, "Optical signatures of quantum emitters in suspended hexagonal boron nitride", ACS Nano **11**, 3328–3336 (2017).

[176] F. Hayee, L. Yu, J. L. Zhang, C. J. Ciccarino, M. Nguyen, A. F. Marshall, I. Aharonovich, J. Vuckovic, P. Narang, T. F. Heinz, et al., "Revealing multiple classes of stable quantum emitters in hexagonal boron nitride with correlated optical and electron microscopy", Nat. Mater **19**, 534–539 (2020).

[177] N. Chejanovsky, M. Rezai, F. Paolucci, Y. Kim, T. Rendler, W. Rouabeh, F. Fávaro de Oliveira, P. Herlinger, A. Denisenko, S. Yang, et al., "Structural attributes and photodynamics of visible spectrum quantum emitters in hexagonal boron nitride", Nano Lett. **16**, 7037–7045 (2016).

[178] S. Choi, T. T. Tran, C. Elbadawi, C. Lobo, X. Wang, S. Juodkazis, G. Seniutinas, M. Toth, and I. Aharonovich, "Engineering and localization of quantum emitters in large hexagonal boron nitride layers", ACS applied materials & interfaces **8**, 29642–29648 (2016).

[179] P. Cudazzo, I. V. Tokatly, and A. Rubio, "Dielectric screening in two-dimensional insulators: implications for excitonic and impurity states in graphane", Phys. Rev. B **84**, 085406 (2011). DOI: 10.1103/PhysRevB.84.085406.

[180] K. Andersen, S. Latini, and K. S. Thygesen, "Dielectric genome of van der waals heterostructures", Nano Lett. **15**, 4616–4621 (2015).

[181] R. Bourrellier, S. Meuret, A. Tararan, O. Stéphan, M. Kociak, L. H. Tizei, and A. Zobelli, "Bright uv single photon emission at point defects in h-BN", Nano Lett. **16**, 4317–4321 (2016).

[182] Q.-H. Tan, K.-X. Xu, X.-L. Liu, D. Guo, Y.-Z. Xue, S.-L. Ren, Y.-F. Gao, X.-M. Dou, B.-Q. Sun, H.-X. Deng, et al., "Ultraviolet to near-infrared single photon emitters in hBN", arXiv preprint arXiv:1908.06578 (2019).

[183] U. von Toussaint, "Bayesian inference in physics", Rev. Mod. Phys. **83**, 943–999 (2011). DOI: 10.1103/RevModPhys.83.943.

[184] S. Gao, H.-Y. Chen, and M. Bernardi, "Radiative properties and excitons of candidate defect emitters in hexagonal boron nitride", NPJ Comput. Mater. 2020 (Accepted for publication) (2020),

[185] S. Pimputkar, J. S. Speck, S. P. DenBaars, and S. Nakamura, "Prospects for led lighting", Nat. Photonics **3**, 180–182 (2009).

[186] J. Muth, J. Lee, I. Shmagin, R. Kolbas, H. Casey Jr, B. Keller, U. Mishra, and S. DenBaars, "Absorption coefficient, energy gap, exciton binding energy, and recombination lifetime of GaN obtained from transmission measurements", Appl. Phys. Lett. **71**, 2572–2574 (1997).

[187] R. Laskowski, N. E. Christensen, G. Santi, and C. Ambrosch-Draxl, "Ab initio calculations of excitons in GaN", Phys. Rev. B **72**, 035204 (2005). DOI: 10.1103/PhysRevB.72.035204.

[188] C. Harris, B. Monemar, H. Amano, and I. Akasaki, "Exciton lifetimes in GaN and GaInN", Appl. Phys. Lett. **67**, 840–842 (1995).

[189] G. Chen, M. Smith, J. Lin, H. Jiang, S.-H. Wei, M. Asif Khan, and C. Sun, "Fundamental optical transitions in GaN", Appl. Phys. Lett. **68**, 2784–2786 (1996).

[190] O. Brandt, J. Ringling, K. H. Ploog, H.-J. Wünsche, and F. Henneberger, "Temperature dependence of the radiative lifetime in GaN", Phys. Rev. B **58**, R15977–R15980 (1998). DOI: 10.1103/PhysRevB.58.R15977.

[191] E. Kioupakis, Q. Yan, D. Steiauf, and C. G. Van de Walle, "Temperature and carrier-density dependence of auger and radiative recombination in nitride optoelectronic devices", New Journal of Physics **15**, 125006 (2013).

[192] D. R. Hamann, "Optimized norm-conserving vanderbilt pseudopotentials", Phys. Rev. B **88**, 085117 (2013). DOI: 10.1103/PhysRevB.88.085117.

[193] S. G. Louie, S. Froyen, and M. L. Cohen, "Nonlinear ionic pseudopotentials in spin-density-functional calculations", Phys. Rev. B **26**, 1738–1742 (1982). DOI: 10.1103/PhysRevB.26.1738.

[194] A. Rubio, J. L. Corkill, M. L. Cohen, E. L. Shirley, and S. G. Louie, "Quasiparticle band structure of AlN and GaN", Phys. Rev. B **48**, 11810–11816 (1993). DOI: 10.1103/PhysRevB.48.11810.

[195] F. Fuchs, C. Rödl, A. Schleife, and F. Bechstedt, "Efficient O(N^2) approach to solve the Bethe-Salpeter equation for excitonic bound states", Phys. Rev. B **78**, 085103 (2008). DOI: 10.1103/PhysRevB.78.085103.

[196] H. W. Yoon, D. R. Wake, and J. P. Wolfe, "Effect of exciton-carrier thermodynamics on the gaas quantum well photoluminescence", Phys. Rev. B **54**, 2763–2774 (1996). DOI: 10.1103/PhysRevB.54.2763.

[197] D. Jacquemin, I. Duchemin, and X. Blase, "Is the Bethe–Salpeter Formalism Accurate for Excitation Energies? Comparisons with TD-DFT, CASPT2, and EOM-CCSD", J. Phys. Chem. Lett. **8**, 1524–1529 (2017).

[198] X. Marie and B. Urbaszek, "2D materials: ultrafast exciton dynamics", Nat. Mater. **14**, 860 (2015).

[199] P. Steinleitner, P. Merkl, P. Nagler, J. Mornhinweg, C. Schuller, T. Korn, A. Chernikov, and R. Huber, "Direct observation of ultrafast exciton formation in a monolayer of WSe_2", Nano Lett. **17**, 1455–1460 (2017).

[200] T. A. Oliver, "Recent advances in multidimensional ultrafast spectroscopy", R. Soc. Open Sci. **5**, 171425 (2018).

[201] J.-J. Zhou and M. Bernardi, "Ab initio electron mobility and polar phonon scattering in GaAs", Phys. Rev. B **94**, 201201 (2016).

[202] N.-E. Lee, J.-J. Zhou, L. A. Agapito, and M. Bernardi, "Charge transport in organic molecular semiconductors from first principles: the bandlike hole mobility in a naphthalene crystal", Phys. Rev. B **97**, 115203 (2018). DOI: 10.1103/PhysRevB.97.115203.

[203] J.-J. Zhou, O. Hellman, and M. Bernardi, "Electron-phonon scattering in the presence of soft modes and electron mobility in srtio 3 perovskite from first principles", Phys. Rev. Lett. **121**, 226603 (2018).

[204] M. Bernardi, D. Vigil-Fowler, J. Lischner, J. B. Neaton, and S. G. Louie, "Ab initio study of hot carriers in the first picosecond after sunlight absorption in silicon", Phys. Rev. Lett. **112**, 257402 (2014).

[205] L. A. Agapito and M. Bernardi, "Ab initio electron-phonon interactions using atomic orbital wave functions", Phys. Rev. B **97**, 235146 (2018).

[206] Y. Wang, B. R. Carvalho, and V. H. Crespi, "Strong exciton regulation of raman scattering in monolayer MoS_2", Phys. Rev. B **98**, 161405 (2018).

[207] M. Wang, Y. Gong, F. Alzina, O. Svoboda, B. Ballesteros, C. M. S. Torres, S. Xiao, Z. Zhang, and J. He, "Raman antenna effect from exciton–phonon coupling in organic semiconducting nanobelts", Nanoscale **9**, 19328–19336 (2017).

[208] E. Cannuccia, B. Monserrat, and C. Attaccalite, "Theory of phonon-assisted luminescence in solids: application to hexagonal boron nitride", Phys. Rev. B **99**, 081109 (2019). DOI: 10.1103/PhysRevB.99.081109.

[209] G. Macfarlane, T. McLean, J. Quarrington, and V. Roberts, "Fine structure in the absorption-edge spectrum of ge", Phys. Rev. **108**, 1377 (1957).

[210] G. Macfarlane, T. McLean, J. Quarrington, and V. Roberts, "Fine structure in the absorption-edge spectrum of si", Phys. Rev. **111**, 1245 (1958).

[211] S. Helmrich, R. Schneider, A. W. Achtstein, A. Arora, B. Herzog, S. M. de Vasconcellos, M. Kolarczik, O. Schöps, R. Bratschitsch, U. Woggon, et al., "Exciton–phonon coupling in mono-and bilayer MoTe2", 2D Mater. **5**, 045007 (2018).

[212] U. Bockelmann, "Exciton relaxation and radiative recombination in semiconductor quantum dots", Phys. Rev. B **48**, 17637–17640 (1993). DOI: 10.1103/PhysRevB.48.17637.

[213] F. Paleari, H. P. C. Miranda, A. Molina-Sánchez, and L. Wirtz, "Exciton-phonon coupling in the ultraviolet absorption and emission spectra of bulk hexagonal boron nitride", Phys. Rev. Lett. **122**, 187401 (2019). DOI: 10.1103/PhysRevLett.122.187401.

[214] Y. Toyozawa, "Theory of Line-Shapes of the Exciton Absorption Bands", Progress of Theoretical Physics **20**, 53–81 (1958). DOI: 10.1143/PTP.20.53.

[215] B. Segall and G. D. Mahan, "Phonon-assisted recombination of free excitons in compound semiconductors", Phys. Rev. **171**, 935–948 (1968). DOI: 10.1103/PhysRev.171.935.

[216] V. Perebeinos, J. Tersoff, and P. Avouris, "Effect of exciton-phonon coupling in the calculated optical absorption of carbon nanotubes", Phys. Rev. Lett. **94**, 027402 (2005). DOI: 10.1103/PhysRevLett.94.027402.

[217] J. Jiang, R. Saito, K. Sato, J. Park, G. G. Samsonidze, A. Jorio, G. Dresselhaus, and M. Dresselhaus, "Exciton-photon, exciton-phonon matrix elements, and resonant raman intensity of single-wall carbon nanotubes", Phys. Rev. B **75**, 035405 (2007).

[218] S. Shree, M. Semina, C. Robert, B. Han, T. Amand, A. Balocchi, M. Manca, E. Courtade, X. Marie, T. Taniguchi, et al., "Observation of exciton-phonon coupling in $MoSe_2$ monolayers", Phys. Rev. B **98**, 035302 (2018).

[219] S. Brem, M. Selig, G. Berghaeuser, and E. Malic, "Exciton relaxation cascade in two-dimensional transition metal dichalcogenides", Sci. Rep. **8**, 8238 (2018).

[220] D. Christiansen, M. Selig, E. Malic, R. Ernstorfer, and A. Knorr, "Theory of exciton dynamics in time-resolved ARPES: Intra-and intervalley scattering in two-dimensional semiconductors", Phys. Rev. B **100**, 205401 (2019).

[221] G. Antonius and S. G. Louie, "Theory of the exciton-phonon coupling", arXiv:1705.04245.

[222] G. Strinati, "Dynamical shift and broadening of core excitons in semiconductors", Phys. Rev. Lett. **49**, 1519 (1982).

[223] L. Wirtz, A. Marini, and A. Rubio, "Optical absorption of hexagonal boron nitride and BN nanotubes", **786**, 391–395 (2005).

[224] G. Cassabois, P. Valvin, and B. Gil, "Hexagonal boron nitride is an indirect bandgap semiconductor", Nat. Photonics **10**, 262–266 (2016).

[225] G. D. Mahan, *Many-particle physics* (Springer Science & Business Media, 2013).

[226] L. Sponza, H. Amara, F. Ducastelle, A. Loiseau, and C. Attaccalite, "Exciton interference in hexagonal boron nitride", Phys. Rev. B **97**, 075121 (2018).

[227] L. Sponza, H. Amara, C. Attaccalite, S. Latil, T. Galvani, F. Paleari, L. Wirtz, and F. Ducastelle, "Direct and indirect excitons in boron nitride polymorphs: a story of atomic configuration and electronic correlation", Phys. Rev. B **98**, 125206 (2018). DOI: 10.1103/PhysRevB.98.125206.

[228] T. Vuong, G. Cassabois, P. Valvin, S. Liu, J. Edgar, and B. Gil, "Exciton-phonon interaction in the strong-coupling regime in hexagonal boron nitride", Phys. Rev. B **95**, 201202 (2017).

[229] W. Choi, N. Choudhary, G. H. Han, J. Park, D. Akinwande, and Y. H. Lee, "Recent development of two-dimensional transition metal dichalcogenides and their applications", Materials Today **20**, 116–130 (2017).

[230] W.-S. Tseng, Y.-C. Chen, C.-C. Hsu, C.-H. Lu, C.-I. Wu, and N.-C. Yeh, "Direct large-area growth of graphene on silicon for potential ultra-low-friction applications and silicon-based technologies", Nanotechnology **31**, 335602 (2020).

[231] Y. Li, A. Chernikov, X. Zhang, A. Rigosi, H. M. Hill, A. M. van der Zande, D. A. Chenet, E.-M. Shih, J. Hone, and T. F. Heinz, "Measurement of the optical dielectric function of monolayer transition-metal dichalcogenides: MoS_2, $MoSe_2$, WS_2, and WSe_2", Phys. Rev. B **90**, 205422 (2014). DOI: 10.1103/PhysRevB.90.205422.

[232] M. Selig, G. Berghäuser, A. Raja, P. Nagler, C. Schüller, T. F. Heinz, T. Korn, A. Chernikov, E. Malic, and A. Knorr, "Excitonic linewidth and coherence lifetime in monolayer transition metal dichalcogenides", Nat. Commun. **7**, 1–6 (2016).

[233] M. He, P. Rivera, D. Van Tuan, N. P. Wilson, M. Yang, T. Taniguchi, K. Watanabe, J. Yan, D. G. Mandrus, H. Yu, H. Dery, W. Yao, and X. Xu, "Valley phonons and exciton complexes in a monolayer semiconductor", Nat. Commun. **11**, 1–7 (2020).

[234] M. Kira and S. W. Koch, "Many-body correlations and excitonic effects in semiconductor spectroscopy", Progress in quantum electronics **30**, 155–296 (2006).

[235] A. Ramasubramaniam, "Large excitonic effects in monolayers of molybdenum and tungsten dichalcogenides", Phys. Rev. B **86**, 115409 (2012).

[236] J. Gusakova, X. Wang, L. L. Shiau, A. Krivosheeva, V. Shaposhnikov, V. Borisenko, V. Gusakov, and B. K. Tay, "Electronic properties of bulk and monolayer TMDs: theoretical study within DFT framework (GVJ-2e method)", physica status solidi (a) **214**, 1700218 (2017).

[237] W.-T. Hsu, L.-S. Lu, D. Wang, J.-K. Huang, M.-Y. Li, T.-R. Chang, Y.-C. Chou, Z.-Y. Juang, H.-T. Jeng, L.-J. Li, and W.-H. Chang, "Evidence of indirect gap in monolayer WSe_2", Nat. Commun. **8**, 1–7 (2017).

[238] V. Chellappan, A. L. C. Pang, S. Sarkar, Z. E. Ooi, and K. E. J. Goh, "Effect of phonons on valley depolarization in monolayer WSe_2", Electronic Materials Letters **14**, 766–773 (2018).

[239] H. Liu, J. Chen, H. Yu, F. Yang, L. Jiao, G.-B. Liu, W. Ho, C. Gao, J. Jia, W. Yao, and M. Xie, "Observation of intervalley quantum interference in epitaxial monolayer tungsten diselenide", Nat. Commun. **6**, 1–6 (2015).

[240] L. Zhang and Q. Niu, "Chiral phonons at high-symmetry points in monolayer hexagonal lattices", Phys. Rev. Lett. **115**, 115502 (2015).

[241] E. Courtade, M. Semina, M. Manca, M. M. Glazov, C. Robert, F. Cadiz, G. Wang, T. Taniguchi, K. Watanabe, M. Pierre, W. Escoffier, E. L. Ivchenko, P. Renucci, X. Marie, T. Amand, and B. Urbaszek, "Charged excitons in monolayer WSe_2: experiment and theory", Phys. Rev. B **96**, 085302 (2017).

[242] Z. Wang, A. Molina-Sánchez, P. Altmann, D. Sangalli, D. De Fazio, G. Soavi, U. Sassi, F. Bottegoni, F. Ciccacci, M. Finazzi, L. Wirtz, A. C. Ferrari, A. Marini, G. Cerullo, and S. Dal Conte, "Intravalley spin–flip relaxation dynamics in single-layer WS_2", Nano Lett. **18**, 6882–6891 (2018).

[243] A. Damascelli, "Probing the electronic structure of complex systems by arpes", Physica Scripta **2004**, 61 (2004).

[244] L. Waldecker, R. Bertoni, H. Hübener, T. Brumme, T. Vasileiadis, D. Zahn, A. Rubio, and R. Ernstorfer, "Momentum-resolved view of electron-phonon coupling in multilayer WSe_2", Phys. Rev. Lett. **119**, 036803 (2017).

[245] M. Puppin, Y. Deng, C. Nicholson, J. Feldl, N. Schröter, H. Vita, P. Kirchmann, C. Monney, L. Rettig, M. Wolf, et al., "Time-and angle-resolved photoemission spectroscopy of solids in the extreme ultraviolet at 500 khz repetition rate", Review of Scientific Instruments **90**, 023104 (2019).

[246] E. Perfetto, D. Sangalli, A. Marini, and G. Stefanucci, "First-principles approach to excitons in time-resolved and angle-resolved photoemission spectra", Phys. Rev. B **94**, 245303 (2016). DOI: 10.1103/PhysRevB.94.245303.

[247] M. Schlipf and F. Gygi, "Optimization algorithm for the generation of ONCV pseudopotentials", Comput. Phys. Commun. **196**, 36–44 (2015).

[248] J. P. Perdew and A. Zunger, "Self-interaction correction to density-functional approximations for many-electron systems", Phys. Rev. B **23**, 5048 (1981).

[249] N. Troullier and J. L. Martins, "Efficient pseudopotentials for plane-wave calculations", Phys. Rev. B **43**, 1993 (1991).

[250] R. Del Sole and E. Fiorino, "Macroscopic dielectric tensor at crystal surfaces", Phys. Rev. B **29**, 4631 (1984).

[251] V. M. Agranovich and V. Ginzburg, *Crystal optics with spatial dispersion, and excitons*, Vol. 42 (Springer Science & Business Media, 2013).

[252] C. Zhang, H. Wang, W. Chan, C. Manolatou, and F. Rana, "Absorption of light by excitons and trions in monolayers of metal dichalcogenide MoS_2: experiments and theory", Phys. Rev. B **89**, 205436 (2014). DOI: 10.1103/PhysRevB.89.205436.

[253] W.-T. Hsu, J. Quan, C.-Y. Wang, L.-S. Lu, M. Campbell, W.-H. Chang, L.-J. Li, X. Li, and C.-K. Shih, "Dielectric impact on exciton binding energy and quasiparticle bandgap in monolayer WS_2 and WSe_2", 2D Materials **6**, 025028 (2019).